University of Illinois at Urbana-Champaign

ACRC

Air Conditioning and Refrigeration Center A National Science Foundation/University Cooperative Research Center

Investigation of the Scuffing Mechanism under Starved Lubrication Conditions Using Macro, Meso, Micro and Nano Analytical Techniques

J. J. Patel, A. A. Polycarpou, and T. F. Conry

ACRC TR-191 December 2001

For additional information:

Air Conditioning and Refrigeration Center
University of Illinois
Mechanical & Industrial Engineering Dept.
1206 West Green Street
Urbana, IL 61801

(217) 333-3115

Prepared as part of ACRC Project #127
Fundamental Investigation on the Tribological
Failure Mechanisms of Compressor Surfaces -Scuffing
A. A. Polycarpou and T. F. Conry, Principal Investigators

The Air Conditioning and Refrigeration Center was founded in 1988 with a grant from the estate of Richard W. Kritzer, the founder of Peerless of America Inc. A State of Illinois Technology Challenge Grant helped build the laboratory facilities. The ACRC receives continuing support from the Richard W. Kritzer Endowment and the National Science Foundation. The following organizations have also become sponsors of the Center.

Alcan Aluminum Corporation
Amana Refrigeration, Inc.
Arçelik A. S.
Brazeway, Inc.
Carrier Corporation
Copeland Corporation
Dacor
Daikin Industries, Ltd.
Delphi Harrison Thermal Systems
General Motors Corporation
Hill PHOENIX
Honeywell, Inc.
Hydro Aluminum Adrian, Inc.
Ingersoll-Rand Company
Invensys Climate Controls
Kelon Electrical Holdings Co., Ltd.
Lennox International, Inc.
LG Electronics, Inc.
Modine Manufacturing Co.
Parker Hannifin Corporation
Peerless of America, Inc.
Samsung Electronics Co., Ltd.
Tecumseh Products Company
The Trane Company
Valeo, Inc.
Visteon Automotive Systems
Wolverine Tube, Inc.
York International, Inc.

For additional information:

Air Conditioning & Refrigeration Center
Mechanical & Industrial Engineering Dept.
University of Illinois
1206 West Green Street
Urbana, IL 61801

217 333 3115

Abstract

Studies to better understand scuffing began approximately sixty years ago, when it was postulated that scuffing occurs when a critical temperature of the surface is reached, at which desorption of surface films occurs. An extension to this hypothesis was proposed suggesting interaction of chemically active species with the metal surfaces, notably oxygen and thus scuffing would be associated with the rate of oxide formation and destruction. In the 1950's another major development in the field of tribology was started which recognized and understood elasto-hydrodynamic lubrication (EHL) became the focus of study and it was assumed that a system is in danger of scuffing when the thickness of the fluid film between the surfaces. Recent fundamental scuffing studies related to air conditioning compressors under dry sliding conditions were performed by Sheiretov, who proposed a process leading to subsurface failure, which eventually led to scuffing. Further studies carried by Yoon focusing on scuffing under starved lubrication conditions (typical conditions for air conditioning compressors), suggested that scuffing was related to shear failure of the bulk material which was caused by formation of macroscopic adhesions at the sliding interface. In these recent studies the effect of surface topography on scuffing has not been treated thoroughly. Further more their approach was based on macro-tribological experiments and meso-to-micro analysis methods. This was intentional since the surface roughness of typical engineering surfaces is large with Ra values from 0.1 to 1 μm, thus the previous researchers were seeking average effects in their studies. Also earlier studies did not examine the progression leading to scuffing. In the present study we investigate, first; the progression of surface topography and respective change in surface parameters with tribological testing leading to scuffing; second, changes in chemical composition of the surface and near surface layers of the sample at the micro and nano-meter scales, and investigate its relation to scuffing, this study differs from the ones carried out by its predecessors (Sheiretov, Yoon) in that it tracks topographical and chemical changes of the interface surface of the (softer) aluminum disc as it progresses form its virgin state to its scuffed state. Furthermore the analyses are carried out using macro to nanometer scales and techniques. To our knowledge this is the first such comprehensive study that will investigate the use of techniques that are typically used in semi-conductors and MEMS applications, whose surfaces are by several orders smoother than the engineering surfaces that will be used in this study.

A shoe-on-disc geometry, which is used to carry out the experiments consists of a steel shoe on aluminum disc and in an approximate simulation of a swash-plate/shoe contact in an automotive swash--plate compressor. The High Pressure Tribometer (HPT) is used to simulate the progression of wear conditions. The refrigerant used in this case is R410A with a POE lubricant. Once the experimental samples have been tested on the HPT, two sets of analytical tests are run, the first to measure the surface roughness and extract the statistical parameters, and the second to analyze chemical composition of the surfaces and the nano-meter range sub-surfaces. Based on the study it is suggested that the use of the micro to nano meter range scales in analyzing engineering surfaces is appropriate and correlates well to the macro to meso scale wear results. Thus the goal of this thesis

Is to investigate the evolution of both the topographical and chemical characteristics as the surface of an aluminum alloy is worn out in a swash plate compressor using macro to nano-scales.

Table of Contents

List of Figures

Page

List of Tables

Chapter 1

Literature Review

Man's relentless pursuit for perfection is hindered by friction, which is the cause of wear and one reason for imperfection. As some parts in motion are subject to severe wear, they fail and can no longer perform their function efficiently, at this stage they are said to be scuffed. Studies to better understand scuffing began approximately sixty years ago, when it was postulated that scuffing occurs when a critical temperature of the surface is reached, at which desorption of surface films occurs (Blok, 1937). Extension to this hypothesis was proposed suggesting interaction of chemically active species with the metal surfaces, notably oxygen. This led to a hypothesis that scuffing is associated with the rate of oxide formation and destruction (Cuotiongco *et al,* 1994). In the 1950's another major development in the field of tribology was started which recognized and understood elasto-hydrodynamic lubrication (EHL) (Grubin, 1949). EHL became the focus of study and it was assumed that a system is in danger of scuffing when the thickness of the fluid film between the surfaces becomes less then the average height of asperities on the sliding surfaces (Dyson, 1976). The major problem with the desorption and hydrodynamic approaches is that the effect of mechanical properties of contacting surfaces is not taken into account. In order to solve this problem it was proposed to use a parameter, plasticity index which is a measure of the amount of surface plastic deformation due to contact between asperities (Greenwood and Williamson, 1966). However studies carried out by Park and Ludema (1994) show little correlation between plasticity index and scuffing. A breakthrough in understanding of scuffing came from a recent study suggesting bulk subsurface failure as a cause of scuffing (Somi Reddy et al., 1995). To better understand the fundamentals of scuffing without external variable, scuffing under dry sliding conditions was studied by Sheiretov (1997), who proposed a process leading to subsurface failure, which eventually led to scuffing. Further studies carried by Yoon (1999) focusing on scuffing under starved lubrication conditions, suggested that scuffing was related to shear failure of the bulk material which was caused by formation of macroscopic adhesions at the sliding interface. Little work has been done suggesting the part played by surface parameters in scuffing of metals surfaces, In the present study we investigate at the progression of wear and respective change surface parameters, and explore the effects of these changes on scuffing. To better understand the objectives and scope of this study, we first take a brief introduction into wear and scuffing, followed by summaries of work done by Sheiretov (1997) and Yoon (1999), who have established the foundation upon which this study is to be carried out. In this study we intend to either confirm, or refute the fact that scuffing occurs as a result of sub-surface damage, which propagates onto the surface. We also intend to pioneer the study of rough surfaces at the nanometer scale contrary to the more popular micrometer scale.

1.1 Wear

Wear is the progressive loss of substance from an operating surface of a body occurring as a result of relative motion at the surface. The four main wear mechanisms are adhesion, abrasion, fatigue and corrosion. Other forms of wear are fretting, erosion, cavitation erosion and impact. Wear can be characterized either by physical and chemical conditions of material removal or based on the appearance of the worn surfaces (Burwell, 1957). It is also important to understand that friction and wear are not intrinsic material properties but are characteristic of the engineering system. Any change in load, speed, or environmental conditions can change the dominant wear

mechanism of the surfaces in contact (Czichos, 1974). The observance of a worn surface can only help determine the final stage of the wear phenomena and therefore cannot be used to track the wear mechanisms involved. In the following paragraphs the four wear mechanisms are briefly described.

1.1.1 Adhesive Wear

Adhesive wear occurs whenever one solid material is slid over the surface of another or under load and removal of material takes the form of small particles, which are usually transferred to the other surface but may come off in loose form. The tendency of contacting surfaces to adhere arises from the strong attractive forces set up whenever atoms come into intimate contact. The theory of adhesive wear is based on the adhesion theory of friction, which was originally proposed by Bowden and Tabor (1950) and formulated as a semi-empirical law by Archard (1953). In this theory, it is assumed that when asperities come into contact, they adhere strongly to each other to form asperity junctions that must be broken if relative sliding is to take place, the weakest point of the junction will break first, which may be either at or away from the original interface of the two materials. If the break occurs at the interface, no wear particles are formed, but if it occurs in either material, then a particle of this material will be transferred to the counter face. The transfer of material is normally from the softer to the harder material, but may also occur in the opposite manner under certain conditions. This theory only explains material transfer and not the formation of loose wear debris. Adhesion is favored by clean surfaces, non-oxidizing environments, and by chemical and structural similarities between the sliding pair. The breakage of the junction at the original interface subjects asperities to stress cycles, which may ultimately cause the creation of a wear particle by a fatigue mechanism. Wear of the harder surface occurs when the hard material has some “local regions of low strength" inside the asperities, and occasionally fracture takes place in these weak regions rather than in the softer counter face.

Experimental results show that the adhesion wear theory cannot explain all forms of wear, as it was first conceived, however, it is sufficient to conclude that adhesive wear may play a major role in some sliding situations. Adhesion could become a dominant wear mechanism under vacuum, inert atmospheres or when the temperature at the asperities is high enough to promote asperity adhesion (Rabinowicz, 1971). But under many practical situations the presence of contaminants on the surface or in the environment limits the extent of the phenomenon. Increasing the hardness of the surfaces, and reducing the real area of contact, thus reducing adhesive force, can minimize adhesion wear. The adhesive strength of pure metals is expressed as a function of their ability to form solid solutions, many surface diffusion treatments enhance wear properties by chemical contamination to produce non-adhesive or anti-welding characteristics. Wear under adhesive conditions is subjected to sharp transitions in behavior.

Oxide forming metals are characteristic to mild wear, a transition from mild wear to severe occurs when the protective surface oxide produced at lower loads breaks down.

‘Laws’ of Adhesive Wear

Archard, was the first to derive an expression for rate of adhesive wear. It is assumed that the real area of contact comprises a number of circular contact spots each of radius a. The area of each contact spot is pa^2 and,

assuming plastic deformation of an ideal elastic-plastic material, each contact supports a load of $pa^2 H$, where H is the yield pressure or hardness. The total load is $W= Npa^2 H$, where N is the total number of asperity contacts.

The counter face will pass over the asperity at a sliding distance $2a$ and it is assumed that the wear fragment produced from each asperity is hemispherical in shape and of volume $2pa^3/3$. The wear volume dQ produced by any asperity contact in unit sliding distance can be expressed as $dQ = pa^2/3$, the total wear volume per unit sliding distance is $Q= Npa^2/3$. The total wear volume, w, depends on the sliding distance s.
The final relationship derived from the equations is:

$$w=K Ws/ H \qquad \text{(Equation 1.1)}$$

where K= wear coefficient, and the factor 3 is a shape factor (in this case it is applicable to the assumed circular junctions and hemispherical fragments). The junction size does not enter the final expression as a consequence of the assumption that the size of the fragment is that of the contact junction and that the probability factor does not depend on the size of the junction.

The wear coefficient K is derived experimentally by running tests and then tabulated for different materials which may vary in magnitudes of about 10. The wear rate increases catastrophically at a critical load, which corresponds to a nominal pressure (the load divided by the nominal contact area) approximately equal to or slightly less than the bulk yield stress. This transition corresponds to the point at which the whole surface begins to deform plastically, so that the asperities can no longer be considered as independent contacts.

1.1.2 Abrasive Wear

Abrasive wear occurs when hard particles penetrate or plough into a surface or sub-surface of material, displacing it in the form of elongated chips. During the process, a smooth surface becomes roughened with fairly regular grooves, with or without loosely attached metallic debris. Abrasive wear can be divided into two main groups, two-body abrasion and three-body abrasion. In the two-body abrasion a rough hard surface slides against a relatively soft counter face, whereas in the three-body abrasion rough hard particles trapped in the contact cause one or both surfaces to be abraded (Burwell, 1957). The first, generally operates under low stress conditions, with little breakdown of particle size of the abrasive, while the latter one is constituent of high stresses. Nonetheless, three-body abrasion situations are usually less severe as the abrasive may also roll in the contact, producing no wear particles. If the hard, sliding surface is smooth, then abrasive wear of the two-body kind can be suppressed. Similarly, three-body abrasive wear does not take place when the particles are small or when they are softer than the sliding materials. Hence a sliding system can be initially free from abrasive wear, however, as sliding progresses, abrasive wear may become a problem due to the wear debris which is often made harder by oxidation or work hardening (Childs, 1988). Accumulation of this debris at the contact will lead to three-body abrasion. The total wear volume can be related to the load, sliding distance and hardness according to the adhesive wear equation. The inverse proportionality to hardness is true only for pure metals, while the relationship becomes more complex as the microstructure of the alloy is varied (Suh, 1997).

1.1.3 Fatigue Wear

Fatigue wear can be classified into two; macroscopic and microscopic fatigue wear. Fatigue wear is associated with non-conforming loaded surfaces, such as those found in rolling contacts, and is usually referred to as

surface fatigue wear. On the other hand microscopic fatigue wear occurs at the contacts between sliding asperities. In both cases, repeated rolling or sliding over a track must take place. Rolling contact fatigue is characterized by the formation of large wear fragments after a critical number of revolutions, with no progressive visible wear due to adhesion or abrasion prior to failure. In surface fatigue wear, the coefficient of friction is negligible since no direct solid-to-solid contact occurs. Metallographic cross-sections of rolling contact surfaces may reveal little or no evidence of the highly deformed layer, which may be observed in the case of sliding. The wear mechanism occurs by fatigue crack propagation and formation of surface and subsurface cracks. Since the fatigue process is controlled by deformation, void nucleation and crack propagation, the microstructure of the material and the state of stress are two important parameters of the wear behavior. Such micro-structural parameters as hardness, number and morphology of second-phase particles or inclusions control the fatigue process. At the asperity level, the accumulation of residual stresses necessary for shakedown is far more difficult than in macroscopic rolling and consequently the fatigue limit will be closer to the point of first yield. Owing to the much higher friction traction that occurs in sliding contact, the plastic deformation zone may reach the surface at much lower stresses. The number of contacting asperities subjected to fatigue cycles can be roughly estimated through the plasticity index (Greenwood & Williamson, 1966). In fatigue wear, the volume of worn material has been found to be proportional to the applied load and the sliding distance as suggested by the Archard's equation. The inversely proportionality with hardness holds only for pure metals, as seen both for adhesion and abrasion. The wear factor can be interpreted in terms of the number of cycles needed to cause the detachment of a wear particle.

The Manson-Coffin fatigue equation relates fatigue life to the plastic strain increment during each cycle, and equations derived from this can be used to estimate fatigue wear (Fretting wear is an example of fatigue wear on a micro-scale). The fatigue wear mechanism explains wear of a harder material by a softer counter-face as well as the formation of loose wear debris, which is a weakness in the abrasion model. The wear mechanism depends on the hardness ratio of the sliding pair, that is, when one material is much harder than the other, the hard asperities will penetrate the softer surface and plough grooves as sliding progresses. The softer surface will be subjected to abrasive wear, while fatigue wear may occur within the harder surface if the level of stress at the surface is above one half of its hardness. When the hardness ratio is such that both surfaces remain nominally elastic (plasticity index below or equal to 0.6), both asperities will be subjected to subsurface plasticity and fatigue (Arnell, 1991). Ideally both surfaces experience an identical number of fatigue cycles but a harder surface will require a higher number of cycles to produce a wear particle and therefore will wear at a lower rate.

1.1.4 Corrosive Wear

Corrosive wear occurs when a part is subject to a corrosive agent, which may be either in a liquid or gaseous state. The products of corrosion form a film on either surface which tends to slow down or even arrest further corrosion and may also protect the surface from wear phenomena. However, abrasion may wear the film away and the cycle of reaction and removal can be repeated indefinitely (Cavatorta, 1998). Oxidation wear is the most dominant form of corrosive wear.

Oxidation of sliding surfaces is usually beneficial in that the oxide film prevents metal-to-metal contact, mitigating adhesion. In cases of low cycles, the oxide is worn out as fine debris and replenished, protecting the

underlying metal layer. The effect of corrosion does not depend on the oxidation rate only. The oxides of most metal, including iron and aluminum, have volumes that are significantly different from those of their parent metals. Therefore, oxide formation develops stresses in the oxide, which increase with film thickness. In static oxidation, the film can fail at a critical thickness either by blistering, when the stress within the film exceeds the strength of the adhesive bond between oxide and substrate, or by cracking, when the oxide fails in tension. A very important parameter for the stability of the oxide is the substrate/oxide hardness ratio. This is due to the fact that, a hard substrate provides good support for the film, whereas a softer substrate is likely to deform plastically, at least at a local level, and thus effectively leaving the thin brittle film unsupported.

1.2 Scuffing

Scuffing is the collapse of lubricant films, destruction of physically or chemically adsorbed films, breakdown of the oxide layers, local thermal expansion of the asperities, plastic flow of asperities, accumulation of wear debris at the sliding contact interface and subsurface material failure (Sheiretov, 1997). Scuffing is generally defined as "localized damage caused by the occurrence of solid-phase welding between sliding surfaces without local surface melting" (Spikes, 1974). Several hypotheses have been placed forward to better understand wear and scuffing phenomenon, however a complete understanding has yet to be established.

Pressure, velocity, temperature, lubrication, surface topography, materials and metallurgical aspects, and surface coating are some of the factors that affect the rate and intensity of scuffing. A study carried out by Cavatorta (1998) investigating the effects of these parameters are summarized below:

As the pressure increases the surface is likely to scuff faster, while the load carrying capacity decreases with increase in temperature (with all other parameters being constant). As velocity increases, the thickness of fluid films decreases, therefore there is a critical velocity below and above which scuffing would occur more easily. The effects of lubricant additives depend on the type of lubricant. Surface roughness affects the magnitude of real area of contact, the contact pressures, which in turn influence the scuffing process. One of the approaches to reducing scuffing has been the use of some form of surface coating or other surface treatments on the sliding components.

In this part of the work we will summarize the important findings of both Sheiretov (1997) and Yoon (1998), and then progress to establish objectives that were not established by them. Findings from both Sheiretov's and Yoon's work are used as foundations for both experimentation and analysis of our results.

1.3 Study of Scuffing Under Dry Sliding Conditions by Todor Sheiretov (1997):

1.3.1 Introduction

Todor's research focused on two major goals, first, was to obtain a more complete set of experimental data for scuffing behavior of several aluminum alloys, and second to study the physics of scuffing phenomenon, evaluate existing hypotheses for scuffing under dry sliding conditions and explore the prospective for a theoretical description of scuffing. The specific procedures and criteria of the study are listed below.

1.3.2 Experimental studies

The experiments in this study were conducted in a specially designed tribometer, which allowed accurate control of the environmental conditions. An area contact (two pins-on-disk) geometry was used to study scuffing. Three combinations of pin sizes and sliding radii are tested, and five different materials were used for the pins which

were; pure aluminum, die cast hypereutectic silicon-aluminum alloy (390-T6), extruded Bi-containing eutectic silicon-aluminum alloy (DHT-3), 1018 steel, and Si-Pb brass. These materials were slid under dry sliding conditions against 1018 carburized steel disks. Most of the tests were conducted at a constant sliding velocity, while the load was increased stepwise. The instrumentation used to identify scuffing provided run-time records, coefficient of friction, sub-surface temperature, wear, electric contact resistance, and load history. The mechanisms leading to scuffing under dry sliding conditions were studied by examining the surfaces, sub-surfaces, wear debris and by quantitative measurement of the average subsurface plastic deformation and the thickness of surface layers. The surfaces of the specimens were examined by optical and electron microscopes and X-ray photo-electron-spectroscopy. The wear debris and sub-surfaces of specimens undergoing scuffing were studied using microscopy. Chemical composition of the sub-surfaces was studied using Auger Electron Spectroscopy, while subsurface plastic deformation was measured by testing specimens with brass inserts positioned perpendicular to the direction of motion. After the test, the specimens were cut parallel to the direction of sliding to reveal the deformation of the brass-aluminum interface. The results of the experimental studies can be summarized as follows:

Scuffing under dry sliding conditions is due to a subsurface failure. The processes leading to scuffing seem to involve the following events: Accumulation of plastic deformation, formation of voids and cracks in the subsurface, coalescence of voids, propagation of subsurface cracks and removal of sections of the surface, unstable decrease of the load bearing area, removal of protective layers from most of the surface, and finally formation of cold welds.

For the tests conducted in air, at a given environmental temperature, specified contact geometry and loading history, the contact pressure at scuffing decreases with the sliding velocity. Scuffing is strongly system-dependent, in that, changes in the geometry of the test specimens lead to shifts of the PV (Pressure Velocity) curve. Scuffing is a time-dependent phenomenon, above a certain critical PV, the time to Scuffing decreases with the PV. This suggests that scuffing occurs when a critical amount of damage is accumulated in the material. The PV at which scuffing occurs depends on the previous loading history. The sub-surfaces of specimens tested under dry sliding conditions have three characteristic regions; these are, transformed material, plastically deformed material, and undisturbed material. At a constant PV, both the thickness of the transformed layer and the amount of plastic deformation increase with time until they reach equilibrium levels. The thickness of the transformed layer and the depth of the plastically deformed region increase with the PV.

1.3.3 Theoretical studies.

The main goal of the theoretical studies was to evaluate the existing hypotheses for scuffing and to construct a hypothesis and a criterion, which would explain most of the experimentally obtained results. A finite element simulation of the contact of rough surfaces, statistical methods for the alignment of surface profiles and analytical correction factors for deviations from the infinite half-space approximation was used.

The local subsurface stresses, temperatures and strains were estimated by applying several numerical methods some of which are explained below. The transient subsurface temperatures were calculated using a simple finite element model, while the strains were obtained from a finite difference method. The stresses were calculated on the basis of the infinite half-space approximation and information about the surface pressures and areas of

contact. The latter is provided by the finite element method for the contact of run-in surfaces. Experimental and theoretical results were used to evaluate several hypotheses for scuffing, applicable to sliding under dry conditions, are evaluated. These hypotheses were grouped according to their major assumptions. The first group of hypotheses related scuffing to a critical temperature condition while the second postulated that scuffing occurs when the shear stress at a critical depth in the material exceeds the shear strength. The third related scuffing to damage caused by extensive plastic deformation. Experimental data was used to deduce a final hypothesis that was constituted by parts of the mentioned hypothesis.

Sheiretov's major findings from the theoretical studies are summarized below:

The real contact area increased linearly with the applied load, while the maximum and the average contact pressures were weak functions of the load. The maximum pressure initially increased slightly with the load and then saturated at about 60% of the scuffing load. The average contact pressure was approximately constant for the whole range of test loads. The "real contact area" increased slowly with load, however, a sharp increase in "real contact area" occurred right before scuffing. The mechanical and the thermal parts of the solution for the subsurface stresses and temperatures can be decoupled. This is due to the small effect of flash temperatures, which were negligible compared to the bulk temperature. The low flash temperatures were a result of relatively small heat fluxes. The thermal gradients near the surface were higher than the gradients in the bulk, however, these fail to produce significant temperature differences. For aluminum, most of the strain accumulated in a contact period occurred early in the period. The total accumulated strain was a weak function of the period's duration. If annealing and dynamic re-crystallization occur between contacts, the accumulated strain is a stronger function of the number of contact periods. The results for the strain accumulated in a single contact period cannot be generalized to account for multiple contacts due to the lack of information for the changes occurring in the material between contacts. The hypotheses relating scuffing to a critical thermal condition are phenomenological in nature and do not provide an explanation for the mechanism of scuffing. These hypotheses consider a "static" state of the material and cannot explain time and load history effects. Blok's flash temperature concept deviated from the experimentally observed data. The results from this study showed that the surface temperature at scuffing was not a material property, it is depended on the geometry, the loading conditions, and the environment. The competitive oxide formation and destruction hypothesis is also phenomenological and in its present form cannot describe adequately the complex dynamics of protective films formation and destruction. The critical shear stress hypothesis is a pioneering approach relating for the first time scuffing to sub-surface failure. However, the shear stresses at the critical depths were not high enough to cause the predicted bulk failure. The proposed hypothesis for scuffing provides a qualitative explanation of the experimental results, which include the effects of material, temperature, contact geometry, time, loading history, and environment.

1.3.4 Major Accomplishments of Sheiretov's Study

Several accomplishments of Sheiretov's work contribute to a better understanding of the scuffing phenomenon. The most important accomplishment of Sheiretov's study was the development of a new hypothesis for scuffing, in this hypothesis, scuffing is related for the first time to the initiation and propagation of deep subsurface cracks. The observations of sub-surfaces of specimens undergoing scuffing provide the proof that these

cracks are present before the final adhesive phase of the scuffing process. The proposed hypothesis also provides an explanation of the existence of several stages of the scuffing process which are associated with the initiation and propagation of sub-surface cracks. The gradual removal of whole sections of the load-bearing surfaces before the final adhesive stage was also a new finding, which provides an explanation for the unstable and catastrophic growth cracks in areas of bare metal, leading to the final stage of scuffing. The sequence of events leading to scuffing is as follows: Accumulation of plastic deformation in the sub-surface, nucleation of cracks and voids, coalescence of voids and propagation of cracks, formation of cold welds

Another contribution from Sheiretov was reliable reproduction and identification of scuffing under laboratory conditions. An experimental procedure was established which could produce reliable consistent results. With the experimental procedure friction monitoring, wear, temperature, and electric contact resistance measurements are possible.

The equilibrium stress-strain curves reported in the literature failed to explain the accumulation of plastic deformation on a local basis, especially close to the surface. On the other hand, the predictions of the simple model based on strain sensitivity, developed in the study, are at least qualitatively correct. This points to the importance of the strain rate effects, which have not been discussed previously in the studies related to sliding contacts.
After Sheiretov's work, Yoon progressed to suggest a new hypothesis explaining scuffing. Below is a summary of Yoon's work.

1.4 Study of Scuffing under Starved Lubrication conditions by Hyung Yoon (1999)

1.4.1 Introduction

The main objective of Yoon's study was to better understand the scuffing process under starved lubrication conditions. The project has two main goals, first, to obtain data for the scuffing behavior of 52100 steel shoes/390-T6 AL plates, and the second to examine the fundamental failure mechanism of scuffing processes at the micrometer scale. Some of the conclusions made from the experiments are stated in this section. Yoon deduced that for every sliding velocity used, the scuffing pressure increases as lubricant supply rate increases, the scuffing pressure obtained with flat shoes is higher than that obtained with crowned shoes and as the lubricant supply rate increases, the scuffing pressure obtained with crowned shoes is much higher than that obtained with flat shoes. This indicates that scuffing is a function of crown height and degree of starvation. When the contact is severely starved the dimple is detrimental because, for a given pressure, the peak contact pressure and temperature for the crowned shoe are higher than those for a flat shoe. If the amount of lubricant supplied at the contact is not enough, the dimple or grove acts like a reservoir.

During scuffing most of the original surface of the pin was removed to a depth of 2-3μm, nascent aluminum oxide was detected and had a thickness of about 6 micrometers using results from the SEM. In the un-scuffed region, oxygen present on the surface could be detected only up to 1μm depth, however, in the scuffed region oxygen was detected up to a depth of 6 μm. Three characteristic layers were seen in the cross-sections, transformed layer, plastically deformed layer, and undisturbed/elastically deformed layer. Below the transformed layer, the plastically deformed layer, the plastically deformed region typically reached a depth of 50-60μm.

1.4.2 Yoon's Proposed scuffing hypotheses

The hypotheses for scuffing can be subdivided in to three major groups. The first is mainly based on he assumption that scuffing occurs if some critical thermal conditions are reached at the sliding contact surfaces. The second is based on the breakdown of the main elasto-hydrodynamic lubrication films in sliding contacts. The third group of hypotheses is based on bulk material failure. These hypotheses assume that if a critical condition on the surface or below of the contacting bodies are reached, surface films or bulk material failures occur, which consequently leads to scuffing.

According to Yoon, the key to understanding scuffing was to understand the dynamics of protective film formation and destruction. In most lubricated contacts, films of several natures may be present at the sliding interface, building several lines of defense against scuffing. In general, the adsorbed films have low shear strength characteristics so that they can reduce the local temperature rise. The oxide films also have low shear strength characteristics and they protect surfaces from adhesion by preventing exposure of the bare metal. It was suggested that the sufficient condition for scuffing to occur was given by the destruction of the oxide layers due to plastic deformation of asperities. Based on the assumption that initiation of scuffing failure is caused by plastic shearing, it was also proposed that the formation of macroscopic adhesion leading to plastic shearing of the bulk material was responsible for scuffing. Yoon hypothesized that, when scuffing occurs, the local tangential traction at the sliding interface is higher than the bulk strength of the softer material, thus the softer material is sheared and transferred to the harder counter face. During the sliding process the surface is initially protected by various surface protective films formed at the tips of the asperities. These films prevent large-scale adhesion between the sliding surfaces, however, at certain critical conditions these films can be locally removed mainly due to high local pressures and temperatures, exposing bare metals, which can cause local microscopic adhesions. The bulk material failure due to plastic shearing, caused by the formation of extensive adhesions at the sliding interface, is considered as the final stage of the scuffing process. The processes leading to scuffing are explained in detail below: In mixed or boundary lubrication due to the high pressures and temperatures, lubricant breakdown can occur as the result of asperity interactions. If the local temperature is high enough, the thermal excitation of adsorbates increases resulting in a higher probability of their detachment from the surface.

After breakdown of the lubricant and adsorbed films (seen from contact resistance), the oxide films can still protect the surface from scuffing. If a high load is induced, the elastic limit of the softer material underlying the oxide layer can be reached locally, resulting in plastic deformation of asperities under the oxide. The plastic deformation destabilizes the protective oxide films formed on top of the asperities, and eventually causing shearing or chipping-off of these films. The contact of the exposed bare metal with the counter face will result in the formation of microscopic adhesions. Due to microscopic adhesion, the local surface tractions mainly shear off the tips of the asperities, resulting to mild adhesive wear, also know as microscopic scuffing.

Accumulation of cold welds eventually leads to formation of macroscopic adhesions. Upon application of separating forces to the adhered junction, failure occurs in the cohesively weaker metal, and this allows the cohesively weaker to be transferred to the cohesively stronger. For the conditions studied in this research, shear failures often occurred at a depth of about 1-2μm. Based on the above hypothesis, scuffing occurs when the surface

tangential traction (μP_{max}) at the interface exceeds the temperature dependent bulk shear strength (τ_S) of the material. The criterion can be expressed as:

$$\mu P_{max} \geq \tau_S (T)$$

where μ is the coefficient of friction and P_{max} is the maximum asperity contact pressure.

Yoon also came up with the following conclusions relating physical, geometrical factors to scuffing:

1.4.3 Shoe & Disc Geometry

1. For a given environmental temperature and specified contact geometry, the scuffing pressure increases as the lubricant supply rate increases and decreases as the sliding velocity increases.
2. PV = constant relationship seems to characterize the scuffing behavior of 390-T6 Al plate/52100 steel shoe contacts. The value of this constant increases as the degree of lubricant starvation decreases.
3. Scuffing is a function of crown height and the degree of lubricant starvation. Crowning is detrimental when the contact is severely starved.
4. When the contact is severely starved, a dimple or groove is also detrimental.
5. For the whole velocity range tested, the scuffing pressure of 390-T6 Al discs increases with improved surface finish.
6. For the sliding velocity used, surface roughness effects are more significant as the lubricant supply rate increases, i.e., scuffing of the smoother specimen is affected to a greater degree than that of the rougher specimen.
7. A skewness change from -0.34 to -1.26 for 390-T6 Al discs with the same surface roughness do not seem to improve their scuffing resistance.
8. For a given lubricant supply rate, the scuffing pressure of tin-coated 390-T6 Al discs is about three times higher than that of the uncoated discs. It is hypothesized that scuffing of tin-coated 390-T6 Al discs is caused by the removal of the coating, which leads to the formation of macroscopic adhesions between the exposed Al substrate and the steel counter-face.
9. For the velocities and lubricant supply rates used, the effects of socket geometry supporting the shoe on scuffing are negligible.

1.5 Objectives:

From the summaries above, Sheiretov concentrated on analysis of scuffing under dry conditions, while Yoon concentrated more on the lubricated conditions, however they both concentrated on sub-surface damage at the micrometer scale. Both Sheiretov and Yoon carried out all their analyses based on an average effect (by studying large areas of several micrometers) using the AES, which gave a good idea of the gross effects of scuffing. In this study we intend to take the analysis to the next scale, that is, the nanometer scale by utilizing techniques used for much smoother (semiconductors) surfaces. According to Yoon's study scuffing is predominantly caused by sub-

surface damage with little change on the surface topography, in this study we intend to either validate or refute this conclusion by studying the wear evolution of the Aluminum disc closely and by monitoring the changes in surface parameters. Below is a summary of the main objectives of this study:

10. To investigate into the changes in Surface topography as an Al390-T6 surface is worn out, and to validate or invalidate the existing hypothesis proposing that sub-surface damage plays the most important role in scuffing.
11. To apply nano-techniques into investigating chemical changes that occur on and below engineering rough surfaces.

By studying the change in surface topography we hope to observe the point at which surface damage occurs, and how it progresses to eventual scuffing. To achieve these objectives, experiments are carried out on AL390 –T6 discs, with 52100 steel shoes under starved lubrication conditions.

CHAPTER 2: HPT Experimental Set Up and Controlled Tribological Testing

2.1 Introduction

The HPT is an instrument that is used to run wear and friction tests, and is one that simulates the environmental conditions found in air conditioning compressors. This apparatus is used to perform friction and wear tests using a lower stationary sample in contact with an upper rotating sample. Figure 2.1 shows a simple schematic of the machine.

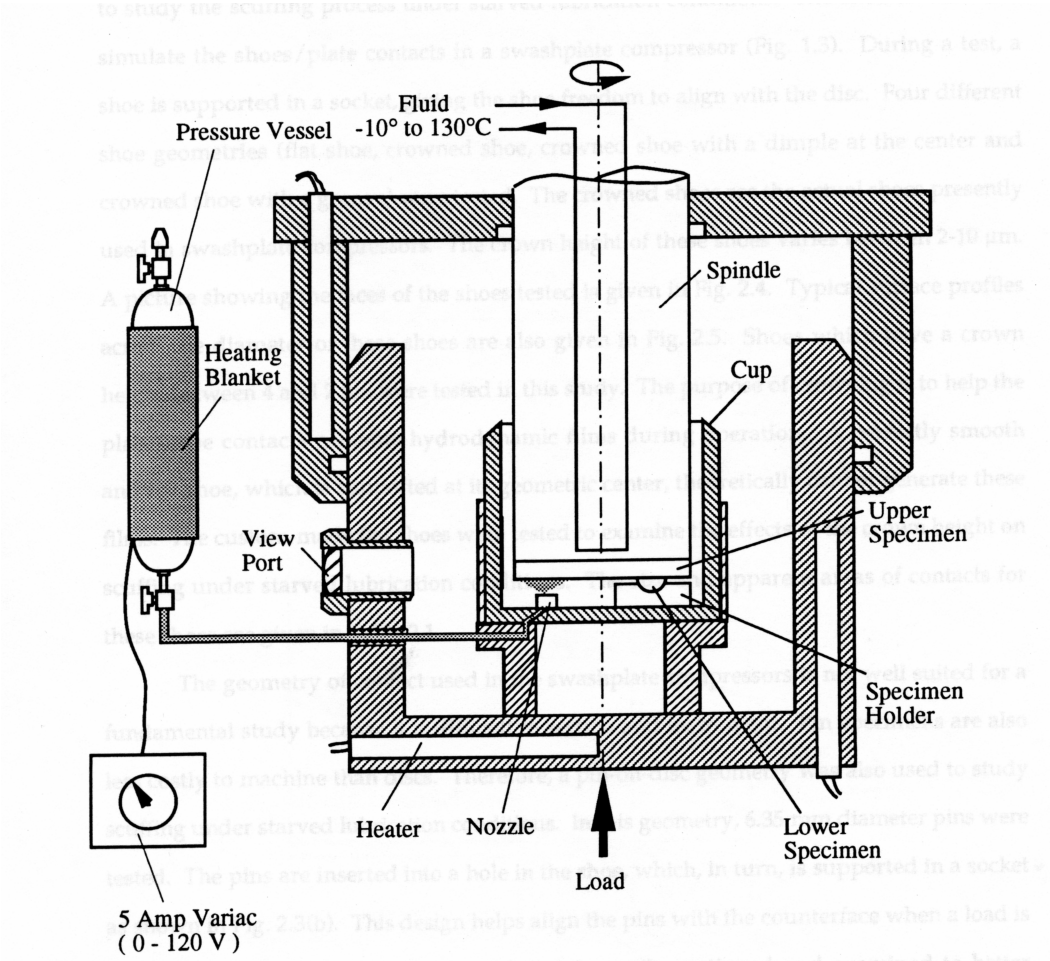

Figure 2.1, Schematic of HPT Pressure chamber and Lubricant supply system

The unit is capable of motion in two directions, the vertical or z-axis direction is used to access the samples, seal the high-pressure chamber, and provide a load on the test specimens. The rotary or theta-axis direction controls the rotary motion of the upper sample. These displacements can be controlled manually on a control panel or via the computer program. The lower stationary sample is mounted on a transducer module that measures the forces in the three orthogonal directions (Fx, Fy, Fz) and also the moment about the z axis. The absolute of the resultant of Fx and Fy is called Fr, and is the force of friction for generalized single point sliding. This positive value divided by the normal force, Fz, provides the coefficient of friction (AMTI, 1991).

The test chamber is contained in special pressure/vacuum (0.2 torr) housing capable of testing up to 250 psig. Chamber temperatures from -12°C to 121C°F can be attained by using a combination of heating and cooling systems. The desired temperature of the rotary contact specimen is obtained by pumping heat transfer fluid through the spindle. The temperature of the fluid is controlled within 0.1°C accuracy by an external unit, which is capable of maintaining constant temperatures (spindle) from 30°C to 130°C. The chamber heaters consist of one 400-Watt cartridge heater in the upper chamber and two 400-watt cartridge heaters in the lower chamber. The lubricant/refrigerant is supplied to the rotating contact specimen through a nozzle fed from a pressure vessel; the pressure is maintained by heating the pressure vessel. The average lubricant flow rate is determined by dividing the weight of the lubricant used by the test duration. A lead screw that is driven by a DC servo motor through a harmonic drive supplies the normal contact load. The specimen mounting system has been designed to be general and consists of flat lower and upper surfaces with threaded holes to accept any specimens or fixtures for specimens. During an actual test, the lower sample is brought into contact with the upper sample using the motor driven lead screw located at the bottom of the unit. The maximum recommended load for this machine is 1000 lbs, in addition at a maximum chamber pressure of 1.72 MPa, which corresponds to a 7000 lbs that are needed to keep the chamber closed. Figure 2.2 depicts schematically the four main subsystems that make up the tribometer. The first or the mechanical portion, which was described earlier, contains the pressure chamber, sample holders, load sensors, position locators, temperature cartridge heaters for the upper and lower pressure chamber and the two drive motors that provide the vertical and rotary motion. The second section is the power box. This system contains the power amplifiers, power distribution system, fuses and relays. The chiller is used to maintain non-test portions of the tribometer at 70°F, which is achieved by re-circulation chilled water in a closed loop. The last section is the control box, which contains the motor controls, amplifiers for load measurements, temperature controls and the microprocessor.

2.1.1 Contact Geometry

In this study, we use a pin on disc contact for the experimentation as shown in Figure 2.3. In this type of geometry thermal expansion of the specimen and other parts of the test rig do not increase any loading on the specimen (Yoon, 1999). In addition, the apparent area of contact does not change with time due to wear. Another advantage of this system is the fact that, as the rotating disc is the upper specimen, most of the wear debris falls at the base of the pins and the effect of debris accumulation from the experiment is eliminated. A photograph of the pin holder is shown in figure 2.4.

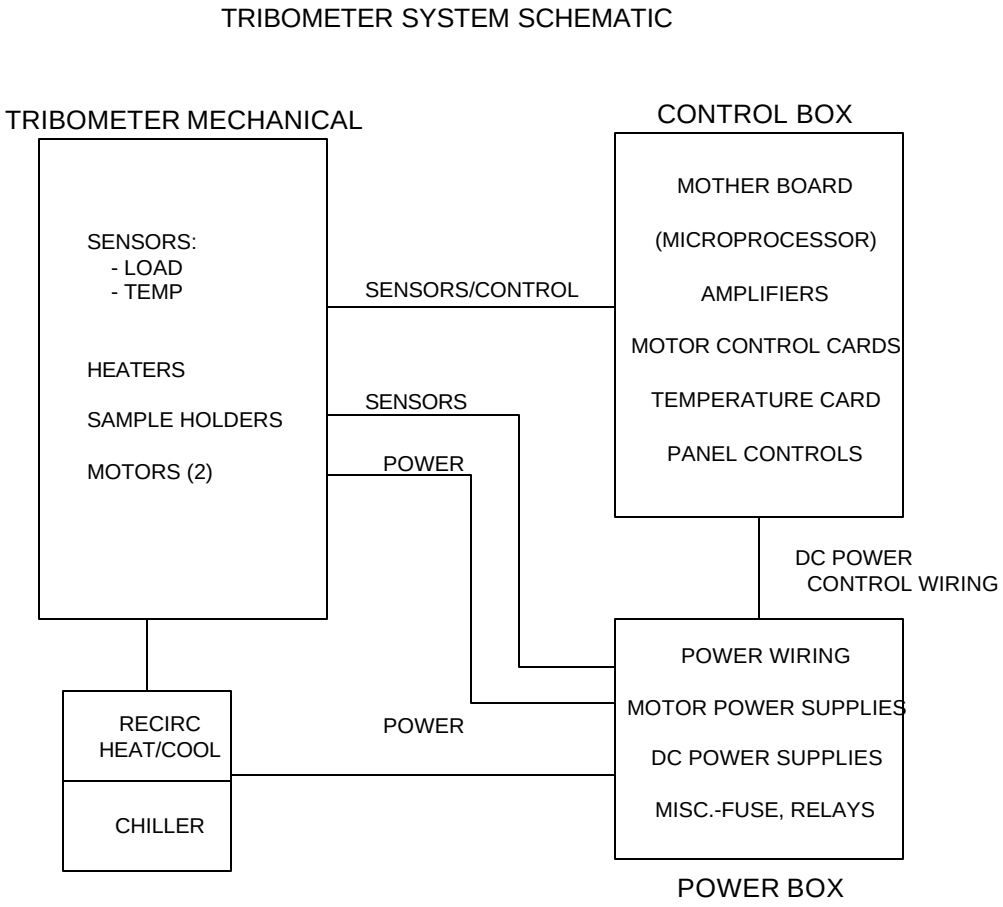

Figure 2.2, Four main sub-systems of the Tribometer.

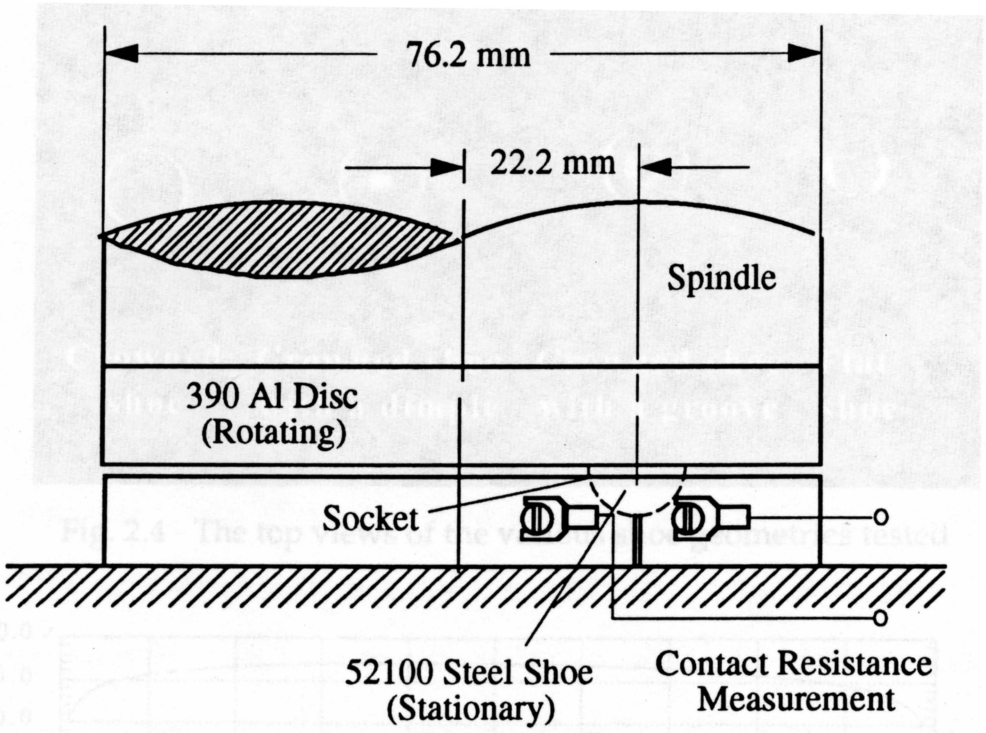

Figure 2.3, Contact geometry of disc on pin,

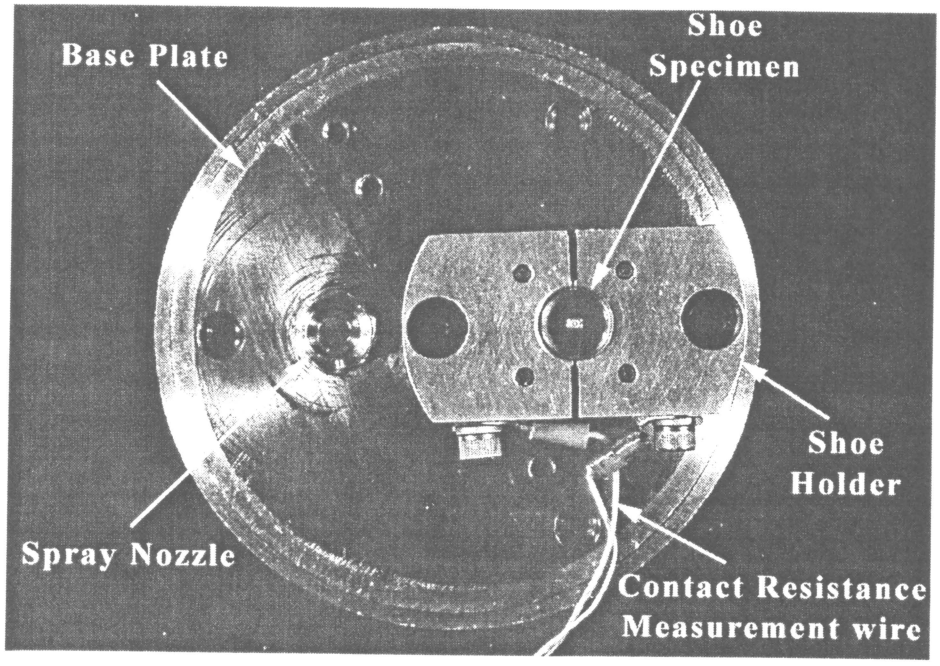

Figure 2.4, Setup for spraying nozzle and the shoe specimen holder.

2.1.2 Instrumentation

The instrumentation of the HPT includes a real-time output for the axial and friction forces, frictional torque, and the environmental temperature. In general, there are two ways that scuffing tests can be conducted in the HPT. One way is an endurance test, from which the time to failure is obtained for given constant load and velocity conditions. The more widely used procedure is the step-loading test because it requires a considerably shorter time. In this test, for a given constant sliding velocity, the load is progressively increased stepwise with a specified step duration until failure occurs.

The HPT is also equipped with a contact resistance measurement, a miniature thermocouple and an LVDT position sensor. The latter measures the relative displacement of the two specimens during the test, therefore allowing for a real-time measurement of wear (however we do not measure the wear rate). In particular, it monitors transitions in the wear rate that are indicative of transitions in the wear mode. However, under lubricated conditions, wear is often very limited and the scuffing condition is identified by transitions in friction, contact resistance, and subsurface temperature (AMTI, 1991) (the LDV data is not used in this study). Figure 2.5 shows a typical scuffing test experiment where the load is increased stepwise until scuffing occurs.

The electric contact resistance between the test specimens is commonly used as an indicator for transitions in different lubrication regimes. The large errors associated with connecting wires and fixtures have often limited its applications. The most common arrangement of a contact resistance measurement circuit is a two terminal circuit as shown in Figure 2.6 (a). The low sensitivity of the circuit allows only for detection of transition from complete separation of the specimens by a lubricant film, to a regime where asperity contact occurs. In boundary lubrication, surface contact occurs at all times, which clearly makes the two terminal circuit inapplicable. The contact resistance under boundary lubricated conditions is typically of sub-ohmic value, often dropping to $10^{-6}\ \Omega$ at scuffing. The measurement of such small resistance is not a trivial problem and requires the development of a special circuit, methods for noise suppression, and data processing software. Figure 2.6b shows the four-terminal circuit used in the study (AMTI, 1991).

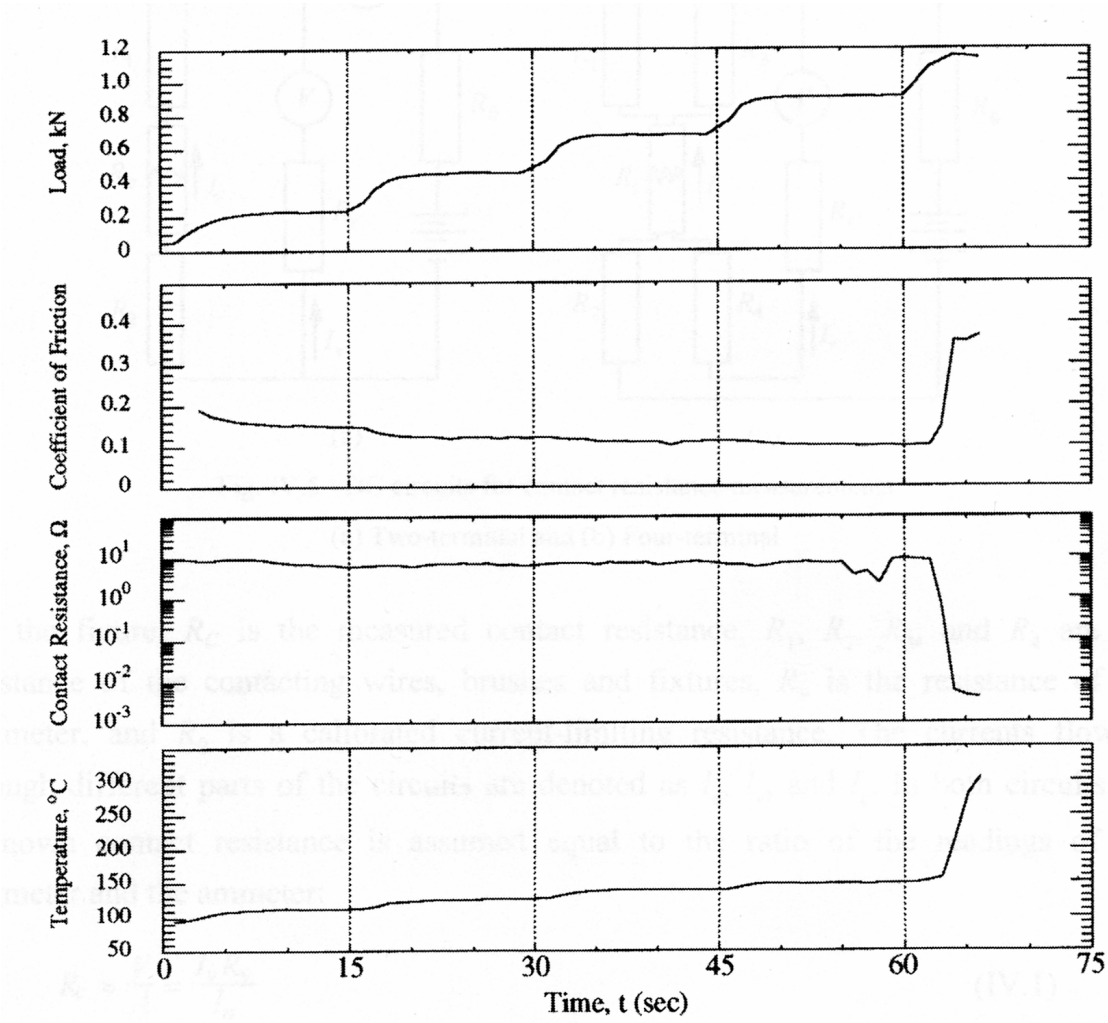

Figure.2.5, Typical scuffing experiment at the interface

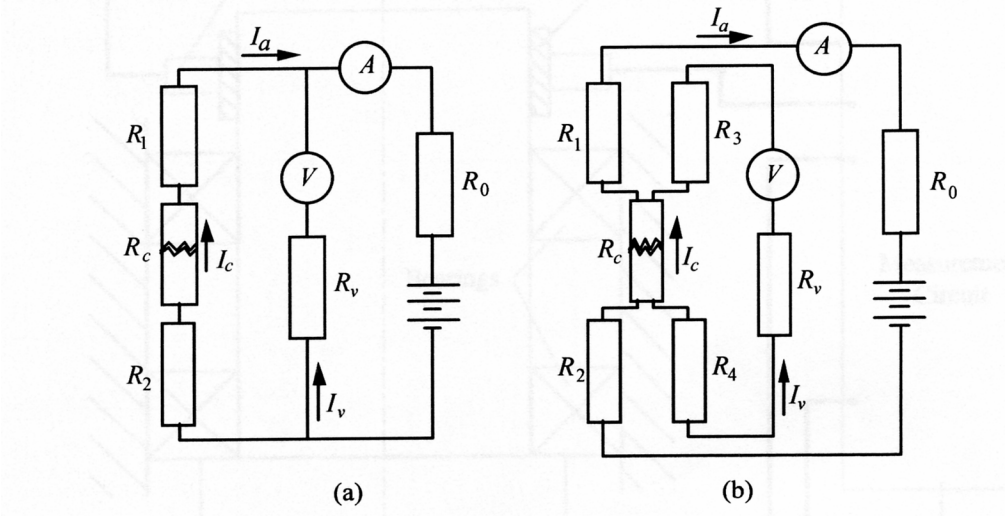

Figure 2.6, Circuit for measuring Contact Resistance (a) Two-terminal and (b) Four-terminal

In the figure, Rc is the measured contact resistance, R_1. R_2 R_3 and R_4 are the resistance of the contacting wires, brushes and fixtures, R_v is the resistance of the voltmeter, and R_o is a calibrated current-limiting resistance. The currents flowing through different parts of the circuits are denoted as Ia, I_v, and I_c. In both circuits the unknown contact resistance is assumed equal to the ratio of the readings of the voltmeter and the ammeter:

$$Rc = V/A = IvRv/Ia \qquad \text{(Equation 2.1)}$$

The very high sensitivity of the four-terminal circuit makes it susceptible to noise. The electromagnetic fields of motors and instruments induce voltages that can sometimes be comparable to the voltage of the signal. In addition, temperature rise at the contact introduces Seebeck thermocouple voltages that can also be significant. To eliminate these errors, the DC power source was continuously turned on and off by a computer controlled solid-state relay. The voltage measured when the power source was off is due to noise alone, while the voltage measured when the power source was on is due both to noise and contact resistance. The difference of these two voltages is the true signal. In the circuit used in this study, the software conducts the subtraction. Figure 2.7 shows the actual measuring circuit.

The surface temperature is a very important tribological quantity; its direct measurement in sliding interfaces is extremely difficult. In practical situations, thermocouples are often employed to measure temperature. The effect utilized in all thermocouples is known as the Seebeck effect. When two dissimilar metals touch each other a small voltage can be measured across the contact. This voltage is a function of the temperature at the junction. In a sliding system, the junction of interest is the sliding interface itself. Theoretically, with a proper calibration, the actual temperature at the interface can be obtained. However, oxidation of the surfaces, strain hardening of the surface material, poor junction connection, and high thermal gradients render the calibration practically impossible to achieve (AMTI, 1991).

2.1.3 Materials for the Test:

This section deals with specific properties of the materials used for experimentation. The discs used were aluminum 390-T6 with average hardness of 72HRB. The chemical composition of this alloy is as follows:

Alloying elements, % by weight							
Al	**Si**	**Cu**	**Fe**	**Mn**	**Mg**	**Zn**	**Ti**
76	**16.0-18.5**	**3.0-4.0**	**1**	**0.5**	**0.4-1.0**	**1**	**0.25**

The Ra of the surfaces of the virgin discs were 0.25-0.35µm, these parameters are further discussed in Chapter 3. The lubricant used in this case was a base POE, the refrigerant used was R410A. Appendix 1 looks at a study carried out by Cavatorta (1998) which discuses the performance of various materials under different conditions. The 52100 steel shoes used for this study have an average hardness of 62HRC and average surface roughness of 0.03µm Ra. The steel shoes were crowned in nature with a dimple as shown in the figures below.

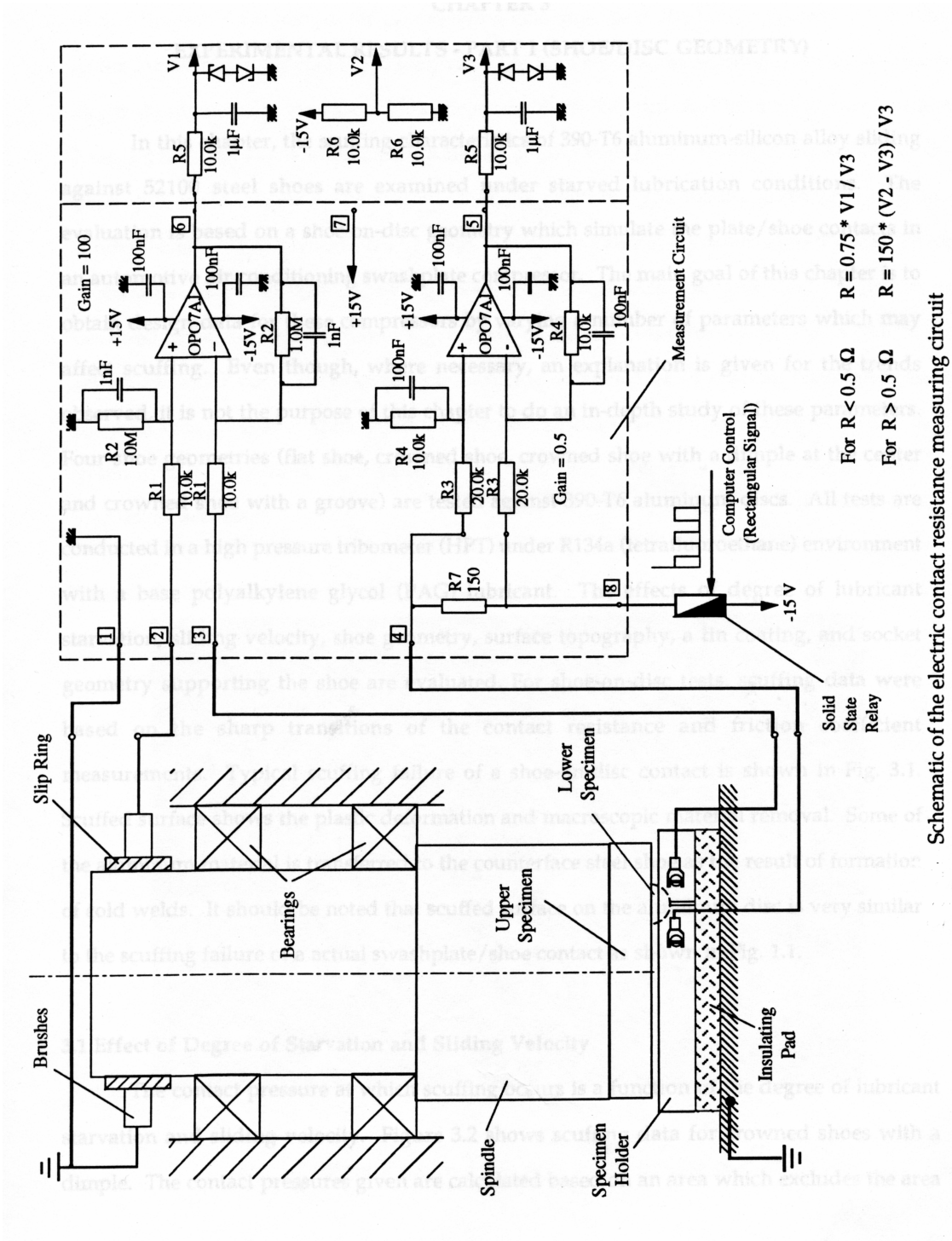

Figure 2.7, schematic of electric contact resistance measuring circuit.

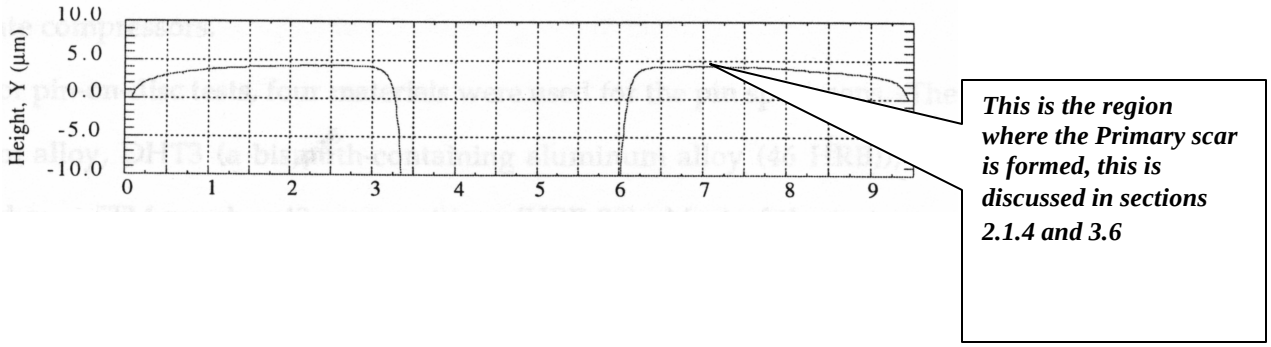

Figure 2.8, Typical surface profile of crowned shoe with dimple.

2.1.4 Summary of Experimentation

In the present study, the step-loading test procedure was used for the scuffing experiments. A 20lb load step and a step duration of 15 seconds was used. The 15-second step duration was chosen since, under starved lubrication conditions, a steady state temperature is reached after approximately 10 seconds (Yoon, 1999). The sliding velocity used was 30mm/minute. These parameters were chosen based on Cavatorta's study, and after conducting many trials to obtain repeatable scuffing results. In this study, scuffing was determined by sharp transitions of the contact resistance (indicating the destruction of surface films), friction coefficient transition. The process of stepwise loading eventually leads to scuffing failure, which causes sharp transitions of the contact resistance, and friction coefficient. At this stage, the load is quickly released and the test stopped. The time taken to scuff the sample was noted and three other tests were run with the same parameters, but the tests were stopped prior to scuffing at 0.25x Scuffing time, 0.5x Scuffing time and 0.75x Scuffing time.

Test Protocol Summary

1. Five Al-Si samples were selected, making sure they have little surface damage from scratches.
2. Sample preparation; The 5 samples were immersed in pools of Acetone, and ultrasonically cleaned for 10 minutes. They were then rinsed in alcohol and dried using a heat source. The samples were then placed in sealed containers to prevent contamination. Note; the specimen should be wrapped in aluminum foil and shouldn't be in direct contact with the plastic container for it will be subject to carbon contamination.
3. Initial surface roughness; The samples were marked and their surface roughness measured (see Chapter 3 for more details).
4. HPT testing; the five samples were to be tested as follows:
    - Sample 1; Virgin sample, no Tribological testing.
    - Sample 2; Sample was tested for a time corresponding to 0.25 x T (T = time to scuff).
    - Sample 3; Sample was tested for a time corresponding to 0.5x T.
    - Sample 4; Sample was tested for a time corresponding to 0.75x T.
    - Sample 5; Sample was tested until it scuffed, time taken to scuff (T) noted.

5. The operating conditions for the HPT were as follows;

    - Rotation Speed; 1030RPM (2.4m/s)
    - Step Load; 20lbs with initial load of 20lb
    - Disc Temperature; 121°C
    - Loading Interval; 15 seconds
    - 0.2 Torr Vacuum

6. After the testing, the samples are then ultrasonically cleaned as mentioned above, and profilometer scans to measure surface roughness are run similar to those on the virgin sample.

7. The roughness data is analyzed using a computer program (MatLab) and Greenwood and Williamson (1966) micro-contact parameters are extracted.

8. The samples are then cut into smaller sizes using a low speed diamond saw, and prepared for chemical analysis (prior to analysis they were ultrasonically cleaned again).

Steps 1-5 of the summary above were carried out in Chapter 2, while 6-7 in Chapter 3, and step 8 in Chapter 4. The photographs shown below were taken using a high-resolution (3.34Mpix) digital camera to show actual samples used for this study.

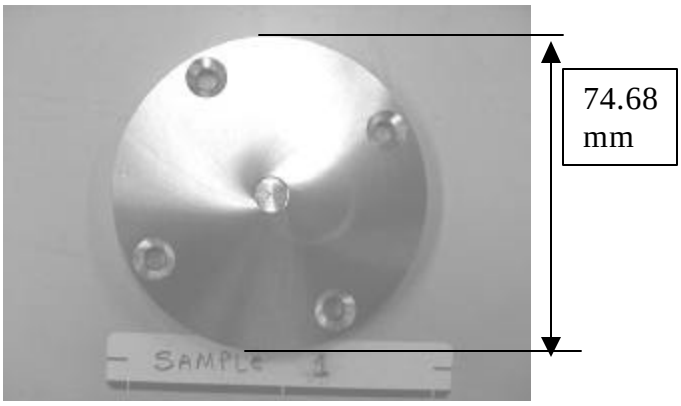

Figure 2.9, Image of virgin sample

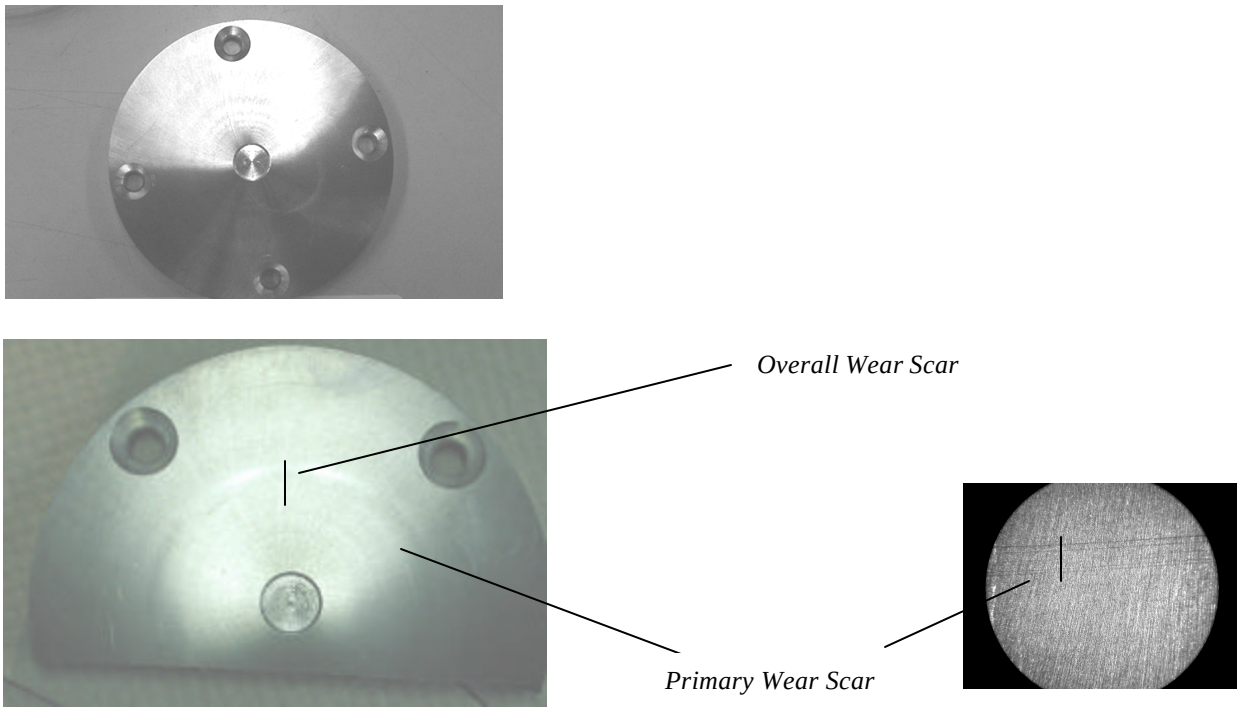

Figure 2.10, Image of Virgin (top) and Worn (bottom) Sample 2.

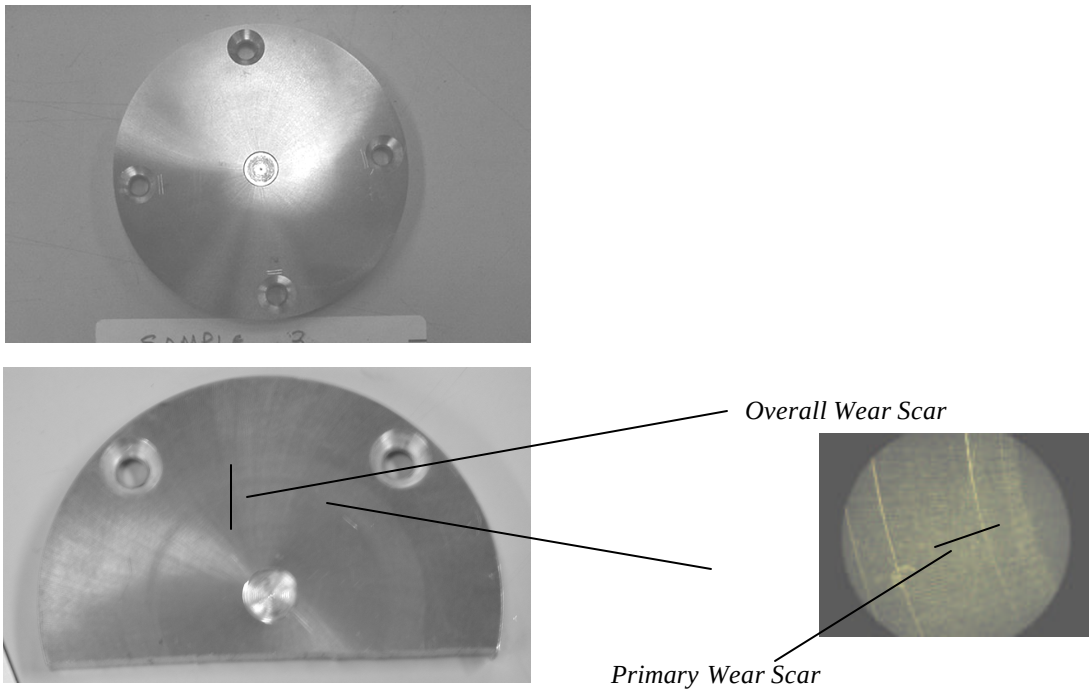

Figure 2.11, Image of Virgin (top) and Worn (bottom) Sample 3.

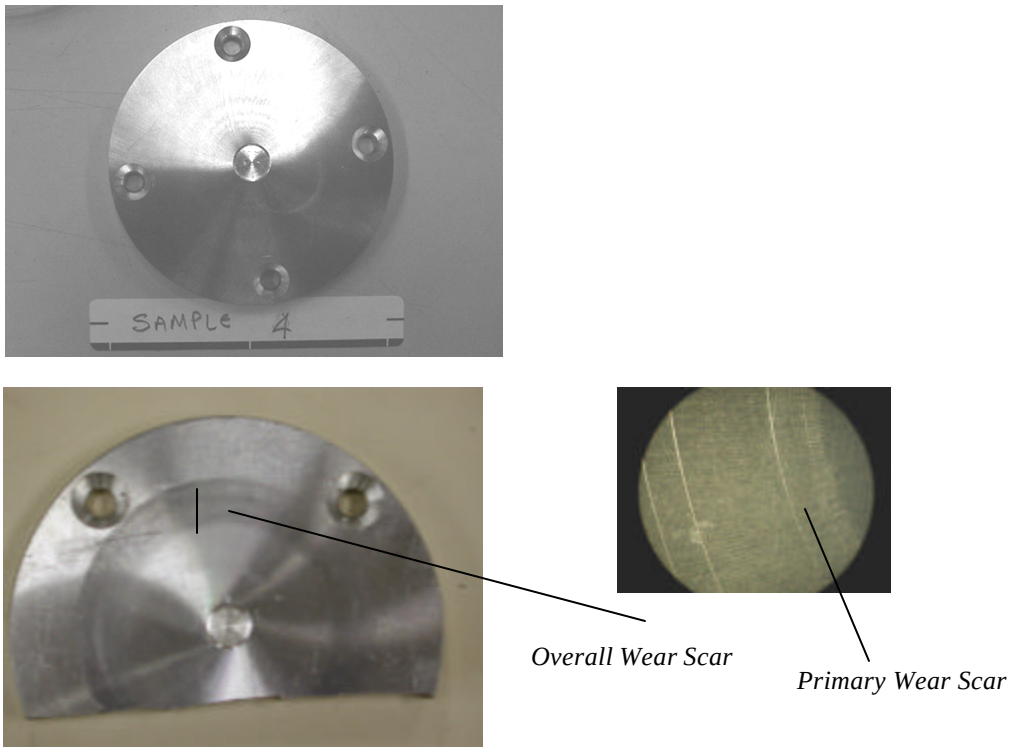

Figure 2.12, Image of Virgin (top) and Worn (bottom) sample 4.

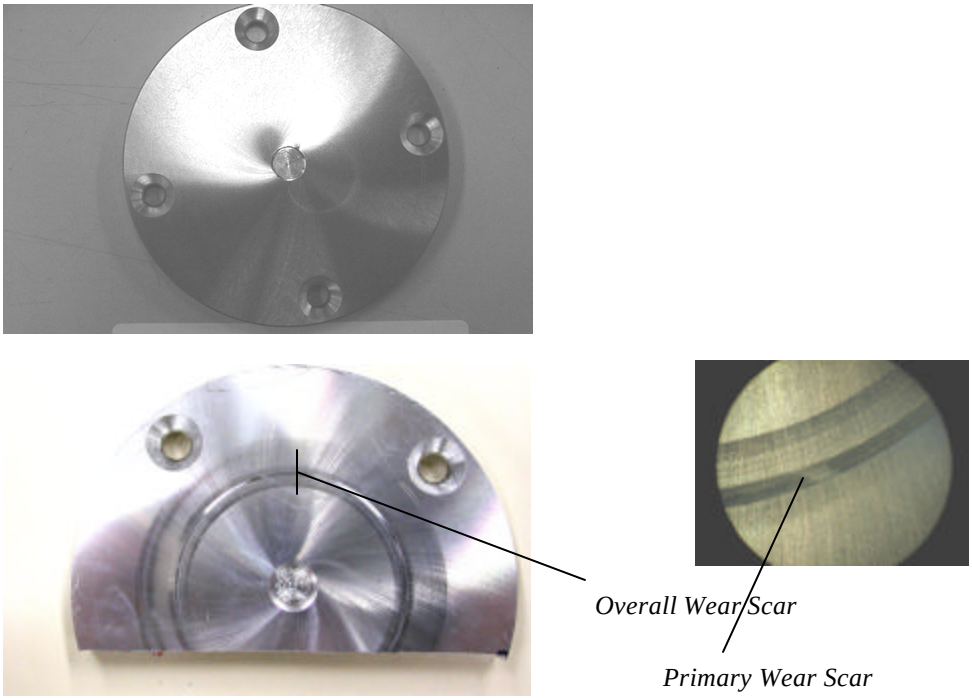

Figure 2.13, Image of Virgin (top) and Worn (bottom)Sample 5.

From the figures above a trend can be observed which shows vital evidence that the surface damage occurs soon after the sample is tested and this primary wear scuffs first. In figure 2.9, sample 2 shows development of a primary wear scar within the overall wear track. In sample 3 this wear track is still present, however the overall wear track becomes more defined at this stage. Sample 4 depicts a premonition that the sample would scuff and this will occur at the primary wear scar. Sample 5 proves that scuffing does occur at the primary wear scar, which is formed in the early stages of wear. It should be noted that we are studying the sample at the meso-scale, as we progress we look at the micro-scale and eventually at the nano-scale.

2.2. HPT Experimental Results and Analysis

In this section we look at the data output form the HPT. The data are plotted in the following order 0.25 x T, 0.5 x T, 0.75 x T and finally T (scuffing time based on the sudden increase in contact resistance and friction from the HPT). The actual experimentation time that led to scuffing was 6 minutes 15 seconds (it should be noted that prior experiments were done under similar conditions with similar samples, to confirm that the time T for scuffing is in fact correct in this case. This is important because all other following experiments are to be based on this time). A possible problem with the short duration of the tests is the fact that it might be too vigorous, however if the loading time was increased or rotation speed decreased the sample did not scuff within the time allowed by the refrigerant supply (the volume of refrigerant is constant thus the sample should scuff before the tests runs out of refrigerant). The experiments that were stopped prior to scuffing, were done so manually. Figures 2.14-2.17 show the HPT experiments for samples 2 to 5 respectively.

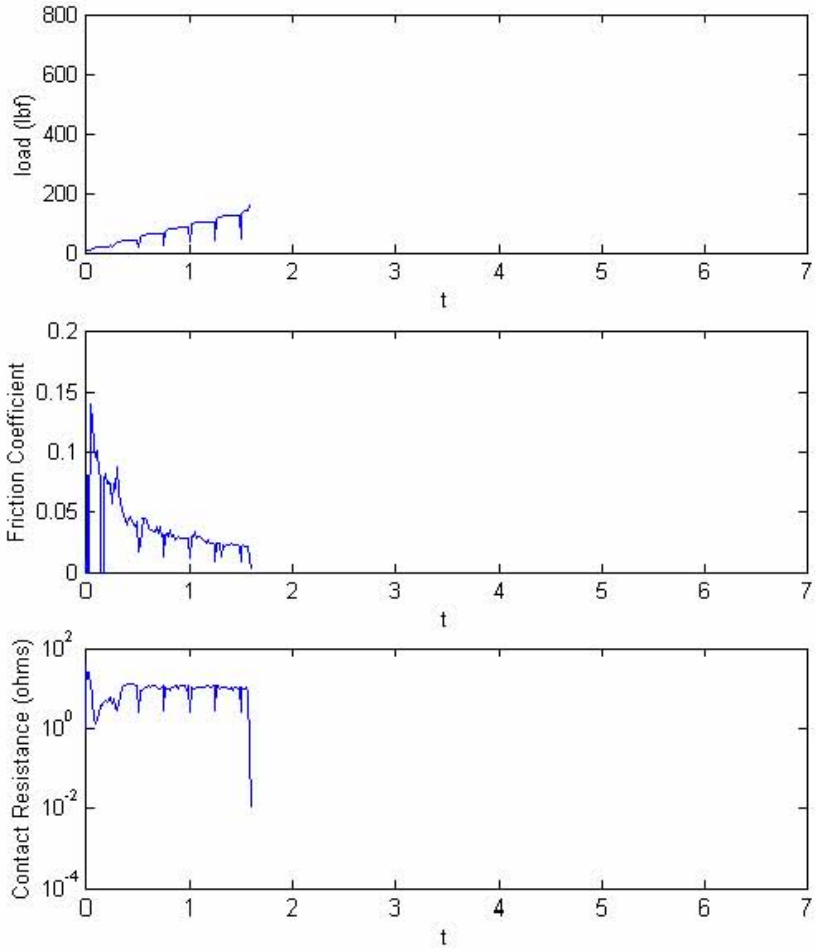

Figure 2.14, Sample 2, 0.25 x T scuffed sample.

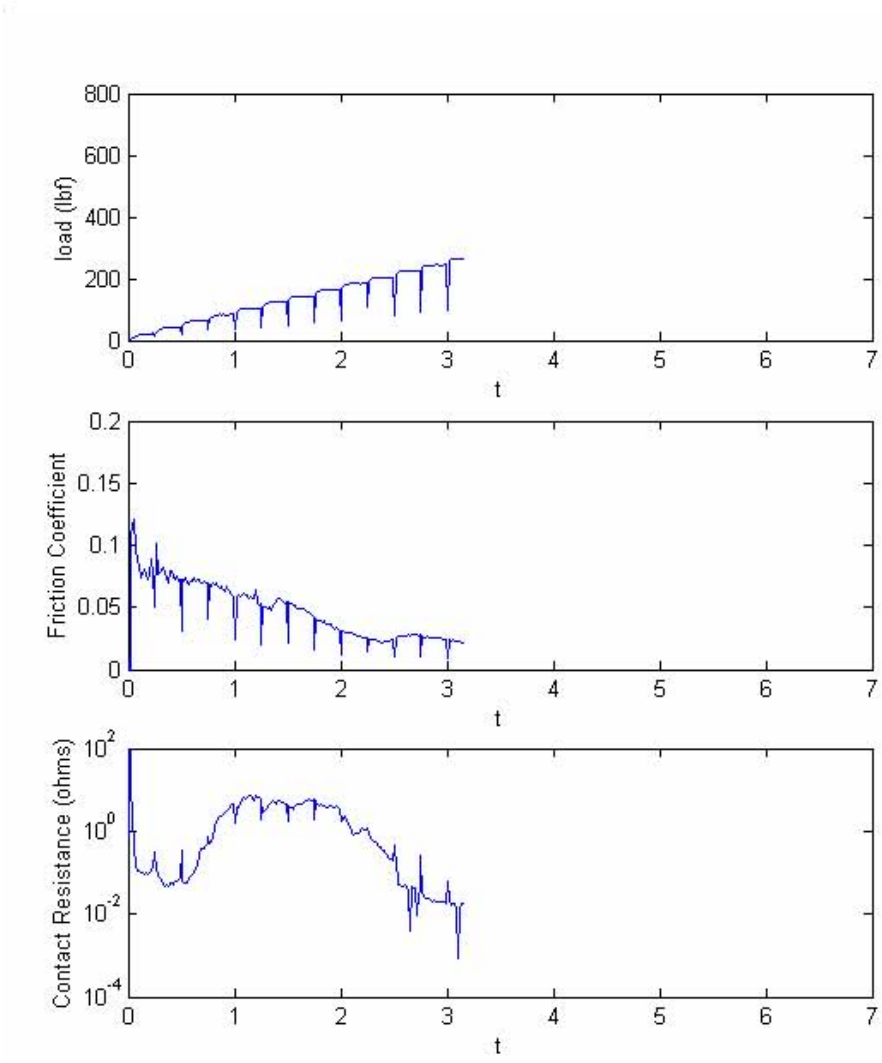

Figure 2.15, Sample 3, 0.5 x T scuffed sample.

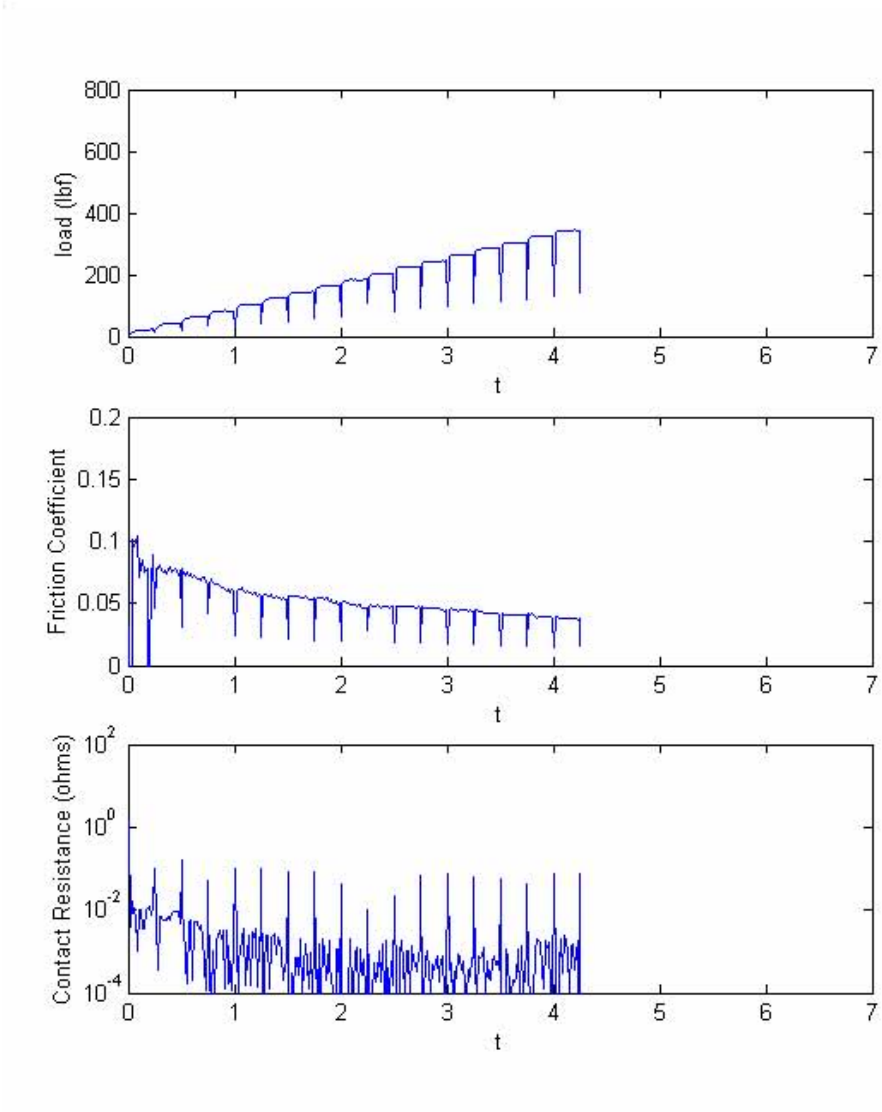

Figure 2.16, Sample 4, 0.75 x T scuffed sample.

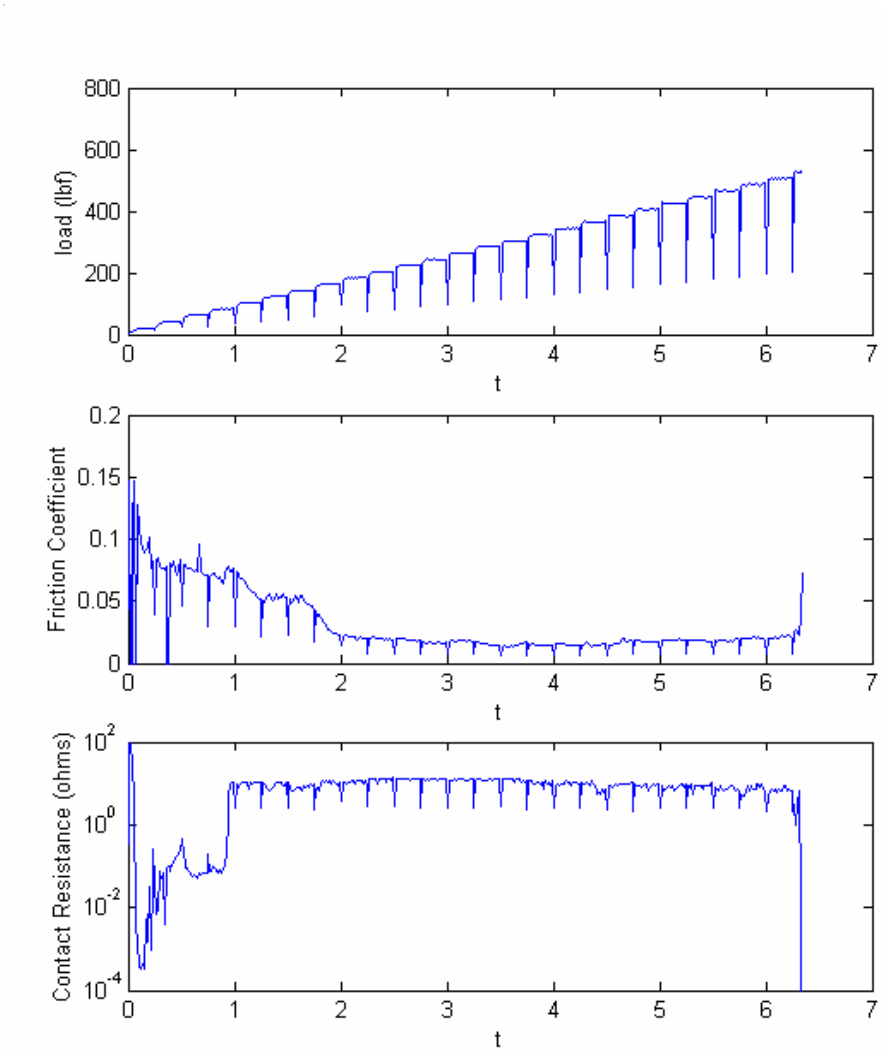

Figure 2.17, Sample 5, scuffed sample.

As depicted in Figure 2.17, the contact resistance drastically decreased at a time of 6.25 minutes, which was established as the scuffing time T. On the graphs above, there are 3 sections for each graph representing the normal step load, friction coefficient and contact resistance, respectively. The trends from these sub-plots with regard to figure 2.17 are explained below:

A. Load Vs Time:

The load applied to the pin on disc system is applied in steps as described earlier. These figures shows an increase in load every 15 seconds until the experiment is stopped. The vertical lines dropping down in the plot are electric noise and therefore should be ignored.

B. Friction Coefficient Vs Time

The friction coefficient is a representation of the physical resistance to motion experienced by the disc on shoe. Initially the friction coefficient is higher and erratic due to taller asperities with high. As these peaks are smoothened out the friction coefficient drops and stabilizes at an almost constant value (running in). In the case of

the scuffed experiment, the friction coefficient increases abruptly due to the fact that, as the asperities are smoothened out, the adhesion force between the disc and pin increases, the increase in adhesion force causes an increase in the friction coefficient. It is suggested that this case the scuffed sample failed due to adhesive failure.

C. Contact Resistance Vs Time.

The contact resistance represents the percent of asperity contact in the case of both asperity and lubricant presence within the interface. If the samples are fully separated, the contact resistance is infinite. On the other hand, if the asperities have significant contact, the contact resistance should be zero. If the contact resistance is in the range 10^{-2} to 10^{2} ohms, the lubrication regimes that exist are boundary and mixed. 10^{-2} means a lot of asperities contacting while 10^{2} means a lot less. In figure 2.14, a small area of contacting surface has been smoothened out thus the contact resistance drops, however the sample did not scuff at this point since the rest of the contact has not been affected. In the case of figure 2.17, initially there are several asperities in contact, as the asperities are smoothened out fewer remain in contact. As the asperities are worn out they reach a steady state stable boundary or mixed lubricant film is formed (constant contact resistance). As subsurface failure occurs, the protecting layers are destroyed, leading to scuffing (Yoon, 1999). The lubricant film is destroyed due to wear, and the surface smoothened out leading to a drop in contact resistance at the point of scuffing. It is also important to note that the pin and disc were stuck to each other at the end of the experiment resulting to a fairly low contact resistance.

2.2.1 Micrograph Analysis:

We now study the samples at the micro scale, where it seems the machining marks are more visible, thus showing that the surfaces are merely polished before they scuff.

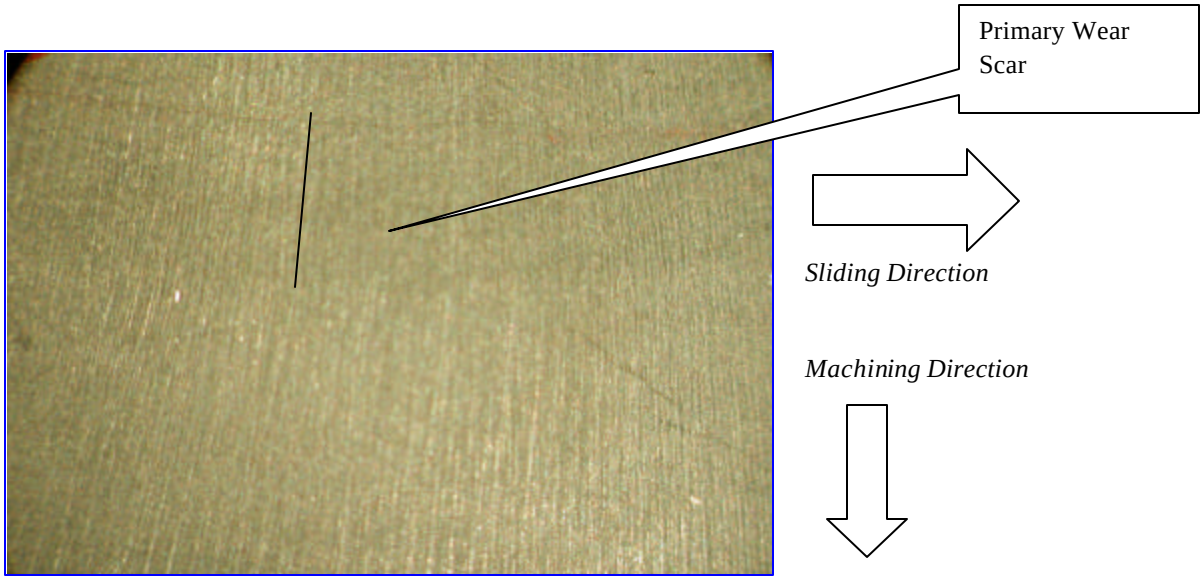

Figure 2.18, Schematic of wear part of sample subject to quarter scuffing time.

As can be seen from the sample above, there is very little visible damage done to the surface at this time. The surface seems a little polished, however, it is difficult to distinguish the zones.

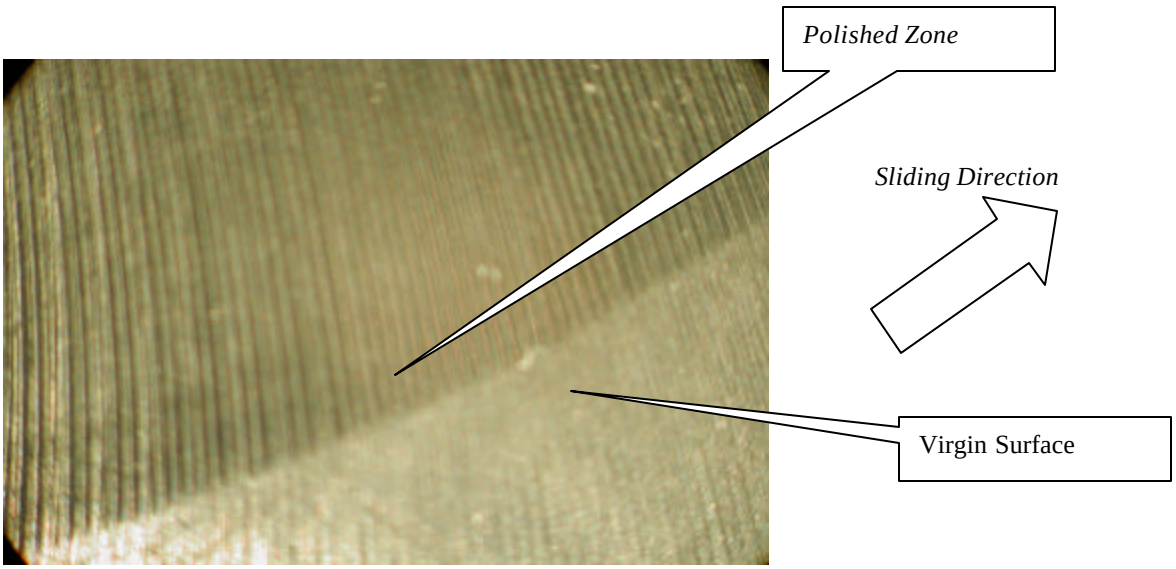

Figure 2.19, Schematic of wear track part of the sample subject to half scuffing time.

The figure above shows a clear difference between the original (bottom) and the polished (top) surfaces. However, it should also be noticed that, other than polishing no other intense damage is visible. At this stage the asperities on the aluminum surface have been smoothened out.

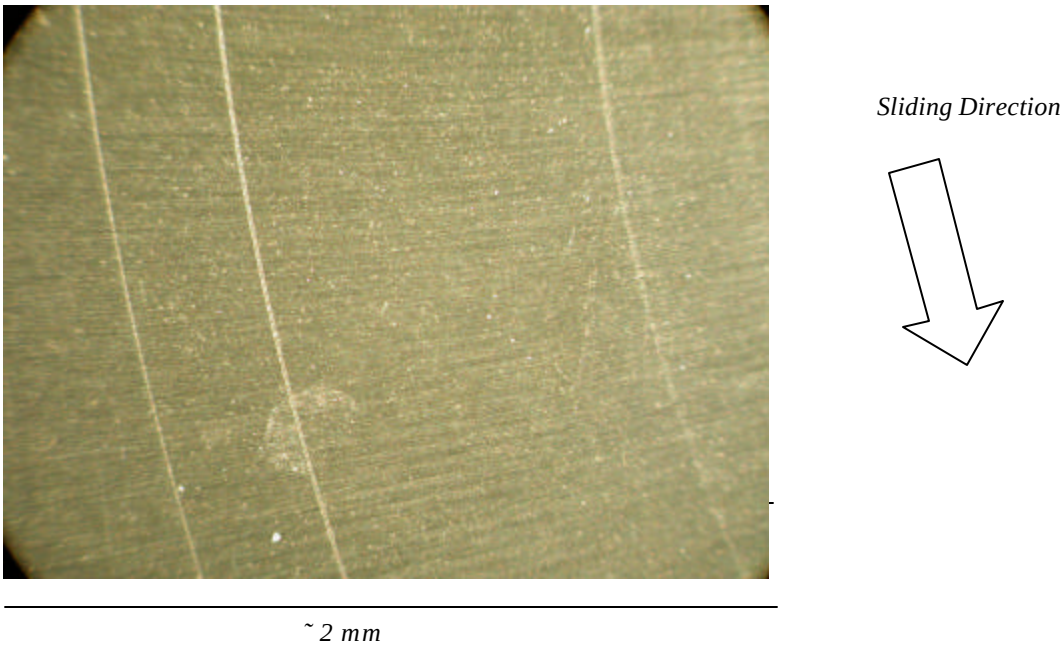

Figure 2.20, Schematic of wear track part of the sample subject to three quarter scuffing time.

As can be seen from the figure, other than surface polis hing, there exist distinct tracks, which are the foundations of scuffing. At is at this point, it is physically visible that the sample is about to fail.

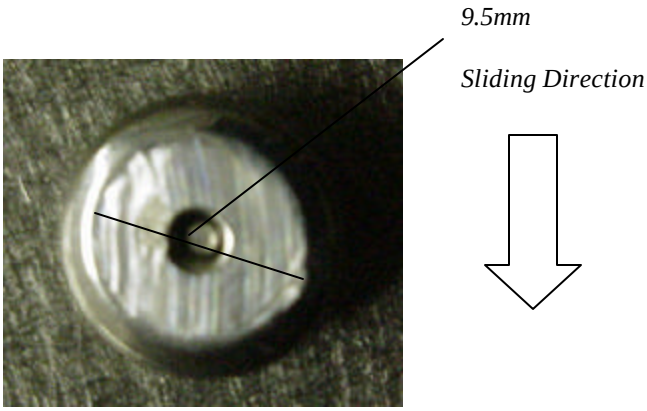

Figure 2.21, Schematic of wear track part of the pin subject to scuffing time.

In figure 2.21, a scuffed steel pin is shown, it can be seen from the image that sites of material transfer do exist (where aluminum has been transferred to the pin), and also material transfer from the pin has occurred (reason for this is explained in chapter 1 under wear).

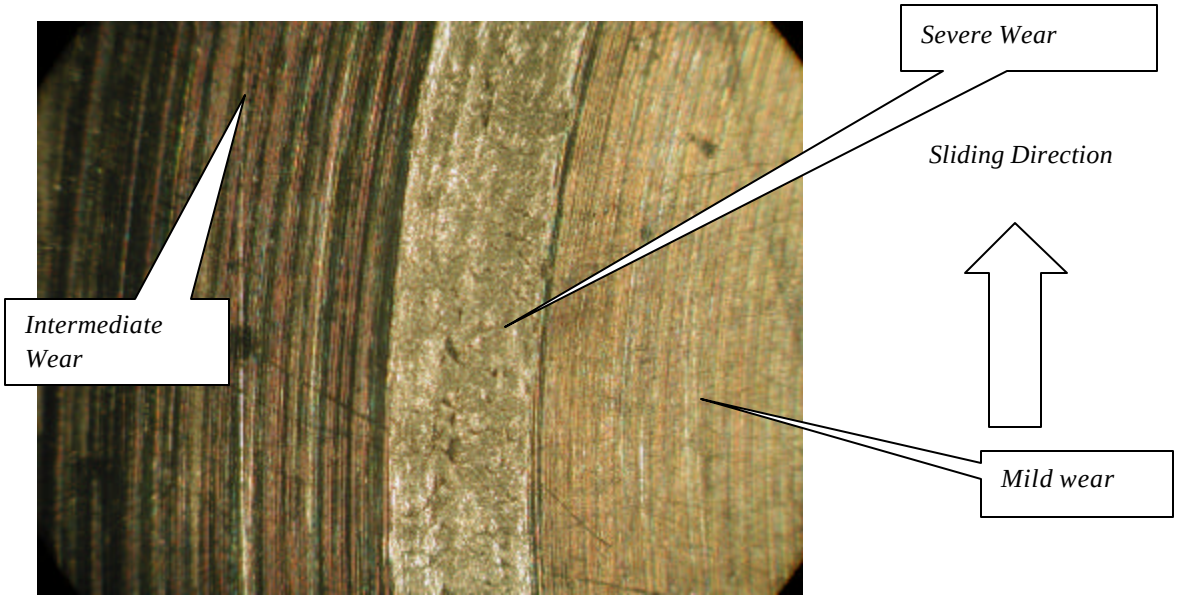

Figure 2.22, Schematic of wear track part of the sample subject to scuffing.

The image above exhibits the wear track and the region of material transfer (center track in the picture). Severe damage has occurred at the center of the picture, while the right-hand-side is polished very well. The left-hand side is subject to wear, however it is less intense than the other regions. The next figure exhibits the actual scuffed sample and its wear tracks.

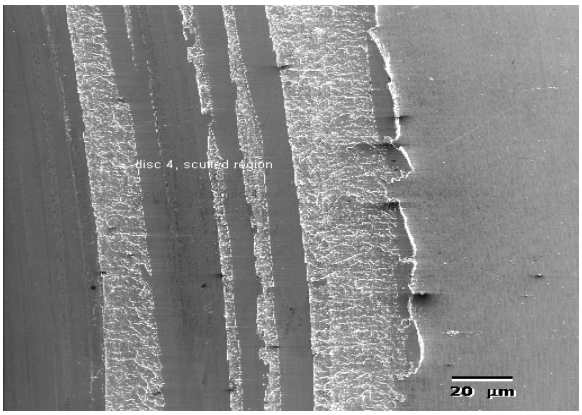

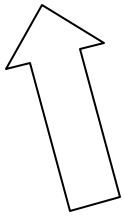

Sliding Direction

Figure 2.23, SEM image of scuffed primary wear scar

The SEM micrograph above shows that there is variation within the primary wear scar regarding material transfer. The primary wear scar formed is not even as shown by the photographs but is also composed of polished areas and material deposit sites. After the wear tests were conducted, other specific studies were carried out to investigate further the evolution of the surfaces. In Chapter 3, we study the evolution of surface parameters, while Chapter 4 looks at evolution of chemical composition of the surfaces and sub-surfaces. As it was discussed in Chapter 1, the emphasis of this study is on the surface evolution via surface topography changes; and on the nano-sub-surfaces. This is different then the approach followed by previous researchers, e.g., Yoon (1999) and Sheiretov (1997), where their focus was on much larger scales below the surface (few micrometers), and they did not systematically study the surface topography changes.

Chapter 3: Statistical Analysis

3.1 Introduction

One of the main objectives of this study is to investigate the trends that occur in surface parameters as the surface evolves from its virgin to worn states. Previous studies regarding compressor surfaces have mainly focused on the chemical composition of the surfaces and micrometer level sub-surfaces and related that to scuffing. In the 1950's a major development in the field of tribology was started which recognized and understood elasto-hydrodynamic lubrication (EHL) (Grubin, 1949). EHL became the focus of study and it was assumed that a system is in danger of scuffing when the thickness of the fluid film between the surfaces becomes less then the average height of asperities on the sliding surfaces (Dyson, 1976). To better understand the fundamentals of scuffing without external variable, scuffing under dry sliding conditions was studied by Sheiretov (1997), who proposed a process leading to subsurface failure, which eventually led to scuffing. Further studies carried by Yoon (1999) focusing on scuffing under starved lubrication conditions, suggested that scuffing was related to shear failure of the bulk material which was caused by formation of macroscopic adhesions at the sliding interface. Little work has been done suggesting the part played by surface parameters in scuffing of metals surfaces, in the present study we investigate at the progression of wear and respective change of surface parameters, and explore the effects of these changes on scuffing. Typical surface parameters that are used are (Ra, Rq, Skewness and kurtosis) can be extracted from surface roughness profiles by one of two ways. Either by using a contact profilometer, or by using an Atomic Force Microscope. The AFM is the preferred method to analyze a surface for it can carry out 3-D scans, which provide important information regarding the lay direction of the surface. The AFM is used for very smooth surfaces in MEMS and the Hard Drive Industry. The maximum scan length of the AFM is 100um, which is usually not sufficient for the rougher engineering surfaces like aluminum samples used in this study. Another major problem with the AFM is the difficulty with focusing on the sample surface due to the rough nature of the sample. With some luck some sample scans have been taken as shown below (Carried out by Alison Suh), these scans are very descriptive and provide information in both the radial and circumferential direction of the primary wear scar of the scuffed sample.

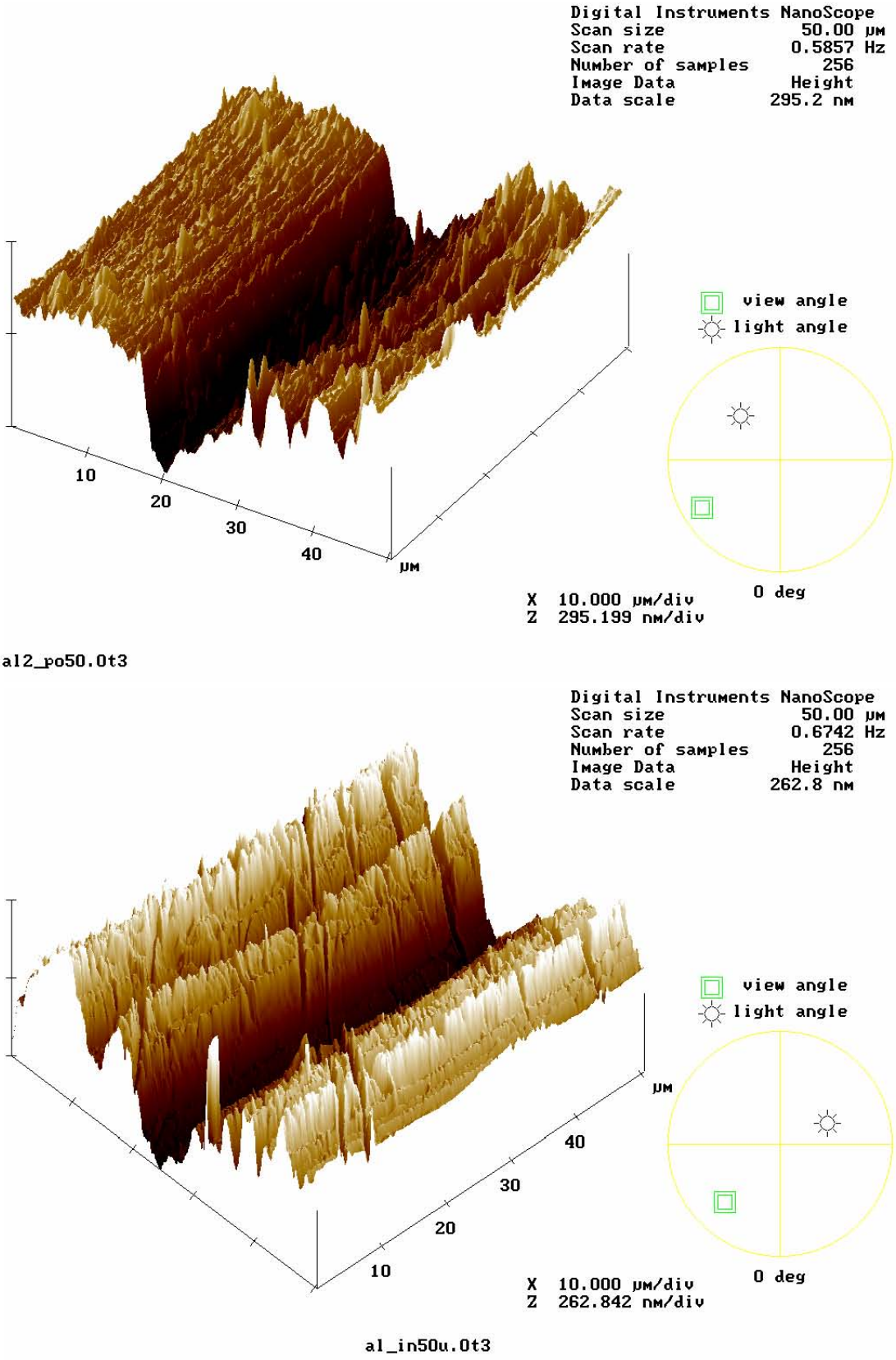

Figure 3.1 a and b, AFM scans taken on worn surface of Aluminum disc

For the two figures above the scan length was 50μm x 50μm and the scan was composed of 256 x 256 points. It can be observed that vital data can be collected by this instrument, which can be manipulated to obtain desired parameters for the study if the AFM can measure the sample surface.

However, due to the difficulties in using the AFM as described above, in this study, the data is mainly derived from data collected from the contact profilometer. To obtain information about the isotropy of the surface a study was carried out where line scans in two orthogonal directions with minimum and maximum spectral moments were taken as per McCool (1987). Then, the equivalent parameters and the isotropy index were derived. From this study, the average isotropy index for the virgin surface was calculated to be approximately 0.35, which implies that the surface is very anisotropic (an isotropic index of 1 means a fully isotropic surface). The data obtained from the contact profilometer was analyzed based on the Greenwood-Williamson (GW) (1966) model to extract the necessary parameters. The GW model of contacting rough surfaces assumes that when two nominally flat surfaces touch, contact occurs on the local high spots or asperity summits. Deformation occurs in the contacting region and could either be elastic, plastic or elastic-plastic depending on the contact pressure and material properties of the surfaces. All the summits are presumed to be spherical and have the same radius *R*, but the summit heights z are variable with a standard deviation *s*. The asperities are assumed to be uniformly distributed over the rough surface with a density of asperities *h*. The GW model also suggested, based on experimental results, that for many engineering surfaces the distribution of asperity heights tends to be Gaussian. Modifications to this theory were made by McCool(1986) and Chang(1986), however the foundation of the rough parameters was based on the existence of an isotropic surface where z(x) is the height distribution of the surface profile. From this, three spectral moments of the surface can be defined;

$m_o = AVG[z^2]$

$m_2 = AVG[(dz/dx)^2]$

$m_4 = AVG[(d^2z/dx^2)^2]$

From these spectral moments the three surface parameters are obtained as follows McCool (1987):

$\sigma = (m_o)^{1/2}$

$R = 0.375(\pi/m_4)^{1/2}$

$\eta = m_4/6\pi(3m_2)^{1/2}$

The Ra or *center line average* and the Rq (σ) or *root mean square* are the most widely used roughness parameters. For a surface where the height of the surface measured above a mean level, x is the coordinate on the surface, and L the measured length, the formula for obtaining Ra and Rq are given below.

$$R_a = \frac{1}{L}\int_0^L |z| dx$$

$$R_q = \sqrt{\frac{1}{L}\int_0^L z^2 dx}$$

The third parameter is used in this study, the Skewness parameter, which is a descriptor of the degree of asymmetry (it is also the third moment). A negative skewness value indicates the existence of more valleys (area) than peaks and vice versa for a positive skewness. Kurtosis is the fourth moment of the normalized distribution, and it has a value of 3 for a Gaussian distribution. Distributions with peaks sharper than Gaussian have values of kurtosis greater than this, and vice versa. The equations for these parameters are given below:

$$Sk = \frac{1}{s^3} \int_{-\infty}^{+\infty} z^3 f(z) dz$$

$$K = \frac{1}{s^4} \int_{-\infty}^{+\infty} z^4 f(z) dz$$

Where *Sk* is Skewness and *K* is Kurtosis.

The above equations are used to derive the parameters used for the analysis of data obtained from the contact profilometer. Below is a description of the contact profilometer, its capabilities, and the procedure used to carry out these experiments.

3.2. Dektak Profilometer

The Dektak^{3}st profilometer is an advanced surface texture measuring system, which accurately measures surface texture. The main principles behind the operation of this system are explained below. Measurements are made electromechanically by moving the sample beneath a diamond-tipped stylus (Figures 3.2 and 3.3). The high precision stage moves a sample beneath the stylus according to a user-programmed scan length, speed and stylus force. The stylus is mechanically coupled to the core of an LVDT (Linear Variable Differential Transformer). As the stage moves the sample, the stylus rides over the sample surface. Surface variations cause the stylus to be translated vertically. Electrical signals corresponding to the stylus movement are produced as the core position of the LVDT changes respectively. An analog signal proportional to the position change is produced by the LVDT, which in turn is conditioned and converted to a digital signal in the from of a single scan.

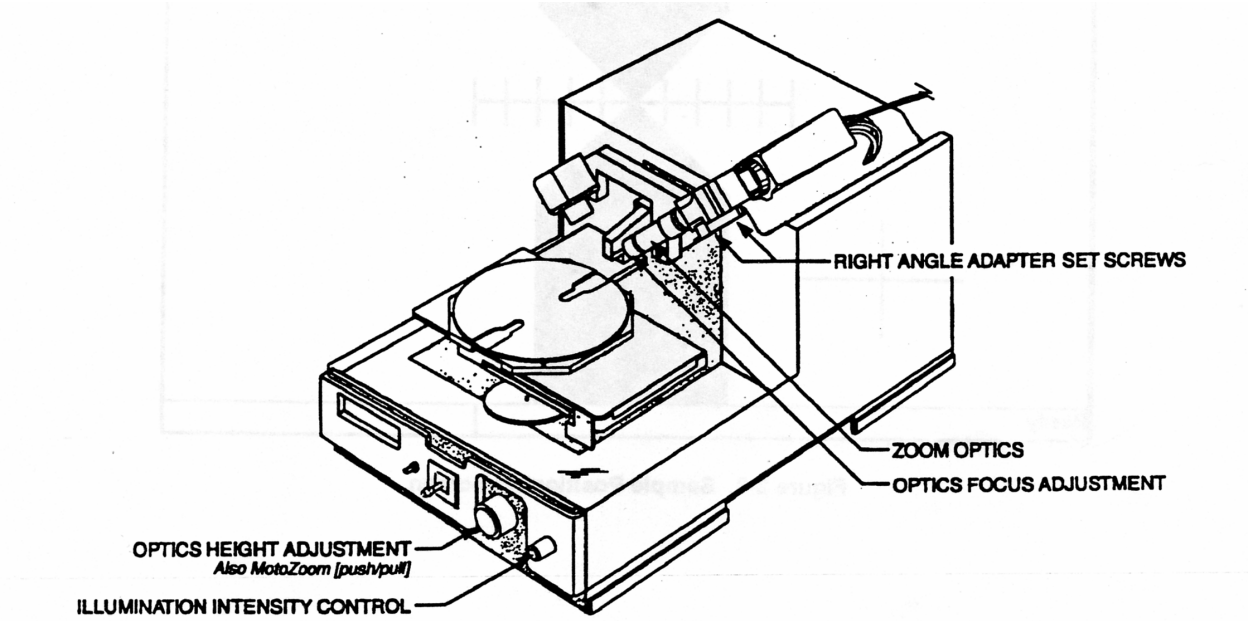

Figure 3.2, Schematic of Dektak Profilometer

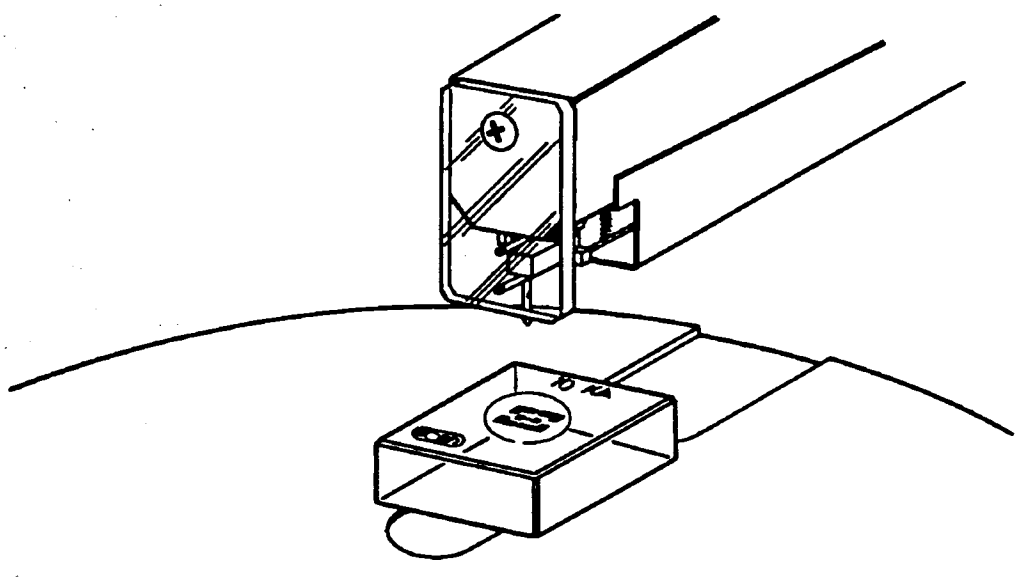

Figure 3.3, Schematic of cantilevered beam, tip and sample position on stage, of the Dektak Profilometer.

The Daktek is made up of several components; these components are listed and briefly explained below (Dektak Hand Book, 1991).

- Video Monitor: This displays programs and graphics in full color, along with a color video image of the substrate surface. It can also be used to view the sample either alone or with the graphics superimposed.

- Precision Scan Head: This unit contains the mechanical and optical components for sample placement, sample viewing, scanning/measurement and environmental protection. A 2.5-micron radius, diamond tipped stylus permits accurate measurements in a wide range of applications. Four optional styli with radii of sub-micron, 5 microns, 12.5 microns, and 25 microns are also available for applications, which require very high horizontal resolution or measurement of very soft films. The stylus can also be obtained in chisel–point shape. User programmable stylus force from 1 to 40mg allows profiling on soft or hard surfaces.
- Precision Sample Stage: A very high precision sample stage performs the scan and permits X-Y positioning to any location of measurement interest over a 76mmx152mm area with theta rotation up to 360 degrees (sample positioning is controlled manually).

There are some important points to note when selecting the stylus force for a scan. When using a low stylus force, the stylus may tend to lift off the surface if a large step is encountered at higher scan speeds. In applications where a light stylus force is required, it is recommended that low or medium scan speed be used at the shortest possible scan length. The horizontal resolution of the Dektak is determined by the scan length and scans speed. There are three speed ranges: Low, Medium and High. Low speed provides high horizontal resolution with 8,000 data points per scan and takes 50 seconds for the scan. Medium takes13 seconds and has 4,000 data points per scan at default setting. The default High takes 3 to 8 seconds and collects 2,000 data points per scan.

The horizontal resolution is directly related to the scan length and the number of data points per scan. The number of data points per scan can be adjusted either by altering the scan speed or by altering the scan length. The scan speed parameter controls the amount of time it takes to complete a scan and the scan resolution parameter displays the distance between data points.

When a scan is run, the stylus is lowered onto the sample surface, and the stage moves the sample as the stylus rides over the surface features. The video monitor allows the operator to view both the physical scanning of the sample and the plotting of the data simultaneously. At the end of the scan, the stylus automatically retracts and the system is immediately ready for the next scan. The surface features encountered by the stylus are represented as a two dimensional profile which is plotted, scaled, and displayed on the video monitor. Once a scan has been made, the initial profile may require software leveling, zero referencing (leveling the surface to predetermined zero plane) and software magnification to zoom-in on an area of interest. Measurement is a continuous process and is facilitated by simple movements of the Reference and Measurement cursors, which allow you to select specific regions of the scan for analysis. The plotting screen displays scan data as well as various parameters from the Scan Routine such as; the Scan ID#, scan length, scan speed, resolution, analytical functions, and stylus force. Also indicated are both the vertical and horizontal distances between the cursors as well as the distances from the vertical and horizontal "zero" grid lines.

Listed below are the technical specifications as provided by the manufacturer.

- Vertical Range: 100A to 1,310 KA
- Vertical Resolution: 1A/65KA, 10A/655KA, 20 A/1310KA (A= Angstroms),
- Scan Length Range: 50 microns to 50mm.
- Scan Speed Ranges: Low, Medium, High
- Scan Time Range: 3 seconds to 50 seconds
- Software Leveling: Two-point programmable or cursor leveling
- Stage Leveling: Manual
- Stylus (standard): Diamond, 2.5 micron radius
- Stylus Tracking Force: Programmable, 1-40mg
- Maximum Sample Thickness: 45mm
- Sample Stage Diameter: 165mm
- Sample Stage Translation: X Axis, ±76mm (from center) Y Axis, -76mm
- Maximum Sample Weight: 0.5Kg (1 lb)
- Power Requirements: 100/115/200Vac ±10%, 50-60Hz, 200Vac
- Warm-up Time: 15 minutes recommended for maximum stability
- Operating Temperature: 210 C ±3 0 C

3.2.1 Analytical Functions

The Dektak has a wide range of analytical functions available for analysis of roughness, waviness, step height, and geometrical measurements. These special functions allow the user to perform complex analytical computations on the profile data quickly and easily. Multiple analytical functions can be entered into a scan routine to automatically calculate surface texture parameters on like samples. The analytical functions are grouped and described below.

3.2.2 Roughness Parameters:

This is the first group of analytical functions that will be studied. When calculating roughness parameters, the R and M cursors are used to define the assessment area of the profile trace (these cursors provide the boundaries for the scan).

- Maximum Dev Maximum Deviation: Calculates the furthest data point above or below the mean line.
- Maximum Ra/ Maximum Ra: Identifies that portion of the assessment length, which has the highest Ra. The assessment length, defined by the cursors, is divided into nineteen overlapping segments. Each segment is equal to one-tenth of the assessment length distance. The Ra is calculated for each segment. The R cursor will be positioned in the center of the segment with the highest Ra. Only one Max Ra is allowed to be programmed into a scan program.
- Ra Arithmetic Average Roughness: This is the most used, international parameter of roughness. It is the arithmetic average deviation from the mean line.

- Rp Maximum Peak: The maximum height or the highest peak of the profile roughness above the mean line, within the assessment length.
- Rq Root-mean-square (RMS): Determines the root-mean-square value of roughness corresponding to Ra.
- Rt Maximum Peak to Valley: The sum total of the Maximum Peak and Maximum Valley measurements of roughness within the assessment length (Rt = Rp + Rv).
- Rv Maximum Valley: The lowest point, or the maximum depth of the profile roughness below the mean line, within the assessment length.

3.2.3 Geometry Parameters

- These parameters consist of:
- Area-Under-The-Curve: Computes the area of a profile between the R and M cursors with respect to the horizontal zero grid line. If the profile is above the zero line, area is expressed as a positive value, if below the zero line, the result will be a negative value.
- Perimeter: Calculates the outside perimeter of a profile between the R and M cursors. A horizontal reference line is created using the R and M cursor intercepts.
- Radius: A least-squares-arc is fitted to the data points and the radius is calculated from the equation of a circle. The algorithm does not distinguish between concave and convex shapes
- Slope: Calculates the arc tangent of the ratio of the vertical distance to the horizontal distance between the R and M cursor intercepts and is expressed in degrees.
- Volume: The integration-by-shells technique is used to find the volume of a solid. This is accomplished by rotating the lamina delineated by the scan trace and a line segment connecting the cursor intercepts through 180 degrees about a vertical axis, which is located half way between the cursors.

Although the profilometer offers various statistical parameters that can be studied, we concentrated on only the parameters, which are commonly used to study rough surfaces based on the GW model. The advantage of this is that we could concentrate more on these parameters and compare them to existing studies. The Dektak profilometer allows us to filter the scan data as per the application that is being studied. Three separate cut-off filters are provided for selecting the wavelength by pass frequency. The three filters are described below.

- Short (High) Pass Filter: This filter is used for calculating roughness data. It filters out low frequency waviness signals and allows high frequency roughness data to pass through.
- Long (Low) Pass Filters: This filter is used for calculating waviness data. It filters out high frequency roughness signals and allows low frequency waviness data to pass through.
- Band Pass Filter: When the band pass filter is selected, both the short pass and long pass filters will be enabled to calculate the roughness data. It creates a band, which filters out high frequencies above the band and low frequencies below the band.

3.2.4 Performing a Scan:

Once a sample has been selected, it is placed on the stage after the clean up process. The following is a summary of the procedure to be followed to obtain the profilometer and scan data.

1. A scan ID has to be entered into the computer for the specific scan.
2. The maximum scan length allowed is 50,000 microns (50mm). To set the scan length, click-on the "Length" parameter box enter the desired scan length and press the enter key. For our experiments the scan lengths for the short scans were 1000µm while the long scans were 12000µm.
3. The scan speed is directly related to the horizontal resolution and the number of data points per scan. Three default scan speed settings are available: Low speed (50 seconds), medium (12 seconds), and high speed (3 seconds) per scan. The speed selected in this case was low speed so as to get better quality data.
4. The data resolution parameter allows the horizontal resolution for the scan length and scan speed to be entered into the scan routine. The data resolution parameter provides three options: low, medium, and high. Adjusting the data resolution parameter adjusts the number of data points per scan and horizontal resolution (microns per sample) accordingly. High data resolution was used for the Aluminum samples.
5. The data point's parameter displays the number of data points per scan. The number of data points can only be adjusted by altering the data resolution or scan speed. In the case of the short scans, the combination of resolution and speed resulted to 8000 data points, while the long scans resulted to 4800 data points.
6. The scan resolution parameter is expressed in microns per sample. Therefore, the lower the number of microns per sample, the better the horizontal resolution. The "Horizontal Resolution" box in the scan parameters window displays the resolution (um/sample) for the scan length, speed, and data resolution of the current scan routine. Adjusting the scan length or speed or data resolution alters the horizontal resolution accordingly.
7. The available vertical resolution depends upon the measurement range selected. When measuring extremely fine geometries, the 65K (Kilo-Angstroms, 10 Angstroms = 1 nm) range provides a vertical bit resolution of 1A. For general applications, the 10A vertical resolution of the 655KA range is usually adequate. When measuring thick films or very rough or curved samples, the 1,310KA range with 20A resolution should be selected. Due to the roughness of the sample the 655KA range provided the best data for the sample, and hence was used.
8. Now you proceed to selecting the profile setting scales. Three different profiles are available for, a variety of sample surface characteristics: Valleys, Provides 90% of the measurement range below the zero horizontal grid line and is used primarily for measuring etched depths;

Hills and Valleys, provides 50% of the measurement range above the zero horizontal grid line and 50% below and is used in most applications, especially if the surface characteristics of the sample are not well known, or if the sample is out of level; Hills, provides 90% of the measurement range above the horizontal grid line. Used primarily for measuring step heights. In this study, Hills and Valleys (50%) profile was used because the sample was assumed to be composed of both, which is later validated in the skewness result.

9. The next stage is setting up the stylus force. The stylus force may be adjusted to compensate for various surface characteristics. When measuring soft material, a low stylus pressure should be used. When measuring hard samples with relatively large step heights, a high stylus force can be used to keep the stylus from lifting off the sample surface. A study was carried out to determine the appropriate stylus force, this study is summarized in Appendix 3.

10. Move on to the display parameter window and select the appropriate parameters, which are Ra, Rq, Skewness, Kurtosis and Radius of Asperities for this study.

11. The Dektak can be programmed to automatically software level the profile trace at the conclusion of a scan in relation to the cursor intercepts. In order to obtain accurate step height readings and analytical calculations, the trace must be software leveled. To enter software leveling, click on the box labeled "Automatic Leveling" in the display parameters window. When automatic leveling is selected, two additional boxes will be activated. These boxes permit the cursor bandwidths to be adjusted and entered into the software leveling parameter. If no bands are required, enter 0, and the default fine line cursors will be used to level the trace. If the desired cursor widths are known, they can be entered into the scan routine. The first box represents the width of the reference cursor and the second box is for setting the measurement cursor width. Also in this study, the scan was leveled in this case to eliminate the effect of the slope of the stage.

12. Next select the analytical parameters that need to be calculated from the scans. If need be, a filter should be turned on depending on the data being studied. The smoothing parameter permits a smoothing filter to be activated. When the smoothing function is used, raw, roughness and waviness profiles are calculated using the smoothed data, however, for our case the data was not smoothened or filtered.

13. Once this has been done the data can be saved and printed or exported as required.

3.3 Roughness Measurements:

As explained in the previous chapter, 5 samples were chosen for this study. These samples were ultrasonically cleaned, then marked in both the radial and circumferential directions as shown in Figure 3.4 (the marking was done to identify the surface where the virgin scan was carried out, so as to repeat a worn scan on the same spot). Limited study was done on the Steel shoe since it was one order of magnitude smoother than the Al disc

it was assumed to be generally smooth relative to the disc. The machining marks on the surface of the Aluminum disc were in the radial direction, therefore, the circumferential data are to be used for roughness analysis (the reason for this is if a scan is being taken parallel to the machining mark, it is difficult to say whether it is in the valley or peak of the machining mark, therefore the conclusion form such a study would not be valid). The aluminum disc was divided into 4 quadrants; 1, 2, 3 and 4. Each of these quadrants has scan position, radial short, radial long and circumferential short. The short scans are 1mm long and are primarily for roughness analysis. The long scan is primarily to study the depression or deformation formed at the wear track to measure wear. The data received from the Dektak was analyzed in MatLab, to calculate the various statistical parameters. The values received from both the Dektak and MatLab calculations were similar, thus verifying the validity of the calculations. The data were analyzed using MatLab because this program is more flexible than the one provided by the Dektak. The MatLab program is also easier to use to calculate various parameters, which can be manipulated here fairly easily. Another advantage of using the MatLab program over the Dektak data is the fact that the MatLab program can be edited and a section can be incorporated in the existing program to facilitate contact geometry calculations, which are the next step of the overall study.

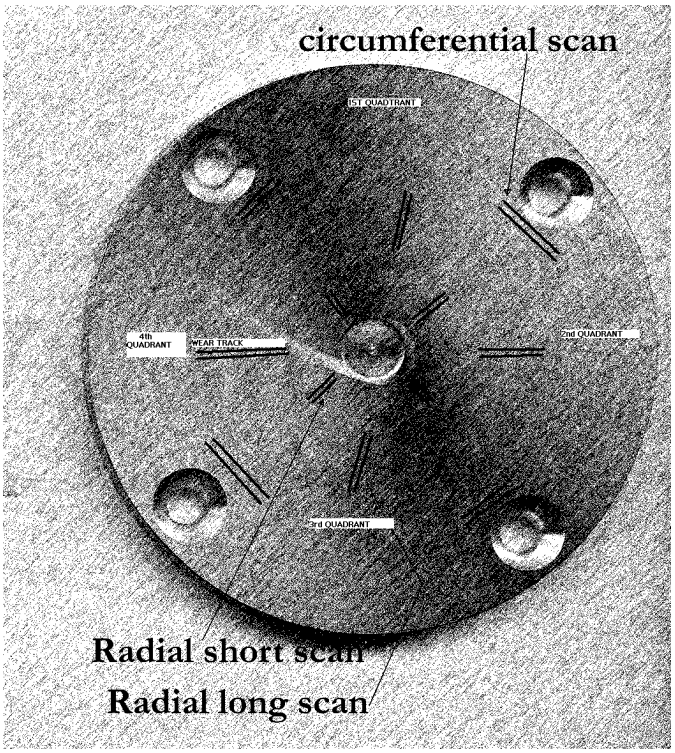

Figure 3.4, Description of surface scans on disc

It should be noted that the circumferential worn scans were not repeated on exactly the same location as the virgin scans, since any sort of marking on the wear path would have affected the results of the wear tests. We now begin out study go the profilometer scans beginning with the radial scans. As previously mentioned, we intend to move from a millimeter scale to the nano meter scale in our analysis. We look at the radial long scans which are 12000µm long, then radial short and finally the circumferential short scans.

3.4 Radial Direction Long Scan Data:

These are long scans made across the wear scan so as to see the cross-sectional damage done by the pin on the aluminum alloy disc. These scans are composed of 4800 data points and are 12000µm long. Below we briefly discuss these scans from their virgin to worn states.

Radial virgin long scan.

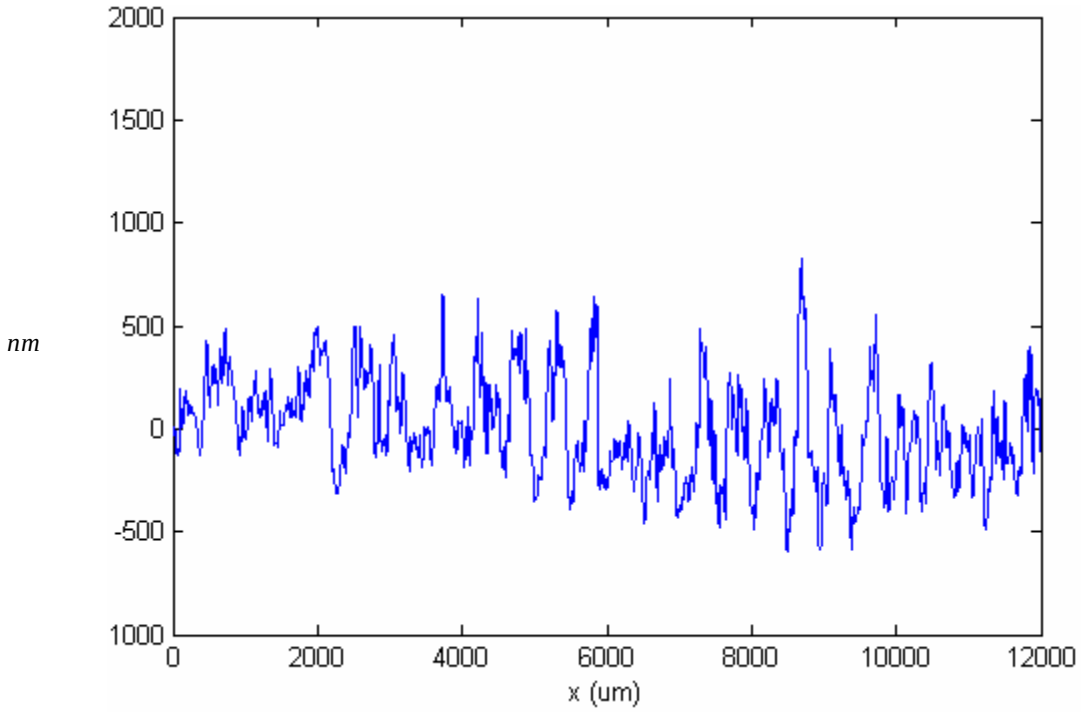

Figure 3.5, Radial long scan on virgin surface.

This scan is carried out on a virgin surface, which had undergone no testing. As can be seen from the graph the surface is fairly rough composed of both peaks and valleys. The first changes that occur from this surface can be viewed on sample 2 surface scan.

Radial quarter scuffed long scan:

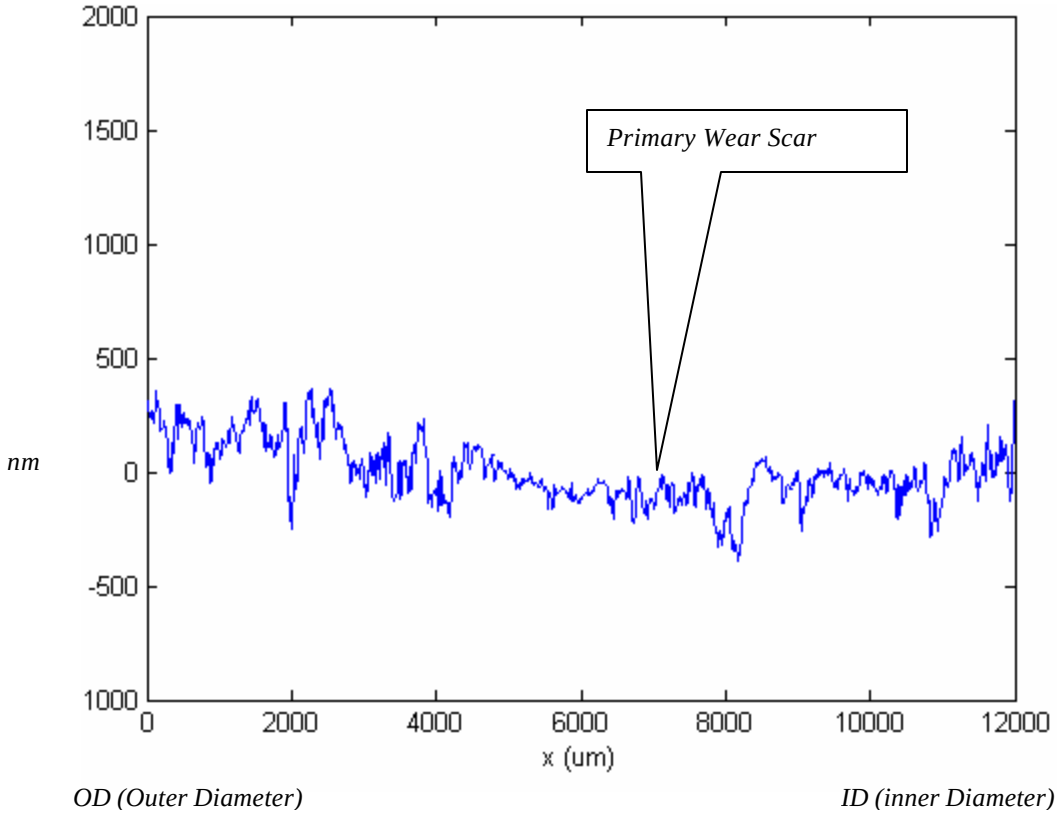

Figure 3.6, Radial long scan on quarter worn surface.

From the figure above it can be observed that the surface has had asperities polished. By polishing the asperity peaks the surface has been smoothened. The existence of wear track can be observed, however it is not obvious where it lies. From the figure above a primary wear track exists from 4000 µm to 8000µm on the x-axis, supporting the observation that there exists a dominant wear scar that eventually will contribute to scuffing (Figure 2.10). This is the same trend observed in the circumferential scans. We now subject the surface to more wear to see the change in topography.

Radial half scuffed long scan:

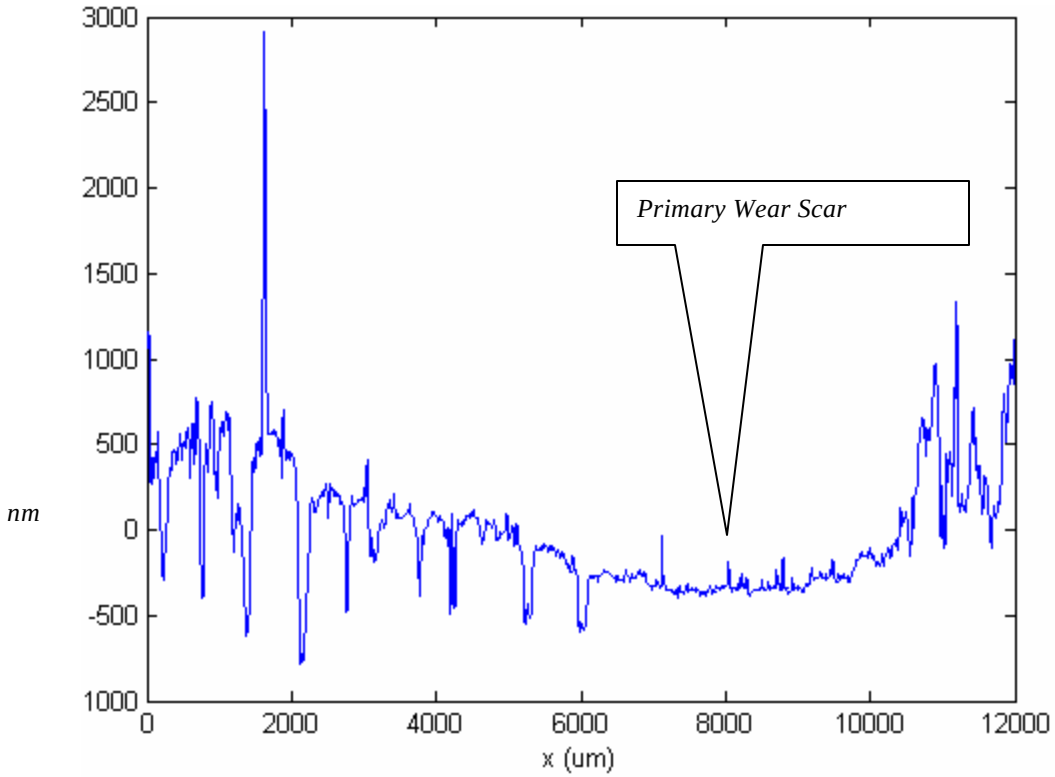

Figure 3.7, Radial long scan on half worn surface.

This scan shows that the asperities in the previous scan have been roughened, thus supporting the hypothesis of cyclic roughening. The wear track position can be established fairly easily from the above graph, some material displacement can also be noticed. The same trend as before is observed here, there is a primary wear scar that exists as shown. From the figure it is visible that the surface is undergoing drastic changes, which will lead to plastic deformation.

Radial Three quarter scuffed long scan:

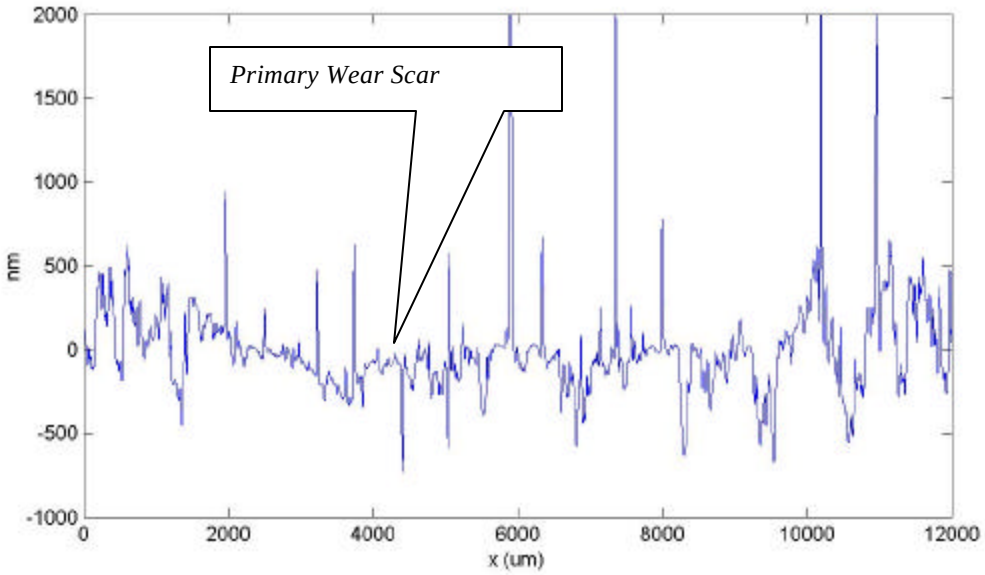

Figure 3.8, Radial long scan on three quarter worn surface.

As the surface is worn, the asperities are smoothened as depicted in the figure 3.22 above. This figure provides further support to the theory that the surface is progressively worn out, whereby it is initially smoothened, and keeps on being smoothened till scuffing occurs. We now look at the last graph and that is the scuffed scan.

Radial scuffed long scan:

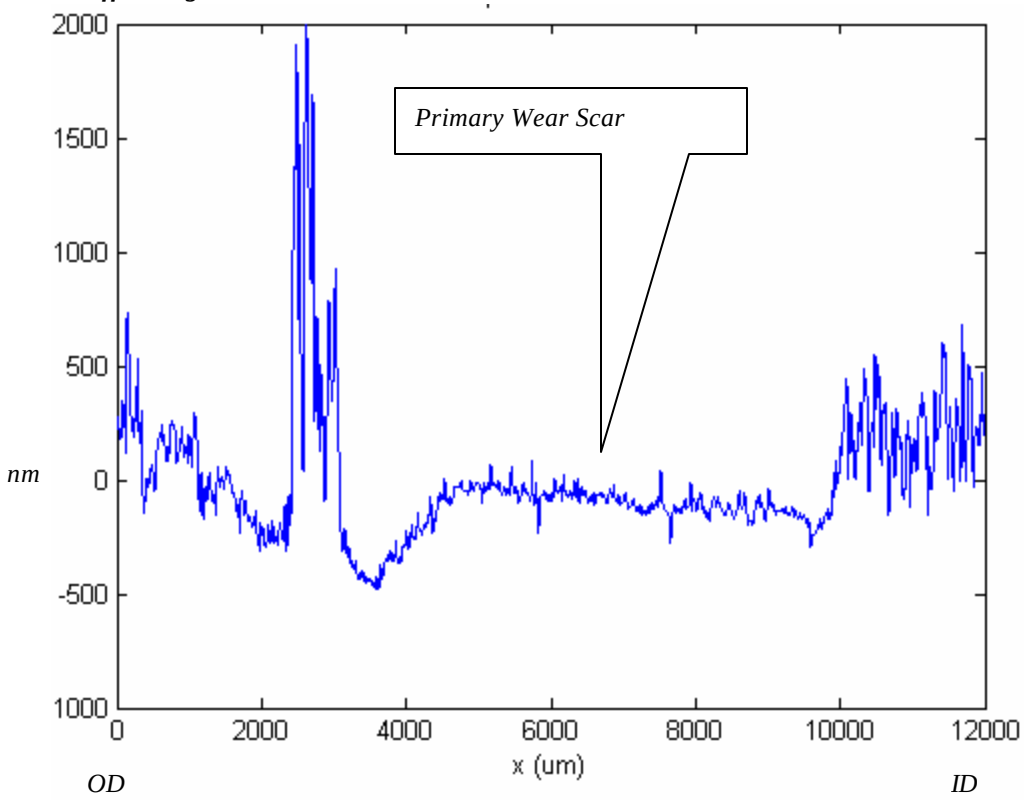

Figure 3.9, Radial long scan on scuffed surface.

Material transfer occurs when a surface is scuffed, this is displayed by the figure 3.23. There is displacement of material at about 3000um on the x-axis, where there is a mountain of material from the surrounding areas. A deep valley has also been created at 3500um. On the far end at 10000um to 12000um there is another sight of material deposition. The surface between the two areas of material transfer is a smooth surface possessing an Ra value of about 0.0338µm.

3.4.1 Radial Direction Short Scan Data:

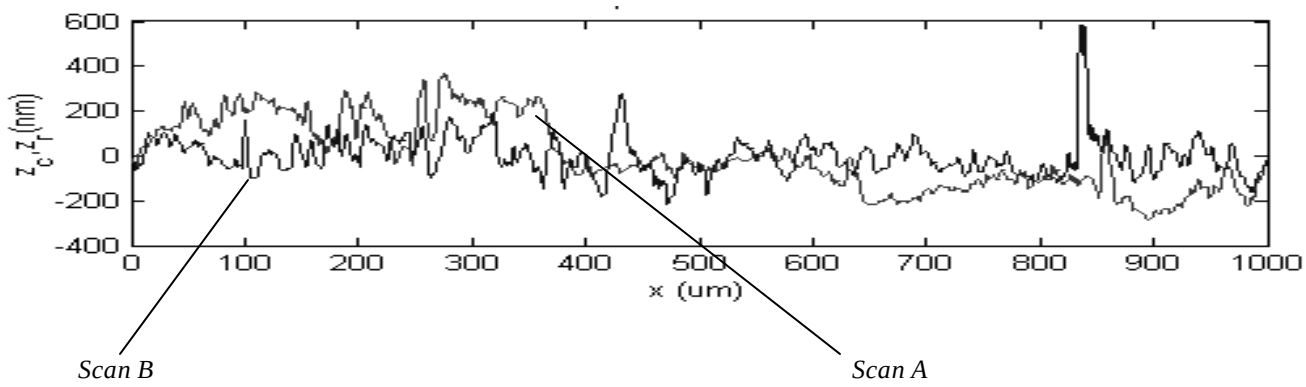

Figure 3.10, Variation of radial scans due to machining process

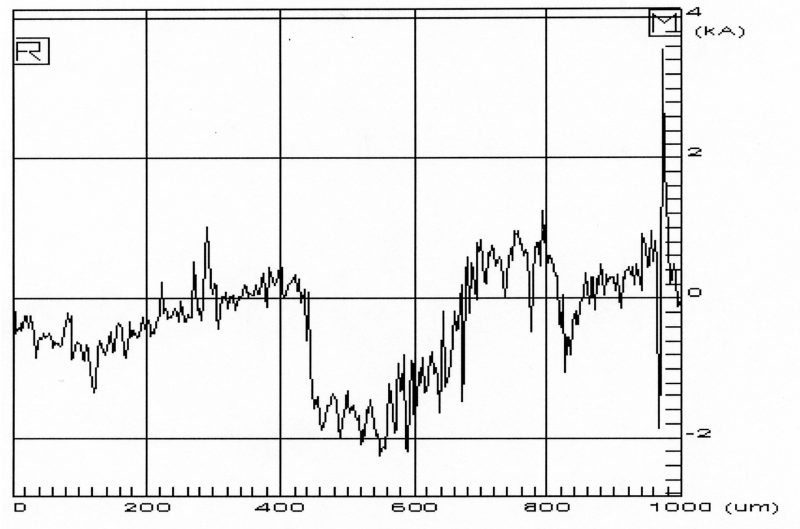

Figure 3.11, Radial short scan

Figure 3.10 above shows two different radial scans on a virgin disc, it can be observed that scan A goes over a peak than into a smaller valley and back on a peak, while the scan B travels constantly on a peak or in a valley. The first scan had Ra and Rq values of 0.132 µm, 0.156 µm respectively, while the second one had Ra and Rq values of 0.00627µm, 0.00829µm. Figure 3.11 shows another Daktek scan, which illustrates the profilometer traveling over a peak into valley then onto a peak once again. The two figures clearly illustrate the fact that it is very difficult to obtain data in the radial direction, which can be used for analysis. Due to the unreliability of this data type, it was decided not to use the data. The isotropy index was calculated as mentioned earlier, and had a value of 0.35 confirming that the surface is very anisotropic. We now progress to studying the circumferential profilometer data.

3.5 Analysis of Circumferential Profilometer Data:

As mentioned earlier, the data obtained in this direction will be studied most intensely for any noticeable trends. In this section we look at representative Daktek scans of each sample in the circumferential direction, then we proceed to plotting the appropriate graphs and deducing conclusions form this data. The profilometer scans provide us with a visual representation of the actual surface. Below we look at the change in surface shape as it gets worn out.

Virgin surface:

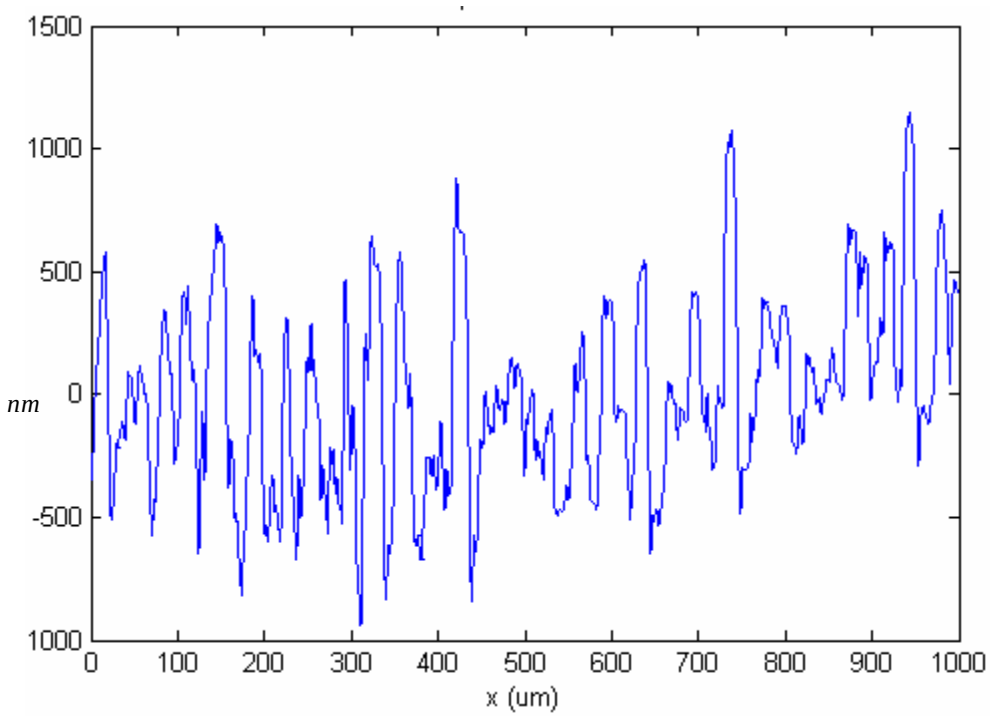

Figure 3.12, Profilometer scan of virgin sample, sample 1

The profilometer scan above is of a virgin surface in the circumferential direction. The scan is composed of 8000 data points (all scans in the circumferential direction have the same number of data points), and is 1mm long. As can be seen the virgin surface is composed of both peaks and valleys, however the peaks are dominating thus it has a positive skewness of 0.409. The Ra and Rq are 0.297 ± 0.035 μm and 0.363 ± 0.04 μm respectively. This graph represents all the virgin scans fairly well, since it posses parameters which are close to the average of the data set, however, the roughness parameters for all the scans were extracted and are depicted in Table 3.1, as will be discussed later. We now subject the above surface to wear and look at it after 0.25xT scuffing.

Quarter Worn Surface:

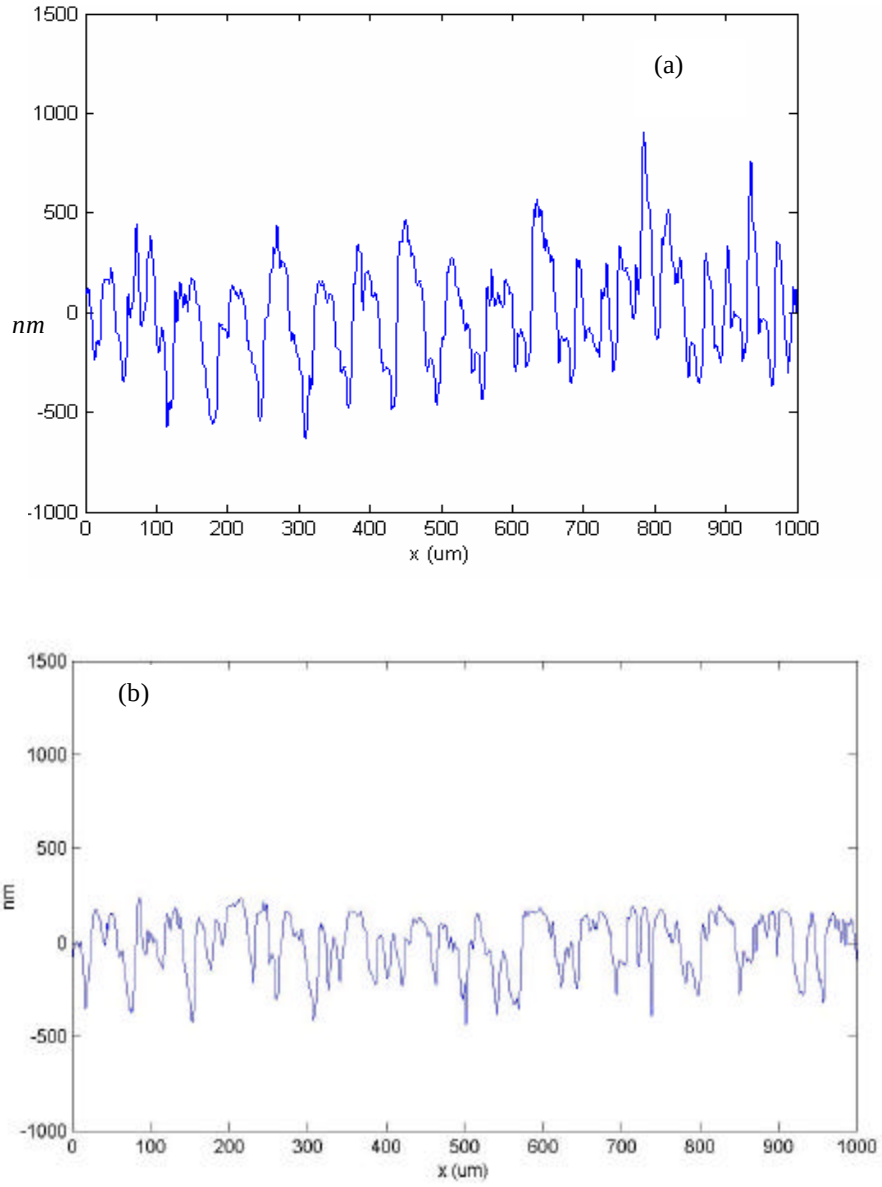

Figure 3.13, Profilometer scan of Sample 2: (a) virgin and (b) worn surface

The above shows a surface at its virgin state and worn state that under went wear for a quarter the time needed to scuff it. The surface has been smoothened rigorously. The asperity peaks have been polished and the surface is mainly composed of valleys, which gives it a negative skewness of –0.67 (table 3.2, sample 2:1:C). The Ra and Rq values are 0.12 µm and 0.16 µm respectively. From the above graph we can observe that polishing or smoothening has occurred in the first quarter of the time needed to wear the surface out. All the data collected on this sample reflect this conclusion, thus reinforcing the observations made here. However from the optical images (Figure 2.10) the surface does not seem to be damaged much accept for a specific primary scar within the wear

track. The primary scar posses much lower values of Ra (0.08 µm) and Rq (0.11µm) and has a skewness of about – 1.57. This is a significant point because it shows that there is a change in the surface properties of the al disc, the question now arises whether the surface will become smoother or rougher if it were worn to 0.5xT scuffing?

Half Worn Surface:

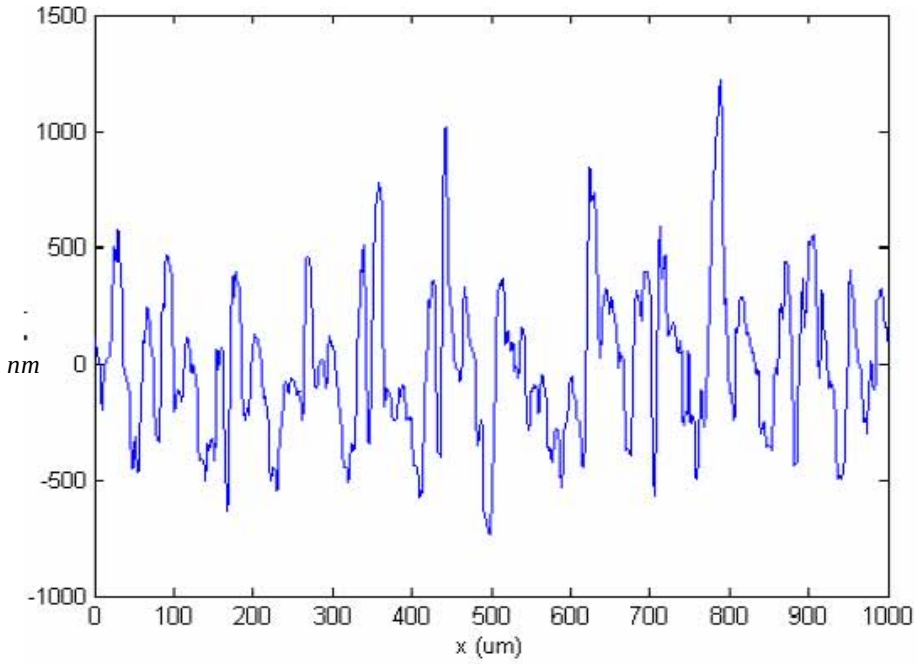

Virgin surface scan of sample

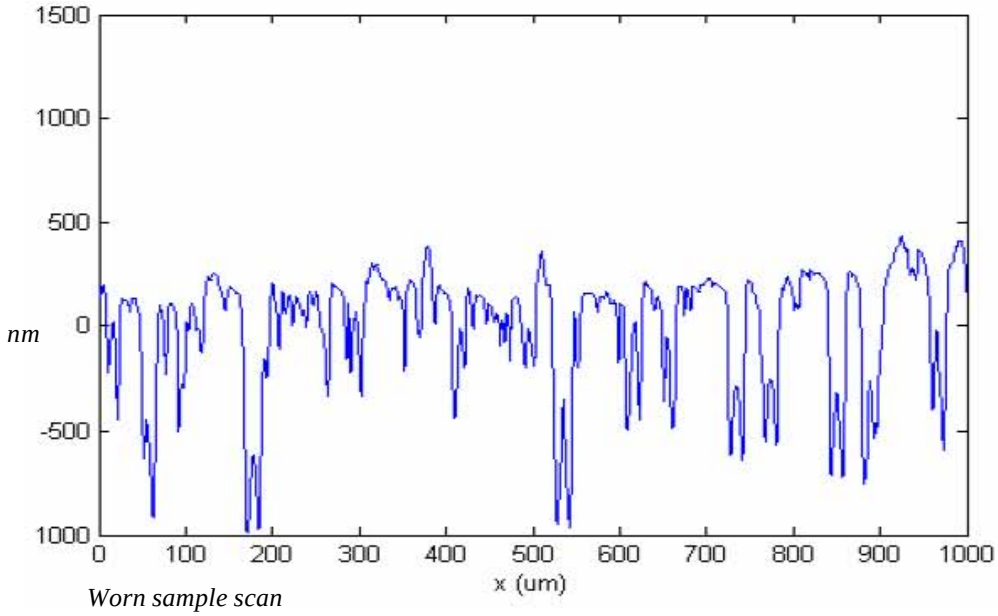

Worn sample scan

Figure 3.14, Profilometer scan of half worn surface

The half worn surface displays some interesting changes from the previous surface. The first is that the surface becomes slightly smoother than the virgin surface as shown by the figures above, and possesses Ra and Rq values of 0.223 µm and 0.285 µm, respectively. This could have been caused by the fact that the virgin disc used for this test was slightly rougher than that used for the quarter time to scuffing test. Further smoothening of the surface contributes to a skewness of –1.356, which is the lowest so far. An important observation is that the surface possesses a more prominent (Figure 2.11) wear track than the quarter scuffed, however the primary wear track seen in the previous sample does still show up. To observe further trends we have to look at the 0.75xT scuffing.

Three-Quarter Scuffed:

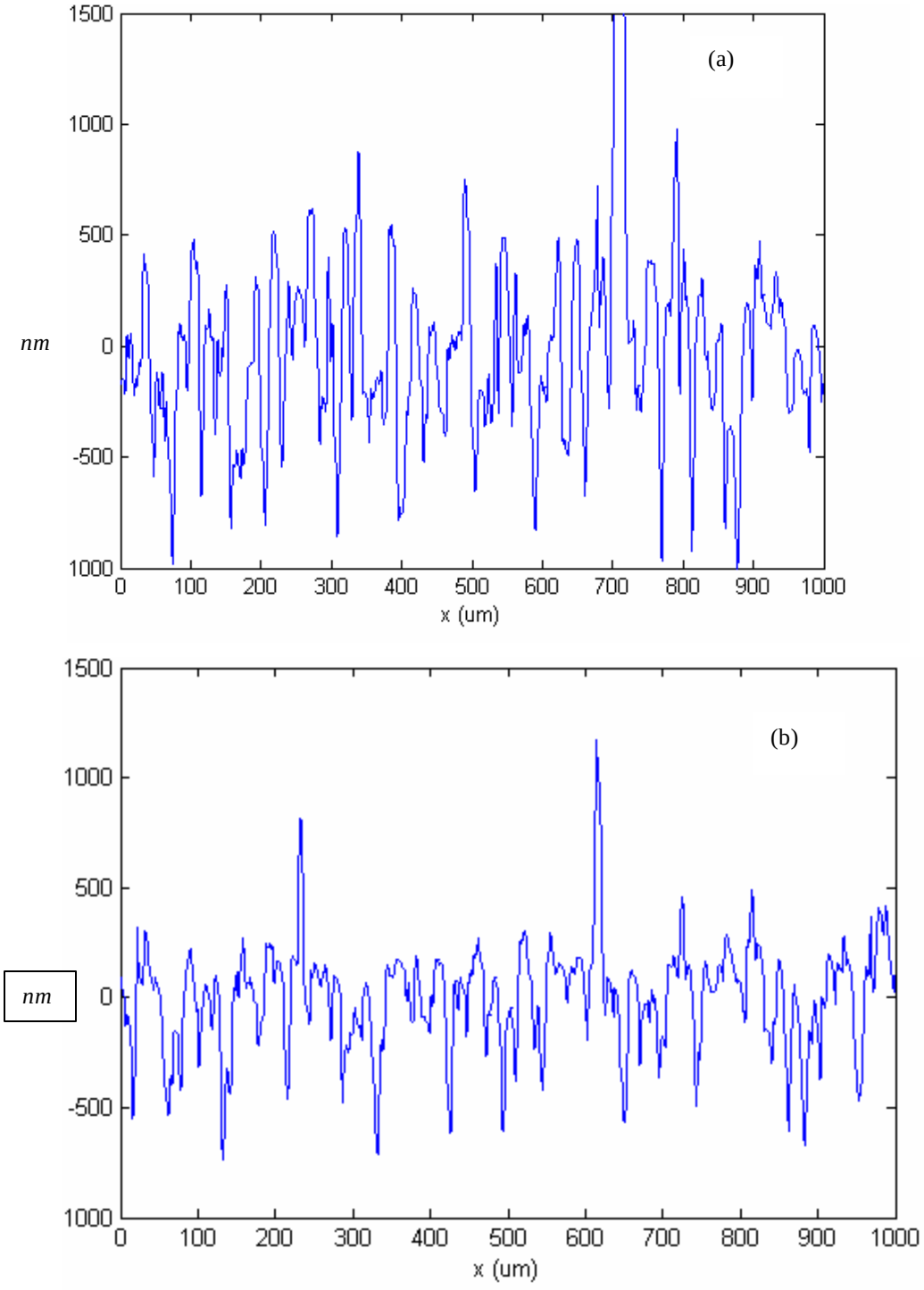

Figure 3.15, Profilometer scan of three quarter worn surface: (a) virgin, (b) worn surface

At 0.75xT scuffed, the surface smoothens out form its rougher state at 0.5xT scuffed. The new surface has Ra and Rq of 0.176 μm and 0.234 μm respectively. The number of peaks in this case increase due to wear thus the

skewness moves to an almost zero, having a value of -0.021. As the broken asperity peaks are subject to wear from the smoother pin surface, they are actually broken into smaller peaks and valleys, which allows for a recovery in the skewness parameter. This sample shows a more distributed wear track which is more dominant that the previous ones, however it still maintains the primary wear track which is now showing signs of scuffing at the edges. So far, as expected the data reveal progressive surface wear. In the scuffed scan, there is material transfer thus it cannot reveal what truly happens to the virgin surface.

Scuffed Surface:

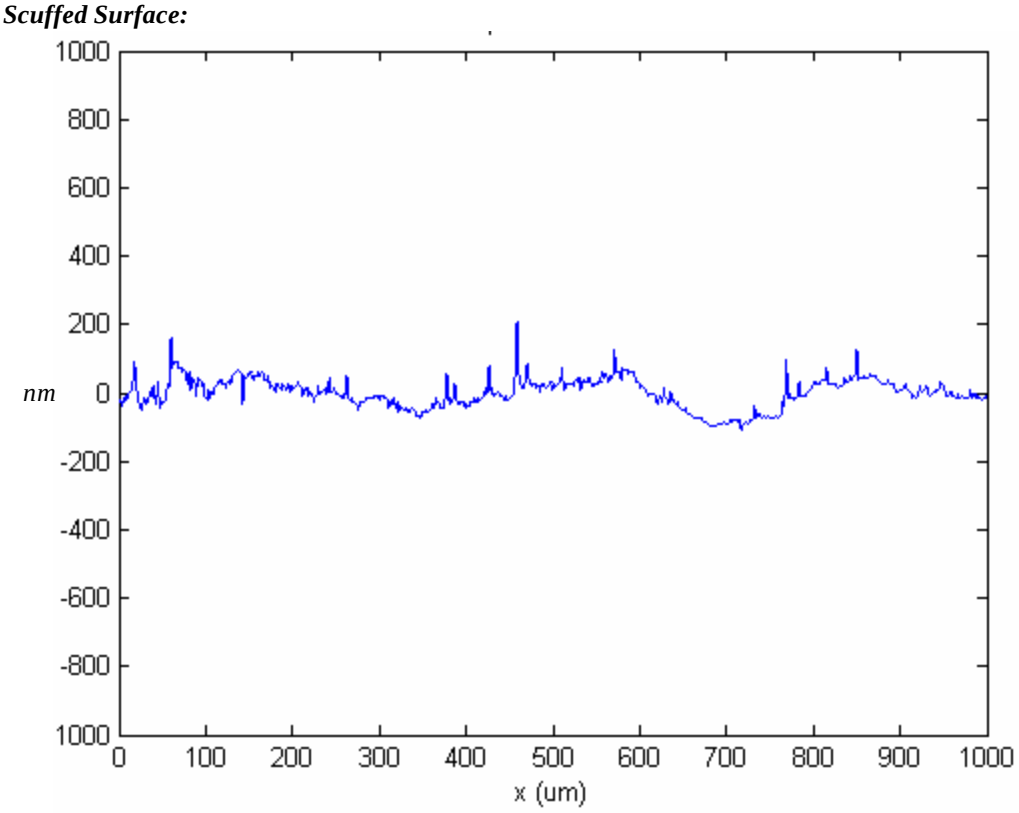

Figure 3.16, Profilometer scan of scuffed surface

The scuffed surface is smoothened to its smoothest state possessing Ra and Rq values of 0.0339 µm and 0.0425 µm. This shows that the surface is actually polished thus giving it a glossy look that was described in the previous chapter. The skewness of the surface is 0.039, indicating a recovery from the negative skewness that the previous stages had. The graphs presented above represent single scan lengths. For further analysis, the relevant data are plotted for the 5 discs and the individual parameters analyzed. Below we study the changes in surface parameters from one disc to the other.

3.5.1 Data Analysis

The various data obtained from the profilometer was analyzed and the summary is tabulated below. In the table under the disc number, the first number is the disc number, the second stands for quadrant on the disc and the letter stands for the direction.

Examples:

1_1_C ; disc 1, quadrant 1, circumferential scan

2_3_R; disc 2, quadrant 3, Radial

4_4_L; disc 4, quadrant 4, Long scan in Radial direction.

Below is the list of wear subject to each sample:

- Sample 1; Virgin sample, no wear test.
- Sample 2; Sample was worn in for a time corresponding to 0.25x T
- Sample 3; Sample was worn in for a time corresponding to 0.5x T
- Sample 4; Sample was worn in for a time corresponding to 0.75x T.
- Sample 5; Sample was run till it scuffed, time taken to scuff (T) noted.

Table 3.1, Statistical parameters of five discs at their virgin state.

Disc Number	**Ra**	**Rq**	**Radius of Curvature Asperities**	**Areal Density of Asperities**	**Roughness Parameter**	**Skewness**	**Kurtosis**	**Plasticity Index**
	μm	**μm**	**μm**	**μm^{-2}**				
	CLA	RMS	R	η	β	Sk	K	Ψ
1:1:C	0.3051	0.3832	7.7700	0.0256	0.0763	0.3730	2.8800	2.5400
1:2:C	0.3320	0.4080	6.9500	0.0249	0.0706	-0.0191	2.5500	2.7500
1:3:C	0.2990	0.3790	7.5700	0.0224	0.0883	0.2760	3.2700	2.6700
1:4:C	0.2260	0.2910	8.0800	0.0249	0.0587	0.6790	3.4900	1.8400
1:1:R	0.1350	0.1650	20.6000	0.0453	0.1540	0.3540	2.4400	2.1400
1:2:R	0.2120	0.2590	11.3000	0.0596	0.1750	0.4260	2.3800	2.7500
1:3:R	0.1380	0.1760	15.1000	0.0469	0.1250	0.3200	3.1900	2.6700
1:4:R	0.1190	0.1580	22.8000	0.0424	0.1530	0.1310	2.9200	1.8400
1:1:L	0.1780	0.2290	373.0000	0.0009	0.0791	0.3970	3.6300	0.3560
1:2:L	0.2020	0.2580	380.0000	0.0008	0.0742	0.4470	4.9000	0.3560
1:3:L	0.1820	0.2360	349.0000	0.0009	0.0726	0.5190	3.9400	0.3580
1:4:L	0.1850	0.2430	383.0000	0.0007	0.0655	0.0476	5.8100	0.3580
2:1:C	0.2250	0.2830	9.9600	0.0249	0.0700	1.2900	3.3000	1.5800
2:2:C	0.2270	0.2770	9.8000	0.0272	0.0738	0.0765	2.6300	1.6700
2:3:C	0.2060	0.2540	12.5000	0.0269	0.0854	0.1700	3.0000	1.5500
2:4:C	0.2500	0.3150	8.8800	0.0287	0.0709	0.1910	2.9800	1.7300
2:1:R	0.1320	0.1560	32.0000	0.0462	0.2300	0.3800	2.0400	1.5800
2:2:R	0.0629	0.0858	21.3000	0.0460	0.0839	1.7100	11.6000	1.6700
2:3:R	0.1190	0.1430	22.8000	0.0591	0.1930	0.5480	2.4100	1.5500
2:4:R	0.1640	0.1970	20.3000	0.0571	0.0863	-0.0955	3.8100	1.7300
2:1:L	0.1080	0.1440	634.0000	0.0007	0.0703	0.5720	3.4200	0.3120

Disc Number	**Ra**	**Rq**	**Radius of Curvature Asperities**	**Areal Density of Asperities**	**Roughness Parameter**	**Skewness**	**Kurtosis**	**Plasticity Index**
	mm	**mm**	**mm**	**μm^{-2}**				
	CLA	RMS	R	η	β	Sk	K	Ψ
2:2:L	0.1390	0.1760	470.0000	0.0007	0.0518	1.4300	24.0000	0.3120
2:3:L	0.1380	0.1830	470.0000	0.0006	0.0597	0.9580	3.0400	0.2870
2:4:L	0.1410	0.1720	480.0000	0.0006	0.0590	0.2510	2.9400	0.2870
3:1:C	0.2600	0.3320	7.8000	0.0306	0.0793	0.8050	4.1100	2.0400
3:2:C	0.2560	0.3350	9.2300	0.0286	0.0883	0.8880	4.5600	1.9100
3:3:C	0.2530	0.3200	9.1000	0.0260	0.0755	0.5850	3.5700	1.9000
3:4:C	0.3270	0.4220	7.5500	0.0280	0.0892	0.2350	3.8600	2.3800
3:1:R	0.1230	0.1530	18.8000	0.0363	0.1050	0.1670	2.5700	2.0400
3:2:R	0.1330	0.1580	20.2000	0.0389	0.1010	0.4650	2.9000	1.9100
3:3:R	0.1320	0.1690	21.0000	0.0385	0.1370	1.0000	5.1000	1.9000
3:4:R	0.1290	0.1530	16.1000	0.0467	0.1220	0.7240	3.3600	2.3800
3:1:L	0.2850	0.3600	426.0000	0.0008	0.0669	-0.3130	3.1800	0.3020
3:2:L	0.2530	0.2920	482.0000	0.0007	0.0771	0.1490	3.6000	0.3020
3:3:L	0.2240	0.2570	428.0000	0.0008	0.0989	0.1670	2.7200	0.3640
3:4:L	0.2500	0.3210	408.0000	0.0008	0.0833	0.4280	3.1600	0.3640
4:1:C	0.3050	0.3780	7.5500	0.0289	0.0825	-0.1970	3.3200	2.2900
4:2:C	0.3420	0.4190	8.4600	0.0224	0.0620	-0.0515	3.1200	2.3300
4:3:C	0.3400	0.4190	6.0900	0.0292	0.0745	-0.1480	2.9000	2.5300
4:4:C	0.3180	0.5070	6.5100	0.0232	0.0767	0.1510	2.3800	2.7300
4:1:R	0.1720	0.2210	17.7000	0.0414	0.1620	0.6400	3.2000	2.2900
4:2:R	0.1380	0.1980	11.2000	0.0283	0.0627	1.7700	11.7000	2.3300
4:3:R	0.1340	0.1730	15.9000	0.0382	0.1050	-0.0998	3.4100	2.5300
4:4:R	0.1440	0.1770	15.3000	0.0462	0.1250	3.3000	2.4400	2.7300
4:1:L	0.2100	0.2780	279.0000	0.0009	0.0682	0.8100	5.7800	0.6310
4:2:L	0.3110	0.4730	131.0000	0.0008	0.0488	2.2400	11.9000	0.6310
3:3:L	0.2360	0.3200	196.0000	0.0009	0.0562	1.2400	6.9100	0.4380
4:4:L	0.2730	0.3330	361.0000	0.0009	0.0647	1.6000	4.9800	0.4380
5:1:C	0.2200	0.2710	8.9200	0.0244	0.0589	0.0220	2.6600	1.8000
5:2:C	0.1930	0.2390	11.2000	0.0307	0.0822	0.1150	2.7600	1.8900
5:3:C	0.2730	0.3630	7.0000	0.0387	0.0987	1.3200	5.4500	2.4300
5:4:C	0.2190	0.2850	8.2700	0.0303	0.0713	0.8100	5.4700	2.0900
5:1:R	0.1360	0.1710	21.6000	0.0533	0.1430	0.2940	2.5500	1.8000
5:2:R	0.1320	0.1780	17.2000	0.0238	0.1100	1.1800	5.6100	1.8900
5:3:R	0.1330	0.1650	16.2000	0.1200	0.1200	0.1380	2.1600	2.4300
5:4:R	0.1080	0.1560	12.9000	0.0389	0.0782	1.6700	8.0900	2.0900
5:1:L	0.1390	0.1850	334.0000	0.0008	0.0489	1.3400	8.6900	0.3980
5:2:L	0.1790	0.2770	254.0000	0.0006	0.0445	3.2200	26.4000	0.3980
5:3:L	0.1540	0.2220	263.0000	0.0009	0.0508	2.6800	20.2000	0.4140
5:4:L	0.1540	0.2300	254.0000	0.0008	0.0489	2.5100	16.3000	0.4140

After the virgin sample analysis, the samples were ultrasonically cleaned and subject to the wear tests as described in chapter 2. Subsequent to these tests, profilometer scans were repeated in approximately the same areas as the virgin ones, the results are tabulated below (Note: there are no results for disc 1, this is because it was not subject to any wear). The exact location varies due to the difficulty in measuring exactly at the same location.

Surface Roughness Parameters after Tribological Testing

Table 3.2, Statistical parameters of the discs at worn state.

Disc Number	**Ra**	**Rq**	**Radius of Curvature Asperities**	**Areal Density of Asperities**	**Roughness Parameter**	**Skewness**	**Kurtosis**	**Plasticity Index**
	µm	**? m**	**µm**	**µm^2**	**Beta**			
	CLA	**RMS**	**R**	h	b	**Sk**	**K**	Y
2:1:C	0.0904	0.1200	19.7000	0.0327	0.0773	-1.5700	5.5800	0.8980
2:2:C	0.0842	0.1070	13.0000	0.0620	0.0863	-0.9260	4.0400	1.0500
2:3:C	0.0894	0.1170	17.7000	0.0427	0.0744	-1.7500	6.7700	0.6660
2:4:C	0.0413	0.0603	23.2000	0.0492	0.0688	-1.6100	7.2000	0.6280
2:1:R	0.0490	0.0757	30.2000	0.0861	0.1970	-1.9800	7.5200	0.8980
2:2:R	0.0633	0.0801	22.0000	0.0627	0.1100	-0.2350	3.5500	1.0500
2:3:R	0.0373	0.0496	25.7000	0.0596	0.0762	1.0100	11.7000	0.6660
2:4:R	0.0380	0.0477	31.5000	0.0776	0.1160	-0.7170	3.1200	0.6280
2:1:L	0.0675	0.0908	1050.0000	0.0010	0.0917	-0.6730	4.4800	0.1250
2:2:L	0.0658	0.0863	1160.0000	0.0008	0.0804	-0.3120	3.5000	0.1250
2:3:L	0.0668	0.0928	1050.0000	0.0008	0.0803	-0.1050	4.9700	0.1270
2:4:L	0.0692	0.0959	1250.0000	0.0007	0.0882	0.0602	4.9400	0.1270
3:1:C	0.1820	0.2670	12.9000	0.0277	0.0955	-1.8300	6.0600	1.7000
3:2:C	0.3190	0.3920	10.3000	0.0337	0.1360	-0.0363	3.2800	2.0600
3:3:C	0.2230	0.2870	9.6500	0.0257	0.0710	-1.3100	4.1800	2.1700
3:4:C	0.2440	0.3000	11.6000	0.0320	0.1110	-0.6180	3.4600	1.4600
3:1:R	0.1600	0.1840	19.0000	0.0604	0.2100	-0.7230	2.2600	1.7000
3:2:R	0.0657	0.1120	17.3000	0.0481	0.0936	3.5500	21.6000	2.0600
3:3:R	0.1820	0.2760	14.3000	0.0414	0.1640	-0.8100	7.7100	2.1700
3:4:R	0.0275	0.0368	33.5000	0.0907	0.1120	1.4200	6.0500	1.4600
3:1:L	0.1590	0.2670	647.0000	0.0006	0.0985	0.2110	7.6100	0.2860
3:2:L	0.1740	0.2720	698.0000	0.0005	0.1070	-1.0700	4.9300	0.2860
3:3:L	0.1610	0.2610	696.0000	0.0006	0.1110	-1.8900	10.4000	0.3010
3:4:L	0.1490	0.2210	461.0000	0.0007	0.0800	-1.2500	24.7000	0.3010
4:1:C	0.2110	0.2720	8.9800	0.0298	0.0728	-0.3330	4.3800	1.9800
4:2:C	0.1770	0.2370	8.7600	0.0357	0.0740	0.0329	5.3700	1.6800
4:3:C	0.1550	0.2280	9.0900	0.0336	0.0697	-1.1100	6.4700	1.7300
4:4:C	0.1930	0.2630	7.4900	0.0327	0.0644	0.4200	5.5000	1.6800
4:1:R	0.1000	0.1620	14.0000	0.0379	0.0857	0.8520	9.3800	1.9800
4:2:R	0.0770	0.0989	18.0000	0.0552	0.0984	0.3510	4.7800	1.6800
4:3:R	0.0732	0.1190	15.5000	0.0414	0.0766	3.5300	20.5000	1.7300
4:4:R	0.0505	0.0641	23.7000	0.0693	0.1050	-0.0486	3.3100	1.6800

Disc Number	**Ra**	**Rq**	**Radius of Curvature Asperities**	**Areal Density of Asperities**	**Roughness Parameter**	**Skewness**	**Kurtosis**	**Plasticity Index**
	µm	**? m**	**µm**	**µm^2**	**Beta**			
	CLA	**RMS**	**R**	h	b	**Sk**	**K**	Y
4:1:L	0.1500	0.2100	367.0000	0.0009	0.0698	0.8950	6.2000	0.4010
4:2:L	0.1560	0.2720	238.0000	0.0009	0.0570	3.5700	34.0000	0.4010
4:3:L	0.1360	0.2110	291.0000	0.0009	0.0552	2.0600	19.3000	0.3570
4:4:L	0.1380	0.2010	346.0000	0.0009	0.0613	0.9090	10.7000	0.3570
5:1:C	0.1254	0.1497	18.3000	0.1100	0.3260	-0.6990	2.3300	1.2900
5:2:C	0.1141	0.1398	16.3000	0.0789	0.3140	-0.8640	4.6000	1.1200
5:3:C	0.1310	0.1640	16.9000	0.1010	0.3920	-0.6800	2.1800	1.1870
5:4:C	0.1238	0.1529	16.9000	0.0984	0.1140	-0.5872	3.4800	1.26300
5:1:R	0.3390	0.4920	10.1000	0.0298	0.1480	0.0444	4.2200	1.8900
5:2:R	0.4600	0.6140	9.1100	0.0236	0.1320	-0.0838	3.4400	2.1200
5:3:R	0.8120	1.0500	13.4000	0.0177	0.2480	0.0164	2.6400	0.2070
5:4:R	1.3300	1.4800	9.0800	0.0216	0.2900	-0.4050	1.8800	3.6300
5:1:L	0.1100	0.1490	468.0000	0.0008	0.0572	0.3610	4.8600	0.2460
5:2:L	0.1150	0.1600	536.0000	0.0007	0.0600	0.5460	4.9800	0.2460
5:3:L	0.1180	0.1720	432.0000	0.0008	0.0787	2.9300	20.5000	0.2860
5:4:L	0.1090	0.1530	548.0000	0.0007	0.0593	0.5540	5.3300	0.2860

The tables above represent the data collected from the scan. To understand better the trend that exists from one disc to the other, it was decided to find the average values of the parameters for each of the 5 discs. These averages were carried out by adding the specific parameters of each quadrant and then dividing by 4, to provide one value for that disc (also depicted by the formula below).

Disc 1;

$$Ra_{\text{average of disc 1}} = (Ra_{\text{quadrant 1}} + Ra_{\text{quadrant 2}} + Ra_{\text{quadrant 3}} + Ra_{\text{quadrant 4}})/4 \qquad \textit{(Equation 3.1)}$$

This formula was used to calculate the averages of all the statistical parameters being analyzed.

These average values were then plotted against each other (the average values of the different discs) to examine the trends that occur as the surface evolves from its virgin to worn state. The plots are given and described below.

3.5.2 Statistical Surface Parameters:

After finding the averages as previously discussed, we proceed to plotting them so as to establish any patterns that are formed as the surface evolves from its virgin state to its worn state.

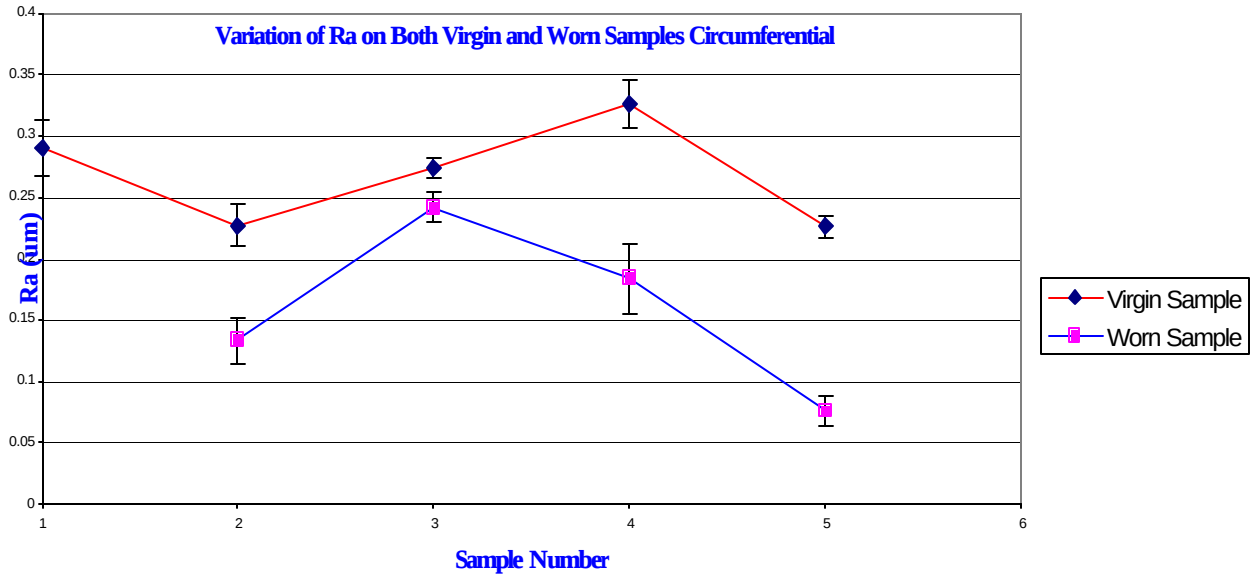

Figure 3.17, Plot of variation of Ra on both virgin and worn sample in circumferential direction

Center Line Average (Ra) Trends:

This is a plot that summarizes all the average Ra values for the 5 discs in the study the standard deviation of al the virgin scans in the circumferential direction is 0.0714µm. The error bar used in the figures is for ± one standard deviation. The data plotted are an average of all the 4 points in a specific direction on a given disc as explained earlier. The general trend in this graph is that as the surface moves from virgin to worn stage, the Ra reduces. This means that the peak asperities are worn out and the surface gets polished. As for the individual results, from the graph there is a change from the virgin to 0.25 T scuffed, the surface is polished and smoothened out. The 0.5T scuff shows a slightly different trend, the surface appears rougher that that of the virgin but this mat simply be caused by the fact that the virgin 0.5xT was rougher, and the variation seems to be within error range. At 0.75T scuff there is a reduction in Ra compared to the increase in the previous disc, supporting progressive wear of the surface until the sample scuffs. Now we proceed to the Rq chart to investigate its results.

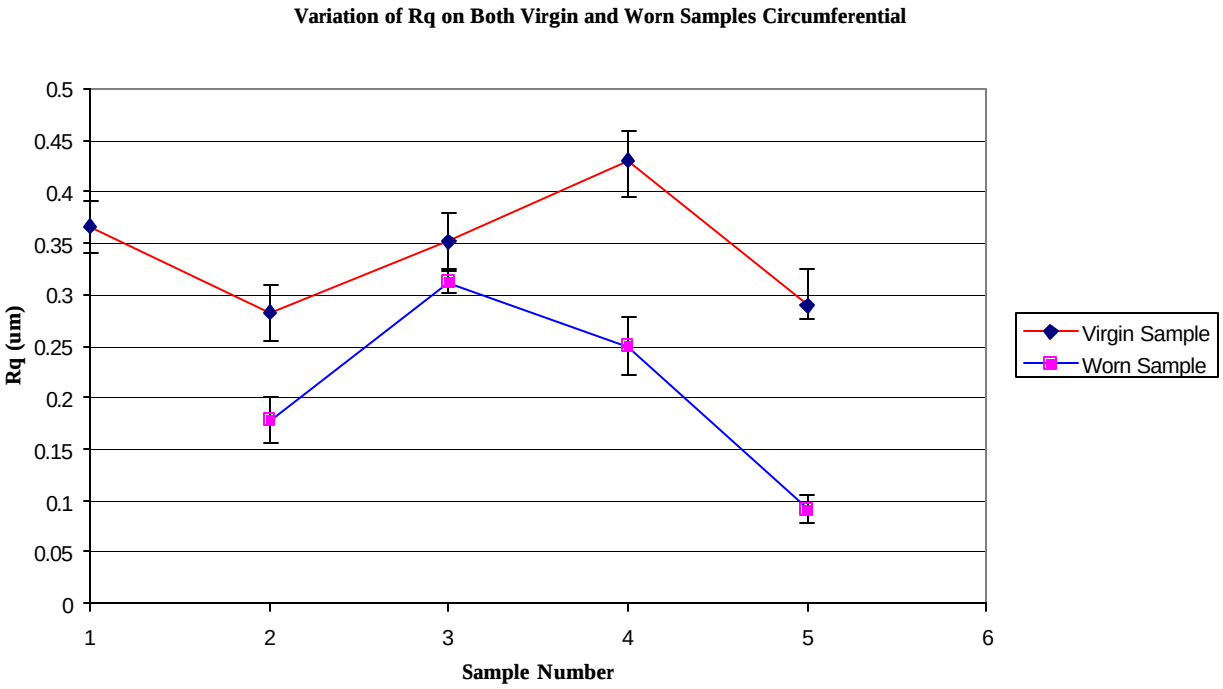

Figure 3.18, Rq variation of on both virgin and worn sample in circumferential direction

RMS (Rq) Trends:

This chart has similar trends as those portrayed in the previous graph, which confirms that the surfaces here are Gaussian. The general trend in this graph is that as the surface moves from virgin to worn stage the Rq reduces The reason for this reduction is the fact that the asperities are smoothened thus reducing the roughness. As for the individual results, from the graph the data suggests progressive wear of the surface until it finally scuffs. The surface does not change much from the 0.25xT to 0.5xT, however the overall picture does suggest progressive wear.

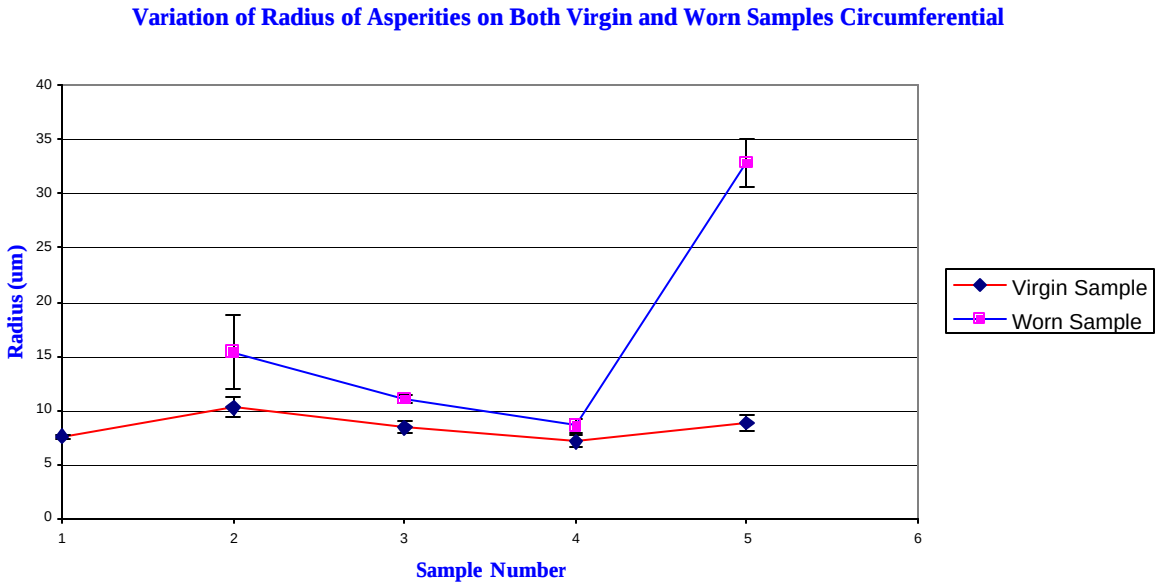

Figure 3.19, Plot of variation of Radius of Asperities on both virgin and worn sample in circumferential direction

Average Radius of Curvature of Asperities:

The general trend exhibited by this set of data is that, as the surface is worn out the radius of curvature of the asperities increases. An explanation for this is that, as the asperities are polished out, a larger radius of curvature is achieved. As for the individual cases at the 0.25T scuff, the maximum change in radius occurs, the following ones (0.5 T and 0.75T), the radius increases decreasingly (compared to the virgin surface), for the scuffed surface, the radius of asperities is much higher than the rest. This is however expected since the surface has undergone severe plastic damage. The conclusion from these graphs is that as a surface undergoes the evolution of wear, the radius of its asperities increase because the asperities are polished.

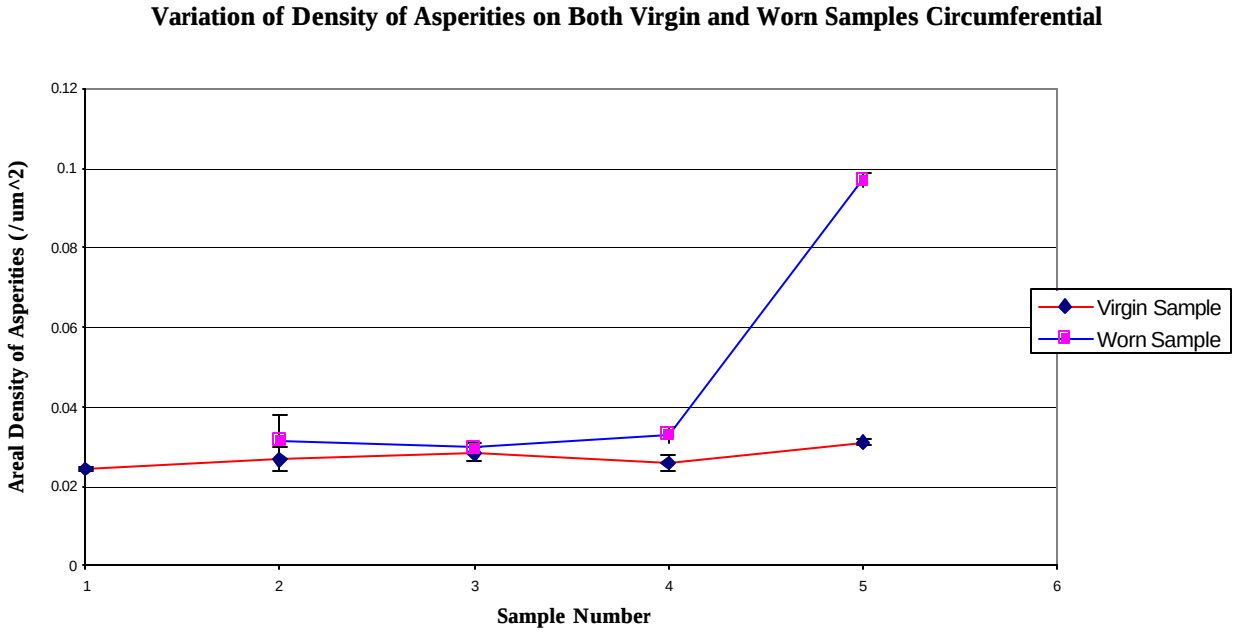

Figure 3.20, Plot of variation of Density of Asperities on both virgin and worn sample in circumferential direction

Areal Density of Asperities:

This parameter tends to look at the number of asperities in a given area, this parameter depends on the manufacturing process and does not change considerably for minor wear. The virgin samples have very consistent results as far as the initial density of asperities is concerned. As the surfaces are worn out the density increases in most cases, this is contrary to intuition, because as the radius of asperities increases it is expected that the density will decrease. However, as the surfaces are smoothened out, the minor asperities that were not recorded get counted as asperities now, thus increasing the count. The scuffed sample shows large increase in density, however as mentioned before this may be due to plastic deformation.

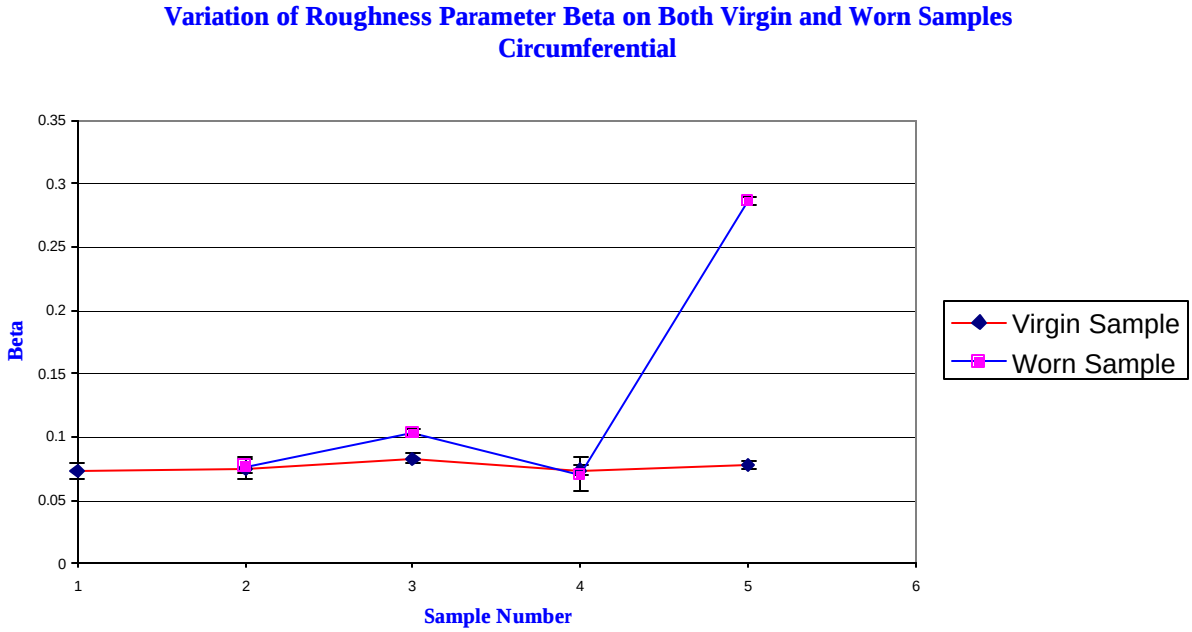

Figure 3.21, Plot of variation of Roughness Parameter on both virgin and worn sample in circumferential direction

Roughness Parameter** b**;

This parameter is the product of η,σ, and R, it is mainly used as a 'check' of the roughness parameters extracted by the analytical methods, and usually ranges between 0.02 to 1.0. Both the virgin and the worn samples show similar results, there is little change from the virgin to the worn state, however some change occurs in the 0.5T, but none significant enough to establish justifiable trends. The scuffed surface has a high β value indicating that this surface is different from the other surfaces in this group.

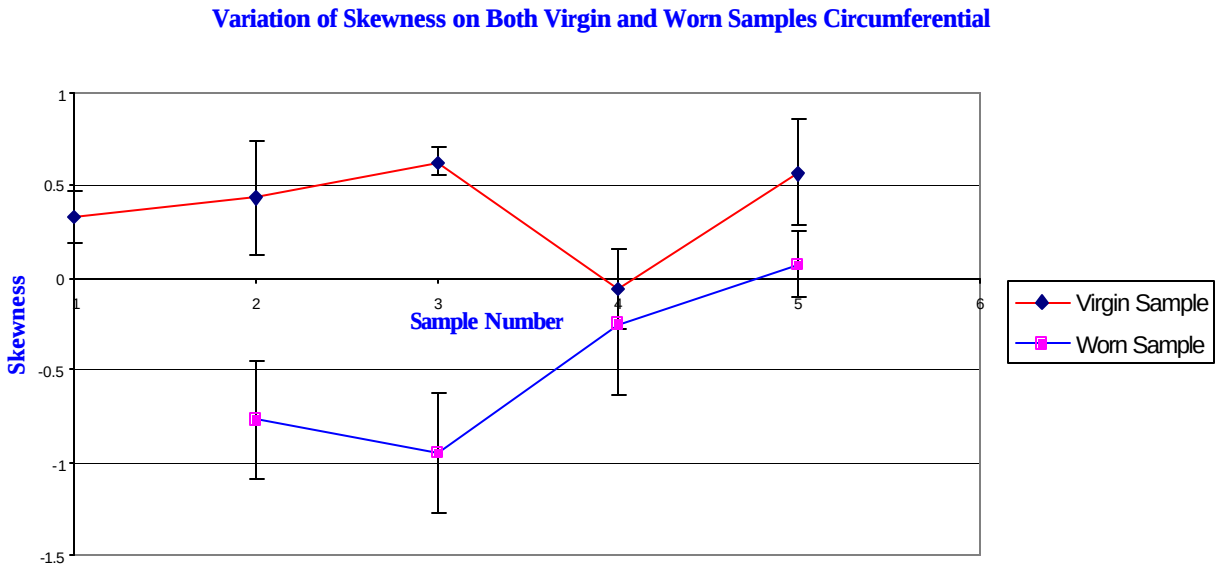

Figure 3.22, Plot of variation of Skewness on both virgin and worn sample in circumferential direction

Skewness Parameter

This parameter gives us some of the most important finding from this study. As mentioned earlier, there seems to be progressive wear. From the graph above, it can be seen that the virgin state has a positive skewness, indicating high peaks and deep valleys. In the worn stage the skewness turns negative for all but the scuffed sample. This supports the fact that all the asperities are being knocked down and we remain with the pits rather than the peaks, these broken asperities undergo wear, thus forming peaks and valleys eventually raising the skewness of the surface. From sample 1 to 2, there is a great change in skewness, it can be hypothesized that the peaks have been polished, thus the presence of deep valleys (as compared to peaks) contributes to a negative skewness. As we move to sample 3, we still have a negative skewness, due to further smoothening of the peaks. Sample 4 and 5 show similar results, the wear begins to affect the valley, which contributes to a positive increase in skewness parameter. Previous studies indicate that with 'regular' mild wear-in, the initial surface begins with a positive skewness (due to machining process), due to plastic deformation the asperities wear out giving the surface a skewness of about –0.5, where the asperities deform elastically which is not the case with these data. From our study we support the theory that as a surface is worn out the skewness decreases to a point (0.5xT) after which it increases until it scuffs.

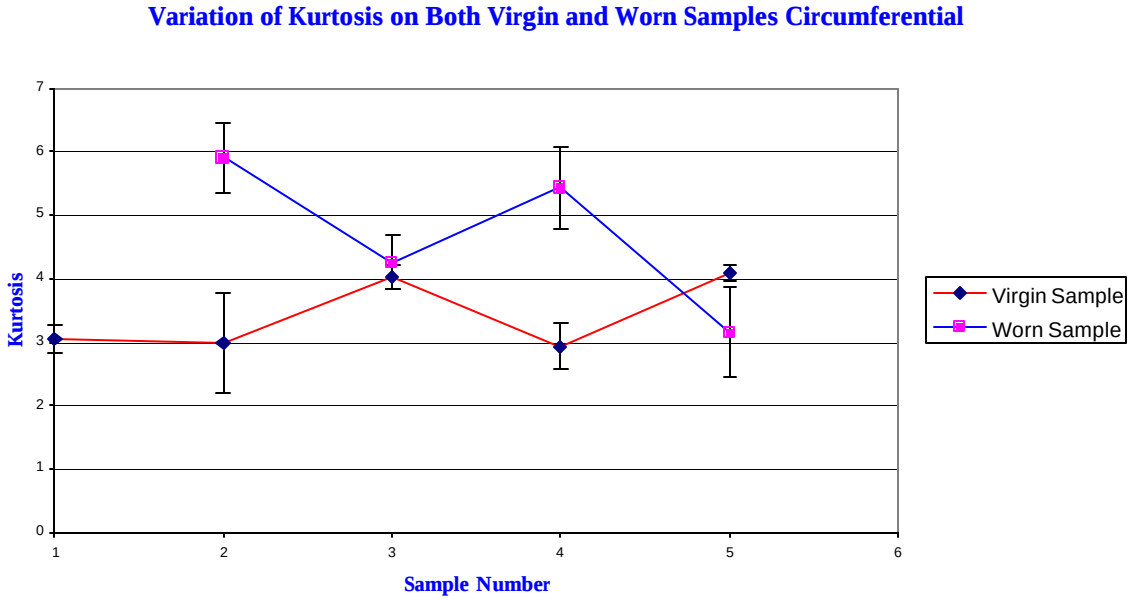

Figure 3.23, Plot of variation of Kurtosis on both virgin and worn sample in circumferential direction

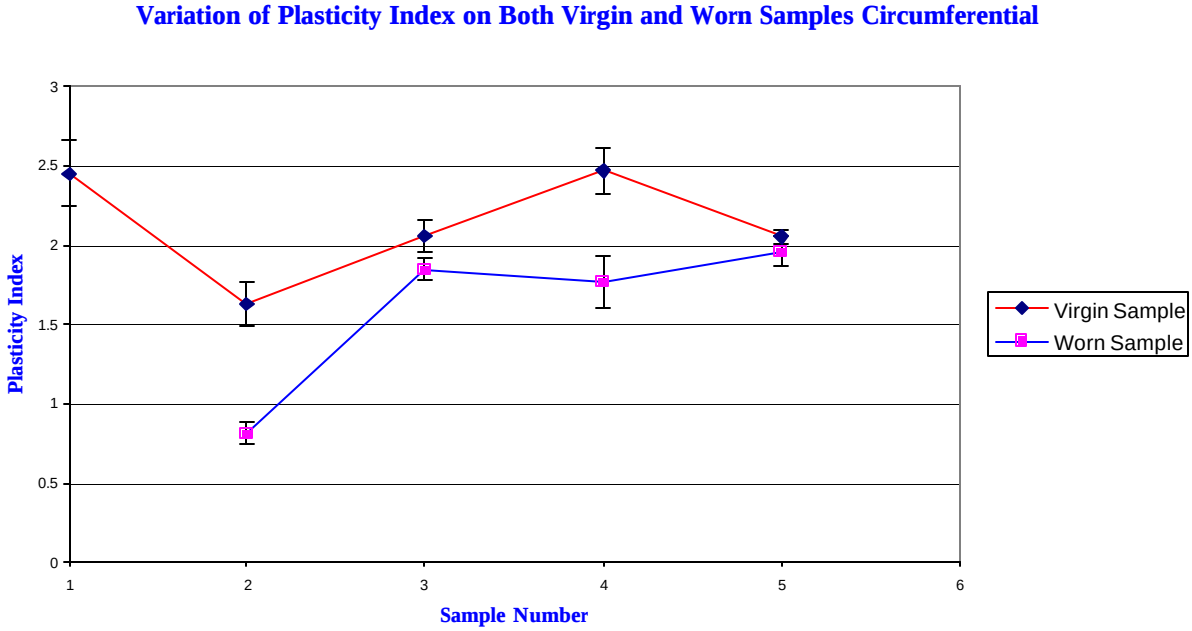

Figure 3.24, Plot of variation of Plasticity index on both virgin and worn sample in circumferential direction

Kurtosis & Plasticity Index

Kurtosis is the fourth moment of the surface. The general trend in this graph is that the virgin state has a Gaussian distribution ($K \approx 3$). As the sample is worn out the kurtosis becomes leptokurtic. This graph does not yield

any substantial conclusions. The plasticity index chart shows that all the regions are subject to plastic deformation and is calculated by the following equation:

$$y = \frac{E^*}{H}\left[\frac{s}{Rs}\right]^2$$

Ψ= Plasticity Index

E*= Composite Youngs Modulus (6.89×10^{10})

H= Hardness (6×10^9)

ν= Poissons Ratio

W= Load

Rs= Radius of Contact

The values for Young's modulus E* and hardness H were kept constant and the values correspond to the bulk properties due to the fact that we don't know the properties of the surface layers. The plasticity index reveals that the surface undergoes plastic deformation at all times, confirming that these surfaces are relatively rough. This concludes our profilometer data analysis

3.6 Conclusion:

From the study presented above, we suggest that progressive wear occurs as virgin surface undergoes wear, the asperity peaks are smoothened till scuffing occurs. The profilometer scans and the statistical parameter graphs fully support this observation. A more important finding arises from the fact that the worn surfaces posses a primary scar which is dominant in sample 2, furthermore as the load is increased even wear occurs thus the dominance is not as strong. However the scar does exist and scuffing occurs at within the primary wear scar (Figures 2.10-2.13), thus indicating the fact that the surface topography does a vital role in scuffing. Figure 2.8 in Chapter 2 shows the location of the primary wear scar on the steel shoe. It is hypothesized that initially (0.25xT) the load is minimal, thus a primary scar is formed at the point of contact, As the load is increased this point of contact is elastically deformed allowing even contact pressure thus a wider wear scar (Samples 3 & 4), eventually as more load is applied the surface eventually fails at the region of the primary wear. This hypothesis is supported by the optical images and the long wear scans. Summarizing this chapter we can say that we have studied the surface roughness from the millimeter range to the micrometer range, and have concluded that the surface roughness parameters do support the hypothesis that a primary wear scar is formed within the overall wear scar and is sustained over the duration of wear, and finally is the zone of scuffing. We now undertake the second task to study the chemical changes that occur on and in the aluminum alloy that eventually lead to its failure.

Chapter 4: Nano-Scale Surface and Sub-Surface Chemical Analysis of Al-390

4.1 Introduction

High pressure and temperature often lead to change in chemical composition of materials. This part of the study deals with changes in chemical composition that occur on the surfaces and sub-surfaces of aluminum alloys as they evolve from virgin to worn to scuffed stage. Previous studies done by Yoon 1999 at the micrometer scale, suggested that one of the main barriers to early scuffing is the oxide layer present on the surface of the aluminum alloy. Once this layer has been destroyed, sub-surface damage occurs eventually leading to scuffing. In this study, we try to investigate the changes in chemical composition that occur, which in turn may affect material properties at the nanometer scale. With this goal in mind it was decided to choose two methods of chemical analysis that are suitable for this study. After a study of several existing and available methods, it was decided to use Auger Electron Spectroscopy (AES) and X-Ray spectroscopy (XPS), because these methods can provide data about the element composition and concentration within the samples. Other analytical methods are described in the Appendix 2. With the methods mentioned above, one has to be very careful in manipulating the specimen, for even a fingerprint could ruin the data. These two methods are very accurate, and require precision to obtain acceptable results. The brief description that follows better explains the fundamentals and working mechanisms of these chemical analysis processes.

4.1.1 Auger Electron Spectroscopy (AES):

The Auger effect was discovered by Auger in 1925 while working with X rays. Auger electrons are produced when incident radiation (photons, electrons ions or neutral atoms) interacts with an atom with an energy exceeding that necessary to remove an inner shell electron from the atom. This interaction leaves the atom in an excited state with a core hole. The excited atoms are unstable, and de-excitation occurs immediately, resulting in the emission of an x-ray or an electron termed as Auger electron. An excited atom with a core level hole can decay to a lower energy state in several ways, of which the Auger and X-Ray are the most probable. X-ray serves better for inner orbital of heavy metals, while Auger is more sensitive for lighter elements (Childs, 1995). Figure 4.1 shows the typical principal auger electron energies.

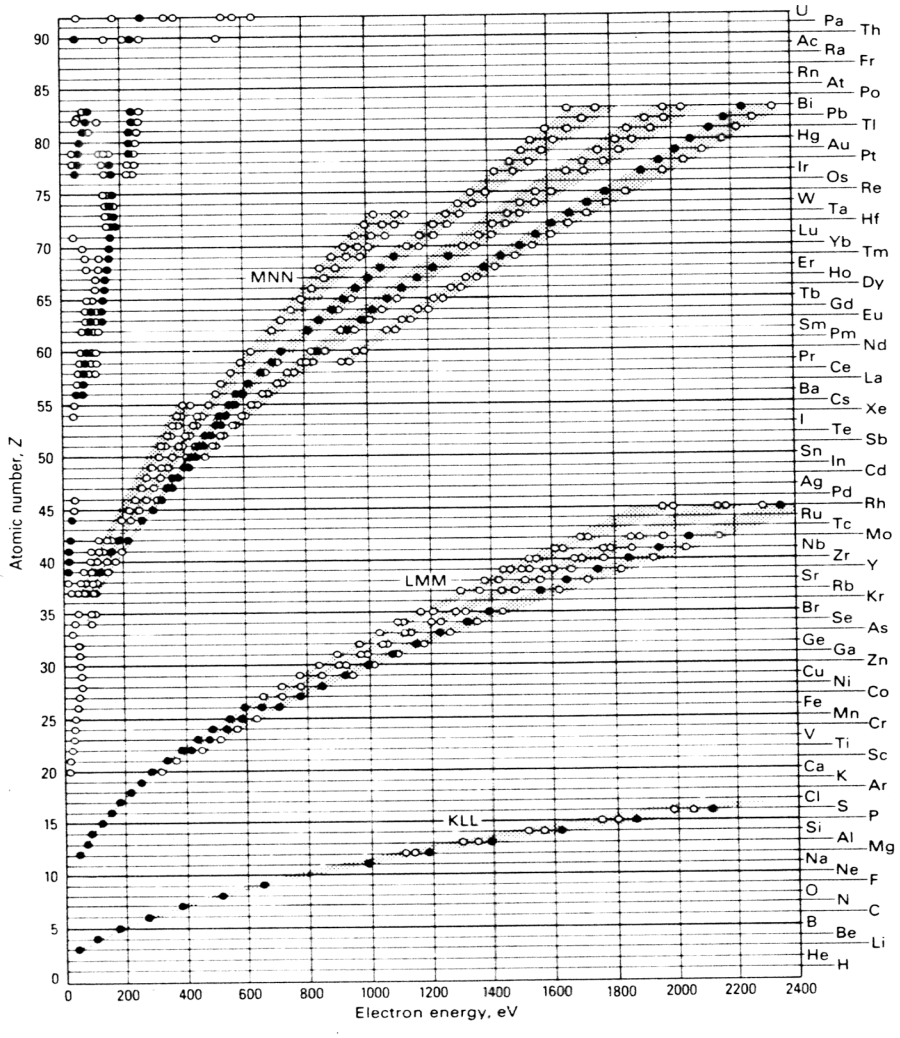

Figure 4.1, Chart of principal Auger electron energies for the various shell KLL, LMM and MNN.

4.1.2 Experimental methods:

The AES typically includes an electron gun for primary -electron excitations of the sample, an electron spectrometer for energy analysis of secondary electrons, a secondary electron detector for secondary electron imaging, a stage for manipulation, and an ion gun for sputtering the surface of the sample. Because the AES technique is surface sensitive, an essential requirement is a UHV system capable of an ultimate vacuum of 10^{-10} Torr. The instrument may be equipped to carry out other functions such as thin film deposition. The electron spectrometer is usually the central component of the AES system, and is usually equipped with a certain analyzer. The cylindrical mirror usually offers a better signal to noise performance for excited electrons.
Operation of a cylindrical mirror analyzer to obtain Auger spectra is illustrated in Fig. 4.2.

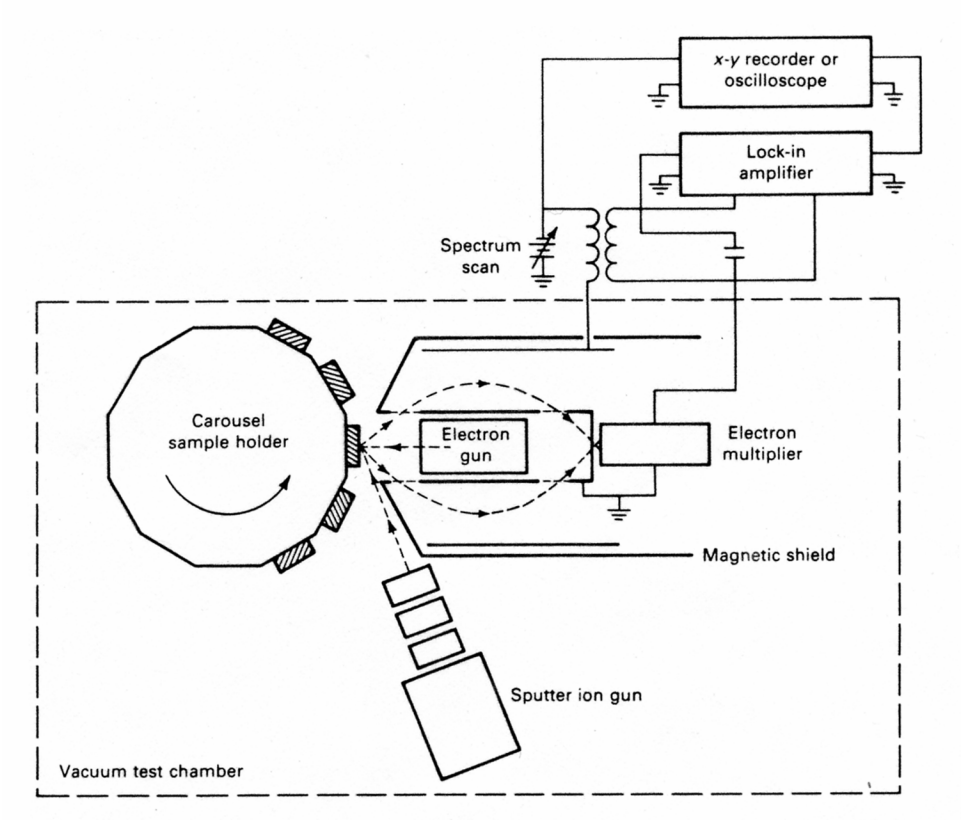

Figure 4.2, Operation of a cylindrical mirror in an Auger spectrometer.

The electron gun, commo nly located coaxially to the cylindrical mirror analyzer, provides primary electrons. A portion of the electrons scattered from the sample surface enter the inlet aperture of the cylindrical mirror analyzer and traverse the space between the inner and outer cylinders of the cylindrical mirror analyzer. A negative bias applied to the outer cylinder directs electrons. The pass energy of the cylindrical mirror analyzer and the kinetic energy of detected electrons are proportional to the bias applied to the outer cylinder (Joshi, 1995).

Data Acquisition:

The electron energy distribution, N(E) plots, contain direct information of Auger transitions. The dN(E)/dE function, which reduces the effect of high (exaggerated peaks and valleys) background, can be generated by electronic or digital conversion methods. The electronic method of generating dN/dE involves superimposition of a small alternating current (ac) voltage on the outer cylinder and synchronous detection of the in-phase component of the analyzer output using a lock-in amplifier. The data can be displayed directly in the N(E) form or differentiated digitally to obtain the dN/dE format. Although N(E) data contain the most complete information, the dN/dE form of display has become the standard way of representation. The instrument allows the possibility to obtain depth profiles in conjunction with ion sputtering. Auger electron spectra from large areas can be obtained by using defocused electron beams or by rastering a selected area. Rastering is often preferred because it permits a clear definition of the area under investigation and limits edge effects. The maximum area of analysis is approximately 0.5 mm in diameter

for the rastering mechanism. Energetic inert gas ions, for example, argon, from 1 to 5 keV are used to sputter the surface, followed by AES in depth profiling (Joshi, 1995).

4.1.3 Experimental Limitations

Like every other instrument, the AES is limited to certain uses. Some of the limitations are described below:

- Elemental Detection Sensitivity. Limitations of the technique include its insensitivity to hydrogen and helium and its relatively low detection sensitivity for all elements. Because the Auger process involves three electrons in a given atom, hydrogen and helium cannot be detected.
- Sputtering Artifacts. Another important limitation arises from use of surface atom removal techniques, such as sputter etching. Many of the surface layers sputtered consist of a mixture of compounds and elements. Because the sputter rates for such layers are unknown, only an estimation of the layer thickness is possible. This is often sufficient to help solve problems. In addition, sputtering artifacts, such as ion beam mixing, differential sputtering, and cone formation, can confuse the data (Harris 1968).
- Sample charging due to electron beams is another common problem with AES applied to insulating materials. Charging causes peak shifts in the spectrum and in severe cases prevents obtaining useful data. As a result of these limitations, most AES applications involve good conductors, such as metals, their alloys, and semiconductors. Oxides, other insulators, and organic materials have been examined, but often with limited success.
- High vapor pressure samples pose another limitation for AES analysis. A sample is vacuum compatible if its vapor pressure is low enough not to degrade or ruin the vacuum in the spectrometer-normally less than 10^{-8} Torr. If the sample out-gasses at a high rate, the surface chemistry may change upon introduction into the vacuum chamber, and the vacuum may be degraded.
- Electron Beam Artifacts. This limitation involves the primary electron beam used in Auger electron excitation. Electrons interact with matter more readily than x-rays and may cause electron beam artifacts. Electron beams can change the surface by promoting migration of atoms into or out of the area of analysis. Poor thermal conductivity of the sample also causes localized heating and associated artifacts. Such effects include decomposition of surface materials typically with organic, biological, and selected inorganic compounds (Joshi, 1995). Great care was taken to analyze the Aluminum samples making sure that the above mentioned problems do not affect the data.

4.2 XPS

The X-ray Photoelectron Spectroscopy (XPS) technique was invented in 1967 by professor Kai Siegbahn at the University of Uppsala, Sweden (Seimann, 1988). The technique was first known by the acronym ESCA (Electron Spectroscopy for Chemical Analysis). Irradiating a solid in vacuum with a mono-energetic source, and

analyzing the emitted electrons by the energy level to achieve surface analysis by XPS. The spectrum is obtained as a plot of the number of detected electrons per energy interval versus their kinetic energy, either low energy x-rays (soft x-rays) or electrons can be used as the exciting radiation. X-rays are gentler than electrons and cause less sample decomposition and charging. Mg Ka (1253.7 eV) or Al Ka (1486.6 eV) filaments are used to produce the x-rays (Perkin-Elmer, 1985). These photons have limited penetrating power in a solid on the order of 1 to 10 micrometers, thus, they interact with atoms in the surface region, causing electrons to be emitted by photoelectric effect. The kinetic energy of the emitted electrons is recorded and related to the binding energy of the atomic orbital from which the electrons originate. The binding energy may be regarded as the energy difference between the initial and final states after the photoelectron has left the atom. The core electrons are subject to attractive forces from the nucleus and repulsive forces from the electrons surrounding them.

If an electron is removed from the outer shell, the screening of the inner electron is reduced by one electron charge, and the core electrons feel an increased force of attraction from the nucleus. The gain of an outer electron, for example through radiation, effectively increases the shielding and decreases binding energy. The x-rays impinging on the surface in XPS produce the photo-ejection of the core electrons. The quantity ultimately measured by the XPS system is the binding energy of the ejected electrons. Because each element has a unique set of binding energies, XPS can be used to identify and determine the concentration of the elements in the surface. The XPS spectrum contains both photoelectron and Auger electron peaks, representing the sample surface. Chemical shifts caused by different chemical environments also occur with Auger lines, which may provide very useful chemical state information when combined with the shifts of photoelectron lines. The major advantage of XPS over Auger spectroscopy is its ability of obtaining more complete and easy to detect chemical bonding information. Auger spectroscopy on the contrary offers a higher spatial resolution.

The Auger electron emission occurs roughly 10^{-14} seconds after the photoelectric event. In the Auger process, shown in Figure 4.3, an outer electron falls into the inner orbital vacancy, and a second electron is emitted, carrying off the excess energy.

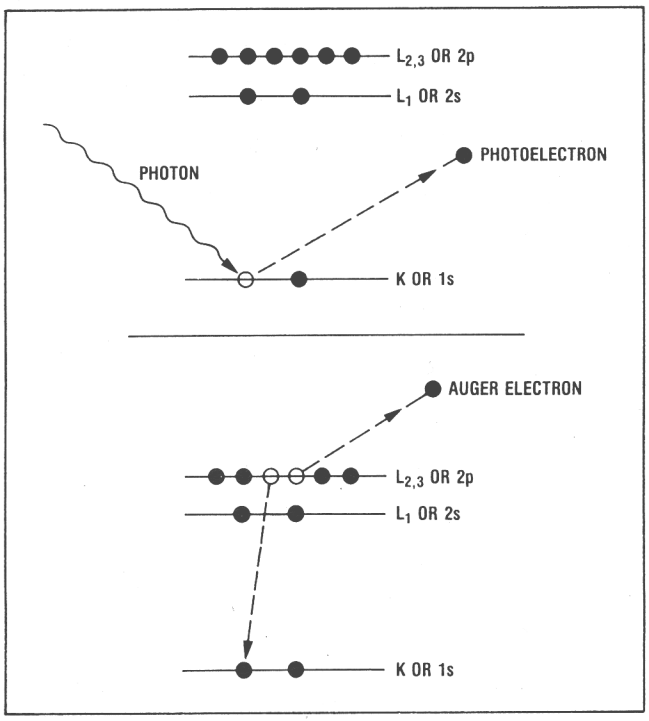

Figure 4.3, diagram of photoelectric process and Auger process.

The Auger electron possesses kinetic energy is equal to the difference between the energy of the initial ion and the doubly charged final ion, and is independent of the mode of the initial ionization. Thus, photo-ionization normally leads to two emitted electrons, a photoelectron and an Auger electron. Probabilities of interaction of the electrons matter far exceed those of the photons, so while the path length of the photons is in micrometers, that of the electrons is in tens of Angstroms. Thus, while ionization occurs to a depth of a few micrometers, only those electrons that originate within tens of Angstroms below the solid surface can leave the surface without energy loss. The electrons leaving the sample are detected by an electron spectrometer according to their kinetic energy. The analyzer normally is operated as an energy 'window' accepting only those electrons having energy within the range of this fixed window, referred to as the pass energy. Scanning for different energies is accomplished by applying a variable electrostatic field, before the analyzer is reached (Perkin-Elmer 1985).

4.2.1 Experimental Procedure.

A schematic of a typical XPS is shown in Figure 4.3. This figure indicates the relationship of major components, including the electron energy analyzer, the x-ray source, and the ion gun used for sputter etching. The precision electron energy analyzer, incorporated in the ESCA is a double pass, cylindrical-mirror type analyzer (CMA) with a retarding grid input stage. The x-ray source is a standard flange mounted physical electronics source, which can be configured with magnesium or an aluminum anode. The x-ray source is located perpendicular to the analyzer axis and the ion beam is nearly normal to the sample surface. The analysis must be carried out in vacuum not to alter the surface chemical state while acquiring data; a vacuum of at least 10^{-8} Torr is required to achieve a meaningful analysis. The source must produce an intense mono-energetic stable beam of either photons, electrons or

x-rays of sufficient energy to excite the electrons of interest in the solid surface examined. Typically, targets are made of magnesium or aluminum. These elements give rise to x-ray photon energies of 1253.7 and 1486.6 eV respectively. This is enough energy to excite the Is and valence levels of the atoms in the first row of the periodic table, the 2s and 2p and valence levels of second row elements and so on.

The beam is directed onto the sample at its surface where it impinges on the material to be studied and causes the ejection of electrons. The specimen-mounting angle is critical in XPS, and does have some effect on the spectra. A low electron take-off angle accentuates the spectrum of any segregated layer on the surface, whereas a sample-mounting angle normal to the analyzer axis minimizes the contribution of such layer (Moulder, 1995).

The electron energy analyzer sorts out the resulting electrons according to their kinetic energy and focuses them on a detector at the output. The analyzer is operated as an energy window referred to as the pass energy, accepting only those electrons having energy within the range of the window. Scanning for different energies is accomplished by applying a variable electrostatic field before the analyzer. Electrons are detected as discrete events and the number of electrons for a given detection time and energy are stored and displayed. The detector produces an electrical signal proportional to the intensity of the electron beam, and the readout system translates it into graphic form.

In the ESCA/SAM System, energy distribution, energy resolution and the size of the analysis area are strictly a function of the analyzer. The size of the analysis area is defined by the size of the circular apertures at the output of the CMA stages. Analyzer energy resolution (AE/E) is also determined by these analyzer, three different aperture sizes are available, the large apertures results in maximum signal intensity, a circular analysis area approximately 5mm in diameter, and energy resolution which is 2% of the pass energy.

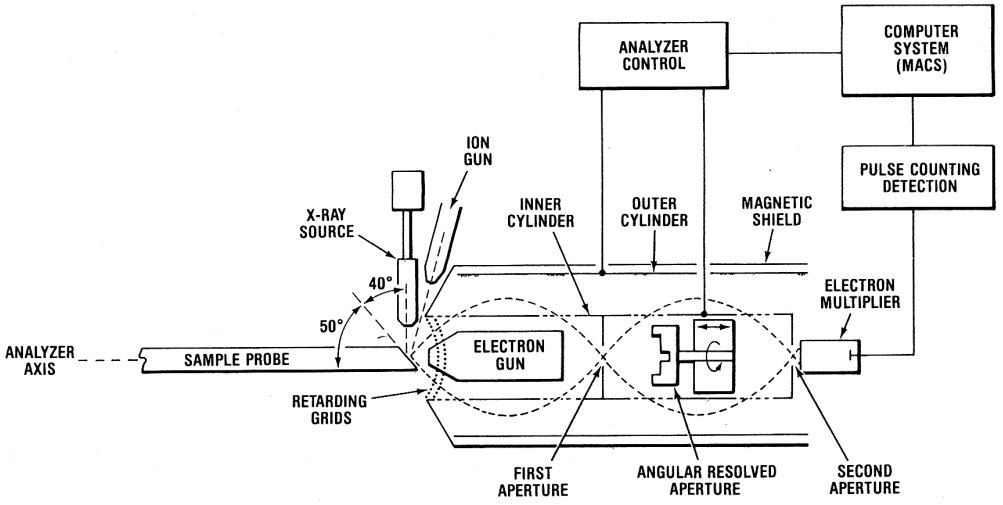

Figure 4.4, schematic of a PHI model 550 XPS.

Data Interpretation:

The photon energy of an element minus the spectrometer work function corresponds to a binding energy of zero with reference to the Fermi level. There are several kinds of lines used to identify the peaks, which in turn are

used to identify compounds. These kinds of lines are listed and explained below as explained in the Perkin-Elmer Handbook for XPS:

- Photoelectron Lines. The most intense of the photoelectron lines are usually relatively symmetrical and are typically the narrowest lines observed in the spectrum. Photoelectron lines of pure metals can, however, exhibit considerable asymmetry due to coupling with conduction electrons. All of the photoelectron lines of insulating solids are of the order of 0.5 eV wider than photoelectron lines of conductors.
- Auger Lines. These are more proper groups of lines in rather complex patterns. There are four main Auger series observable in XPS, they are the KLL, LMM, MNN, and NOO series, identified by specifying the initial and final vacancies in the Auger transition. The KLL series, for example, includes those processes with an initial vacancy in the K shell and final double vacancy in the L shell. The symbol V, e.g. KVV, indicates that the final vacancies are in valence levels. Auger lines have kinetic energies that are independent of the ionizing radiation, thus they appear on a binding energy plot to be in different positions when ionizing photons of different energy (i.e. different x-ray sources) are used.
- X- Ray Satellites: The x-ray emission spectrum used for irradiation exhibits not only the characteristic x-ray, but also some minor x-ray components at higher photon energies. For each photoelectron peak that results from the Ka x-ray photons, there is a family of minor peaks at lower binding energies, with intensity and spacing characteristic of the x-ray anode material.
- X-ray "Ghosts". These are mainly due to contamination and can be ignored from the analysis.
- Shake-Up Lines. When an ion is left in an excited state, a few electron volts above the ground state, the kinetic energy of the emitted photoelectron is reduced, with the difference corresponding to the energy difference between the ground state and the excited state. This results in the formation of a satellite peak a few electron volts lower in kinetic energy (higher in binding energy) than the main peak.
- Multiplet Splitting. A photoelectron line that is split asymmetrically into two components is formed by emission of an electron from a core level of an atom that itself has a spin (unpaired electrons in valence levels) can create a vacancy in two or more ways.

Once the data are obtained from the XPS, keeping the mentioned lines in mind, and using standardized books, the compound are identified by the binding energy of their peaks.

4.2.2 Summary of XPS

X-Ray Photoelectron Spectroscopy (XPS), also known as Electron Spectroscopy for Chemical Analysis (ESCA), is a surface analysis technique used for obtaining chemical information about the surfaces of solid materials. Insulators and conductors can easily be analyzed from areas a few microns and larger. The method utilizes an x-ray beam to excite a solid sample resulting in the emission of photoelectrons. An energy analysis of these

photoelectrons provides both elemental and chemical bonding information about the material comprising the sample surface. All elements, except hydrogen and helium can be detected. In XPS analysis, the sample is placed in an ultrahigh vacuum environment and exposed to a low-energy, monochromatic X-ray source; x-ray excitation causes the emission of photoelectrons from the atomic shells of the elements present on the surface. The energy of these electrons is characteristic of the element from which they are emitted. By counting the number of electrons as a function of energy, a spectrum representative of the surface composition is obtained. The area under peaks in the spectrum is a measure of the relative amount of each element present, and the shape and position of the peaks reflect the chemical state for each element. XPS is a surface sensitive technique because only those photoelectrons generated near the surface can escape and become available for detection. Due to collisions within the sample's atomic structure, those photoelectrons originating much more than about 20 to 100 Å below the surface are unable to escape from the surface with sufficient energy to be detected.

4.3 AES Experiments on Aluminum Samples:

Depth profiling is a very attractive feature of this technique, which allows us to follow the changes in chemical composition that occur as we penetrate through the surfaces moving into the sub-surfaces of the sample. The samples from the HPT were cut into smaller pieces using a low speed diamond saw. These pieces were then ultrasonically cleaned in a pool of acetone, then rinsed in alcohol and dried using a dry hot air. In the Auger, the raster size was set to 0.7mmx0.7mm, sputtering an area of about $0.5mm^2$, however the data analysis area was only $0.5\mu m^2$. The sputtering rate was established to be approximately 12nm per minute based on an approximation made using silicon sputter rates. The tests were run and depth profiles obtained for each of the 5 test sets. The five figures shown below (figures 4.5 to 4.9) show optical images of the area in which the depth profiling was carried out.

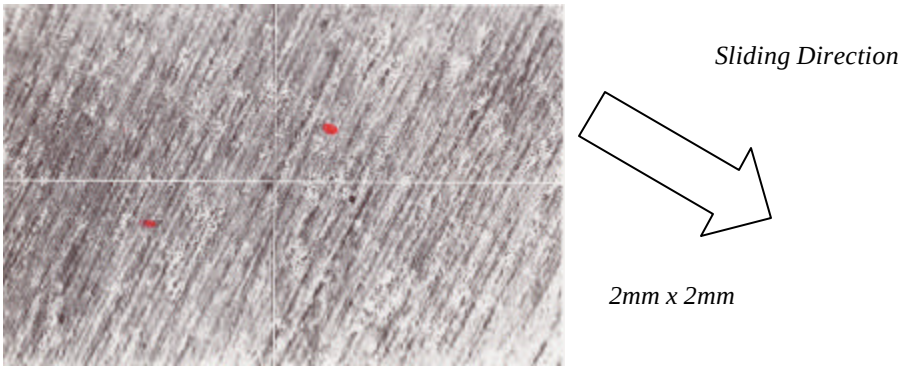

Figure 4.5, Location of AES Depth profiling on Sample 1, Virgin.

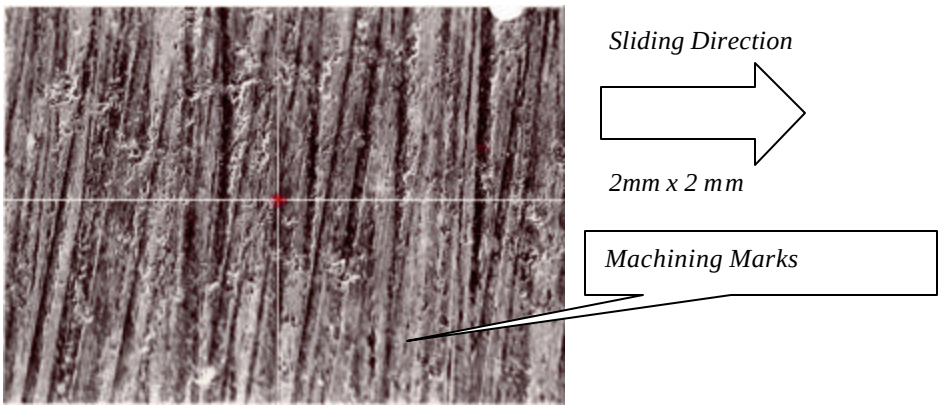

Figure 4.6, Location of AES Depth profiling on Sample 2

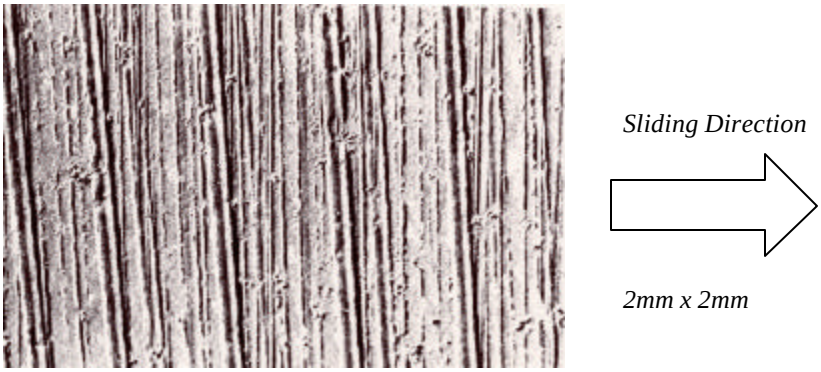

Figure 4.7, Location of AES Depth profiling on Sample 3

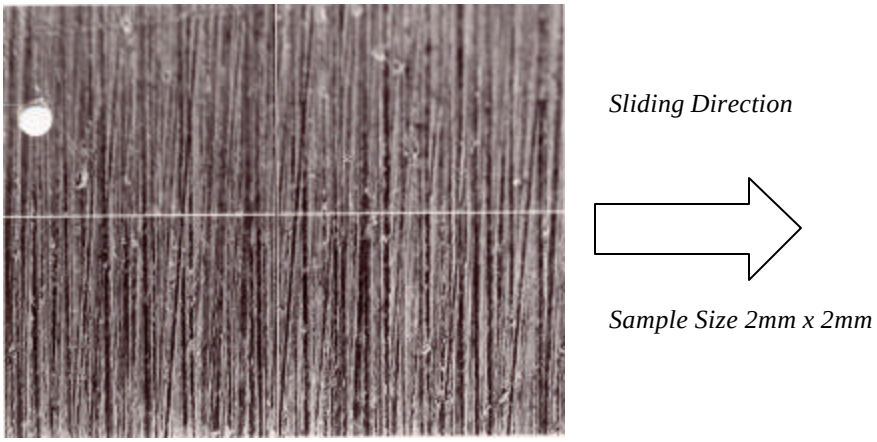

Figure 4.8, Location of AES Depth profiling on Sample 4

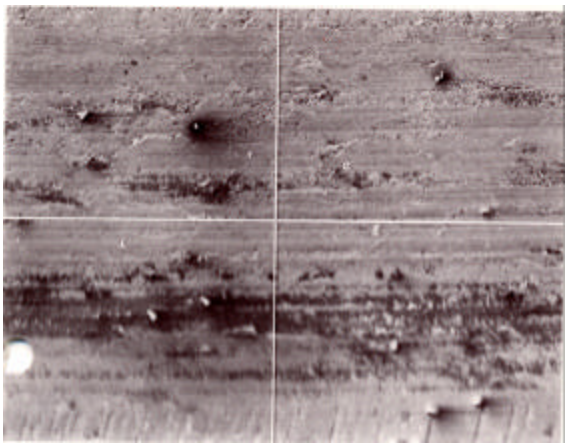

Figure 4.9, Location of AES Depth profiling on Sample 5

The machining marks are visible for all but the scuffed sample, which should not be confused for the wear marks. From the figures above it can be determined that the surface is actually polished and severe wear does not take place till scuffing.

4.3.1 Data Analysis:

Two methods will be used to analyze AES data, the first is depth profiles relative to intensity obtained from the AES, and the second is percentage concentration of these depth profiles. The intensities shown in the first set of data are converted into percentages by taking into account the Auger energy strength and concentration. The following graphs show results that were obtained after the AES tests were carried out on the samples and are in arbitrary units.

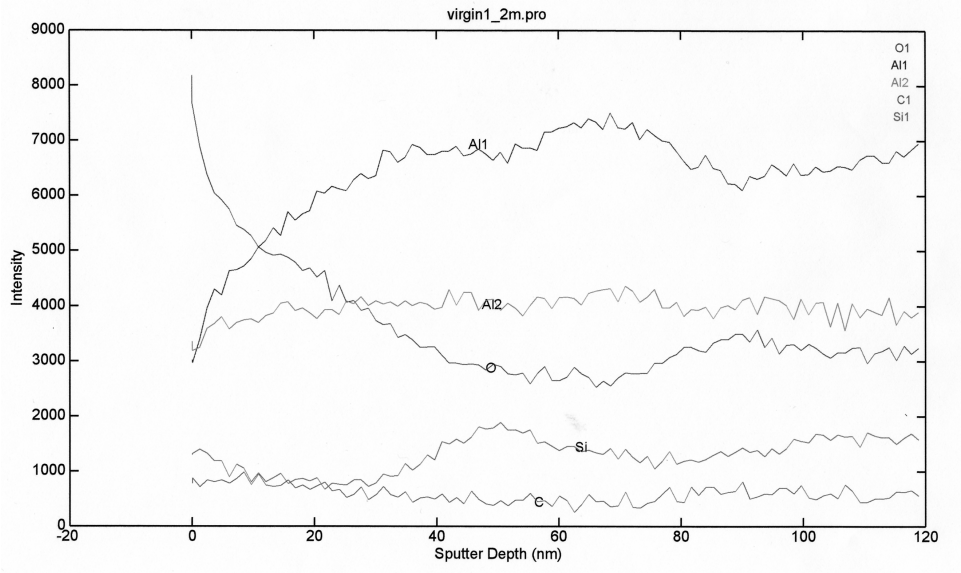

Figure 4.10, Depth profile of Sample 1.

From the graph it can be observed that there is substantial oxygen from oxidation of the surface. As we sputter into the surface the oxygen deteriorates relatively fast until about a depth of 10nm. The oxygen decreases at a

declining rate, until a depth of about 80nm where it increases but not significantly. The oxide layer initially covers the aluminum, but as we sputter into the sample, the aluminum increases to almost a stable amount. The silicon is initially low, but at a depth of about 30nm, it increases substantially, this is important because some of the later samples display different trend. There is minimum carbon on this sample. This depth profile is representative of the profiles of all the samples in their virgin states. As the samples are worn out we expect to see a change in both composition and concentration of the elements. We now progress to study the first worn sample that is followed the scuffing test protocol for a time duration of 0.25xT. Similar Auger profiles in different locations on the sample give similar results, indicating that the $0.5\mu m^2$ analysis area is sufficient for consistent data, but avoids the averaging effects as with Yoon (1999) and Sheiretov (1997) which used larger areas.

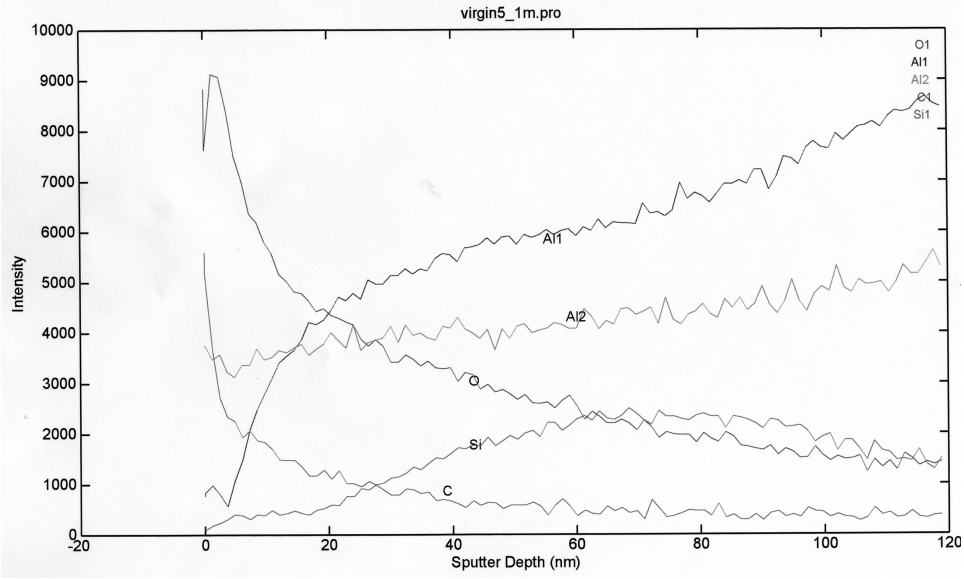

Figure 4.11, Depth profile of Sample 2.

Just like the virgin sample, this sample is initially covered with an oxide layer. The oxygen deteriorates almost at an exponential rate and keeps on decreasing for the rest of the profile. From the graph two different oxide slopes can be established, suggesting existence of two different oxides. There is a substantial amount of silicon, from a depth of about 20nm, which stabilizes to an expected level from the stoichiometric composition of the alloy. As for the aluminum, its trends are relatively constant and are comparable to that in the previous virgin sample. There is a substantial amount of carbon, mainly from the oil and carbonation from the air, however the carbon concentration reduces to an insignificant level at about 40nm. As the samples are subject to longer durations of wear, we would expect further change on their chemical composition.

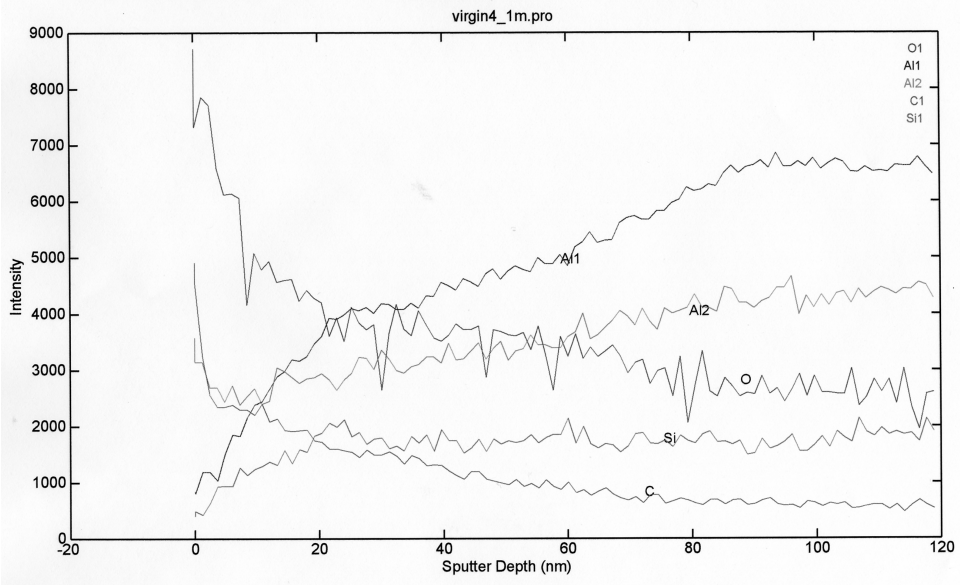

Figure 4.12, Depth profile of Sample 3.

In Figure 4.12, the oxygen deteriorates rapidly for the first 10nm, and then almost decreases linearly at a less rapid rate suggesting two different oxide layers as suggested in the quarter scuffed profile. Aluminum trends are similar to the ones previously seen suggesting that change in Al concentration does not play any part in scuffing due to change in chemical composition. As for the carbon, it is more prominent in this sample compared to the previous one; probably because it was run for twice the amount of time the previous samp le was run (the carbon is present until about 60nm). Silicon trends change on this sample, a lot more silicon can be seen at an early depth of 10nm, and is relatively constant in intensity for the rest of the depth.

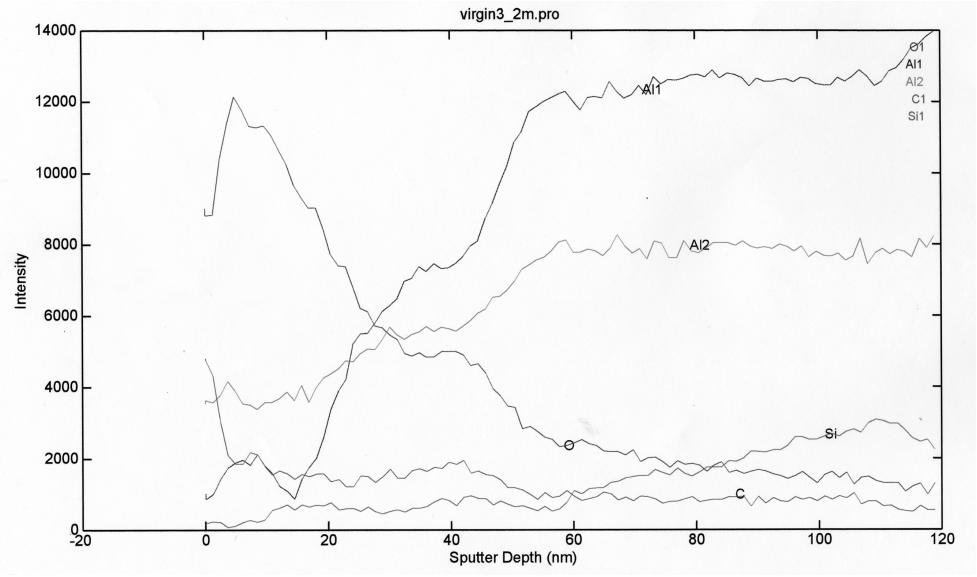

Figure 4.13, Depth profile of Sample 4.

For 0.75 x T sample we begin to see interesting trends, it almost signifies the turning point towards failure. Oxygen can be seen to a much deeper depth and can decreases less rapidly as compared to the previous graphs (virgin, 0.25xT, 0.5xT). The aluminum displays similar trends as previously seen. Carbon is almost at the same level previous sample (NB the scale is different on this graph, so intensity is displayed by half the amount). The most interesting trend is seen in the silicon; here the silicon is depleted up to a depth of about 60nm, which represents an important finding.

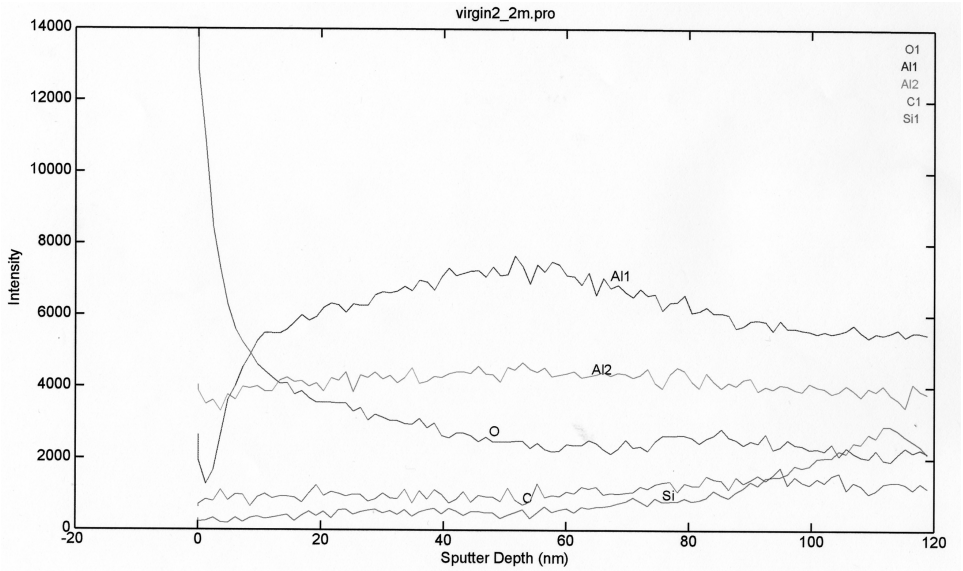

Figure 4.14, Depth profile of Sample 5.

This scuffed sample displays some essential trends needed for deducing a conclusion. The oxygen concentration decreases fast, probably the fastest rate so far, but then stabilizes to a relatively constants amount. Aluminum trends are similar to the previous samples. The carbon content is a lot less than the previous sample it is possible that the carbon being burned out due to the heat and pressure that is generated at the interface during scuffing. The most noticeable element is silicon; the silicon is depleted up to a depth of about 60nm and then begins to increase to an expected level.

In summary from depth the profile intensities, we have established some important trends from the analysis, however we need to study the percentage concentration of the elements from the depth profiling to substantiate the findings established in this section. An important output of the AES is the kinetic energy plot, which illustrates the energy bands used to detect the elements under investigation. Figure 4.16 summarizes the 5 different kinetic energy plots starting from Sample 2 (top left), Sample 1 (top right), Sample 5 (center left), Sample 4 (center right) and Sample 5 (bottom left). This figure shows the kinetic energy range of the survey.

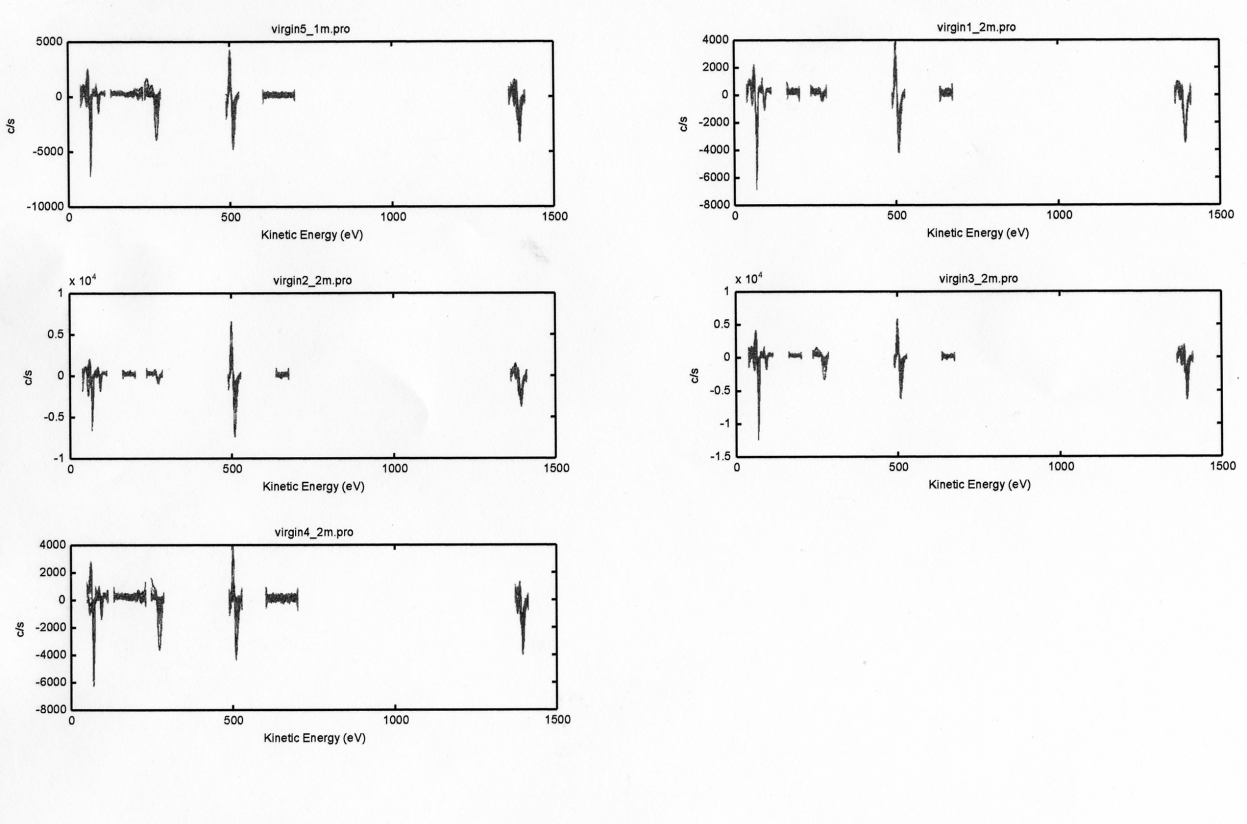

Figure 4.15, Summary of kinetic energies of AES depth profiles

We have studied the data obtained from the depth profile, now we look at the variation of concentration in percentage of each of the elements as we take a depth profile. We first start out with the virgin sample so as to establish a reference to which the worn samples will be compared.

The virgin sample initially displays low percentage of Silicon; this is due to the oxide layer that exists on the surface. However as sputtering continues and the oxide and carbon compounds on the surface and sub-surfaces are removed, the silicon percentage increases to an expected amount of ≈ 17%. Initially Oxygen reduces at a fast rate (steep gradient), after that it decreases from about 25nm at a different rate, this indicates the possibility of two different oxides existing within the sub-surfaces. The aluminum and carbon do not show any significant trends that support the findings of the intensity plots.

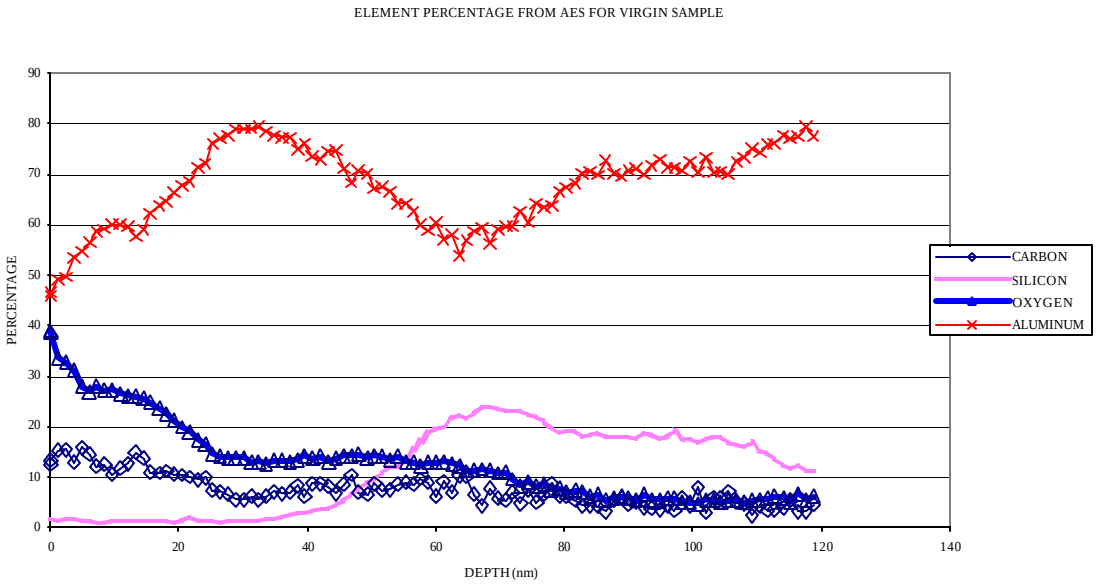

Figure 4.16, Percentage concentration of elements on Sample 1

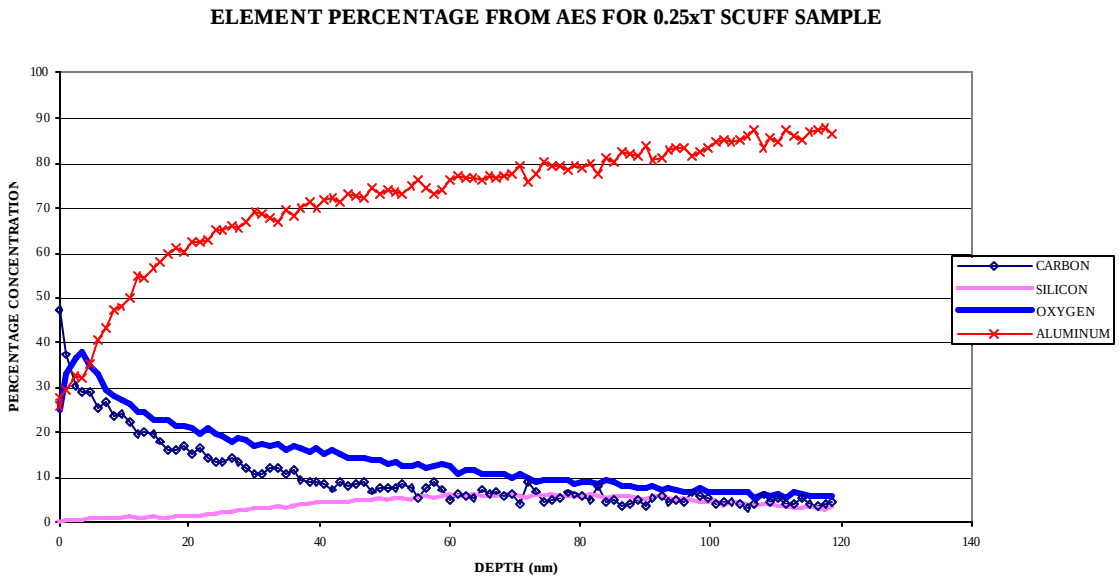

Figure 4.17, Percentage concentration of elements on Sample 2

The graph above shows the relative percentages of the elements that exist in the quarter time to scuffing sample. The essential finding is that the silicon concentration is depleted. The oxide in this sample also shows two distinct slopes suggesting the existence of different oxides in the sub-surfaces. The virgin sample has 76% Al whereas in this case the percentage of Al is higher than that due to a reduction in the Silicon concentration. The

0.5xT scuff sample shows similar results to those shown by the 0.25xT sample. These similarities indicate a steady state that has been reached and sustained as the wear cycle continues.

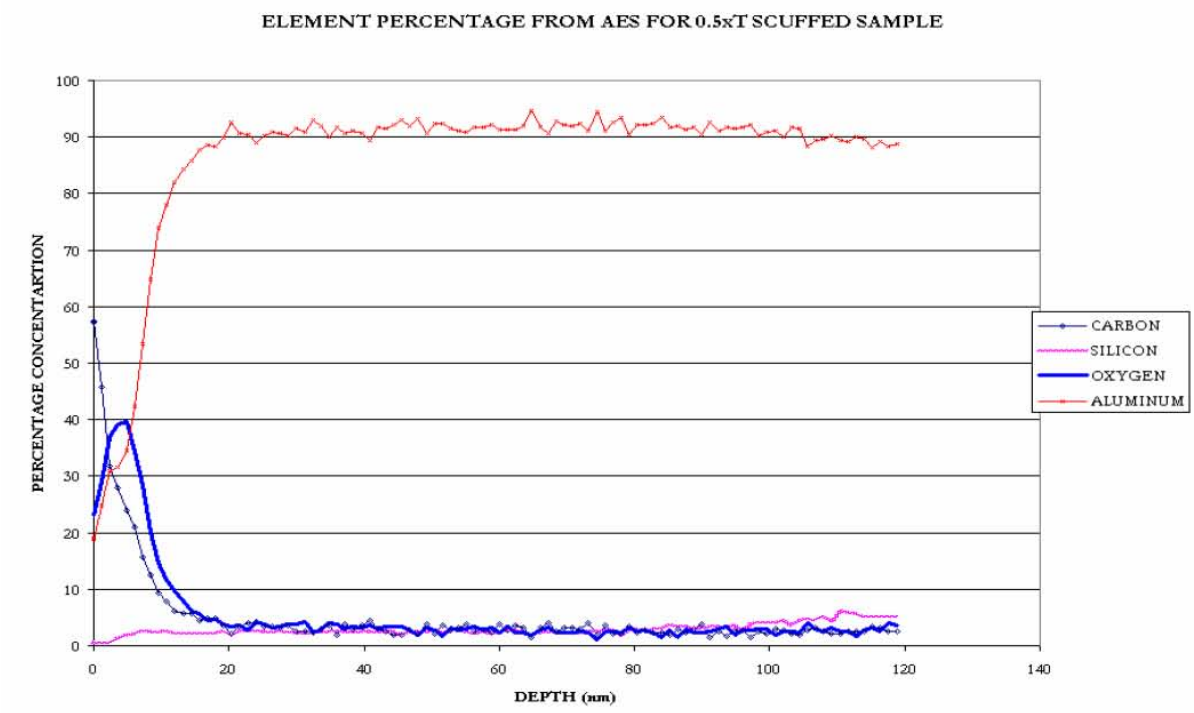

Figure 4.18, Percentage concentration of elements on Sample 3.

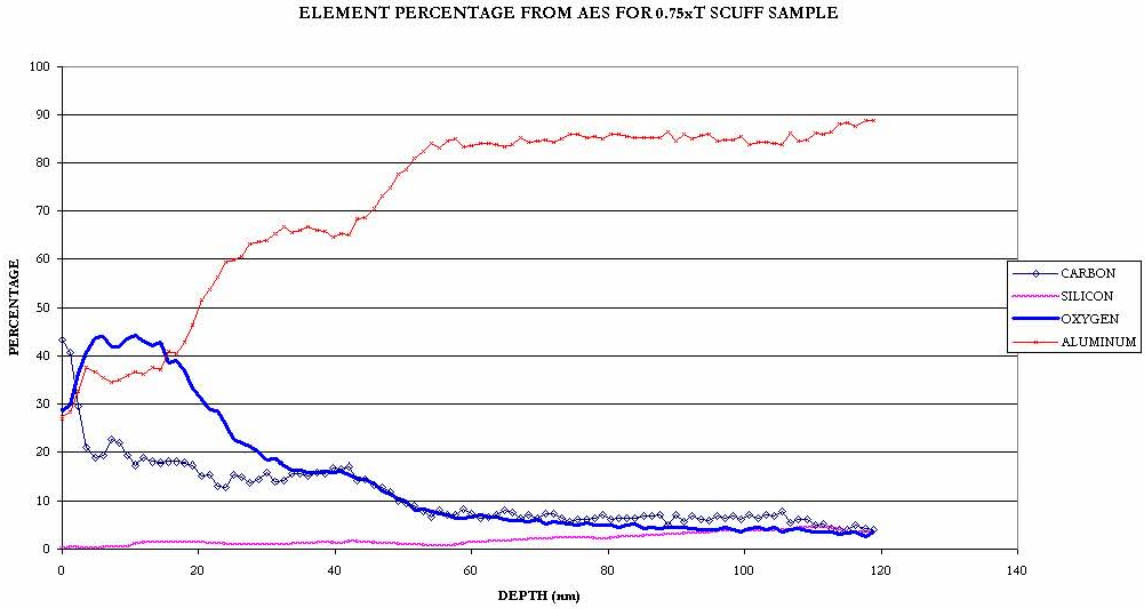

Figure 4.19, Percentage concentration of elements on Sample 4

In the 0.75xT sample, initially the percentage of oxygen is relatively high; this results in a low initial percentage of aluminum. It seems at this stage, the steady state reached in the previous two stages is absent. The surface is beginning to prepare for failure. This data is supported by the second AES experiment carried out on the same sample, showing similar trends The asperities are smoothened out at this stage as mentioned in chapter 3, this might be accompanied with plastic deformation, leading to a change in concentration of the oxide layers. Examining the scuffed sample the percentage of silicon has decreased drastically in the initial 100nm, after which it begins to increase.

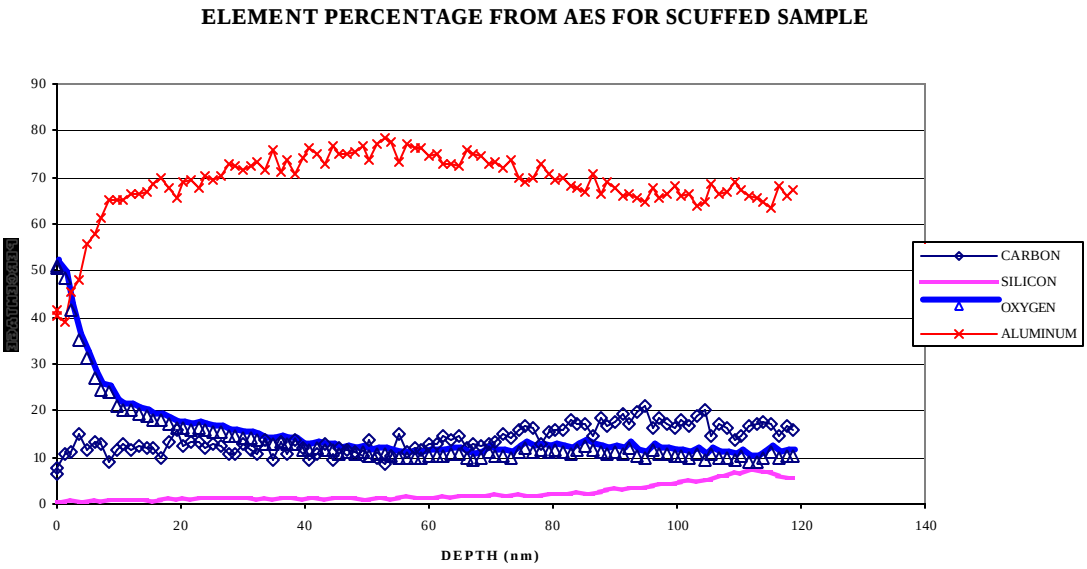

Figure 4.20, Percentage concentration of elements in Sample 5

Figure 4.20 above depicts that the concentration of silicon decreases drastically from its virgin state. To investigate the details of silicon depletion, we plot the silicon concentration of all five samples against depth. Figure 4.22 clearly illustrates a decrease in concentration of silicon at 0.25xT scuffing and keeps on decreasing till the sample scuffs. This indicates that the silicon is indeed depleted almost as soon as the wear process is initiated.

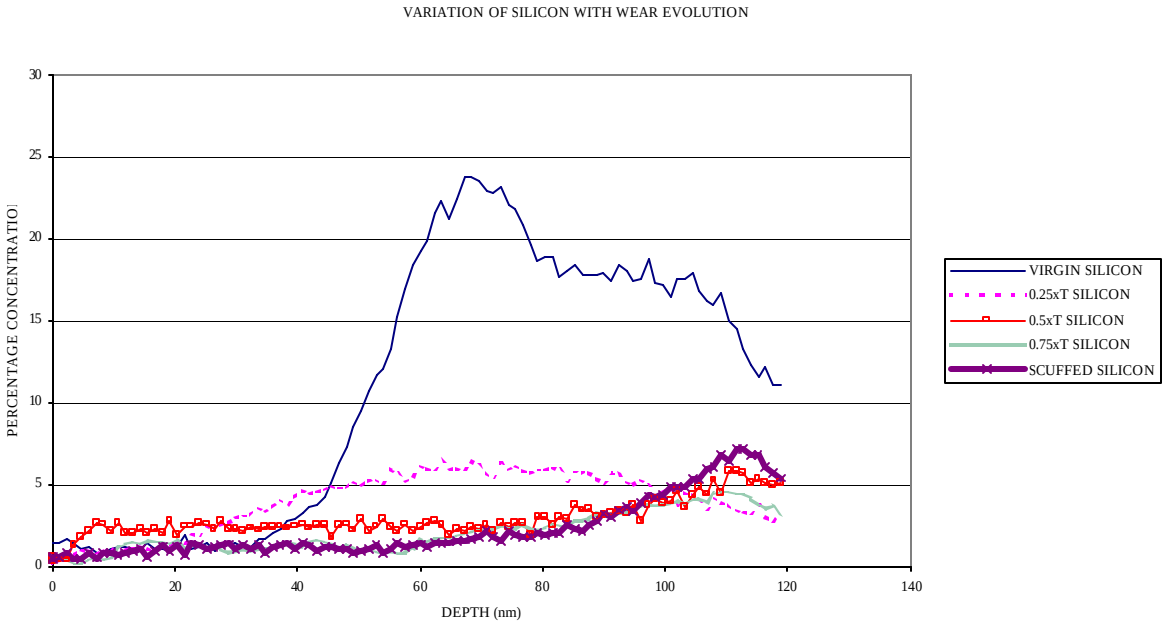

Figure 4.21, Variation of silicon concentration during the wear cycle up to a depth of 120nm

4.3.2 Conclusion from AES:

There exists a trend in the change of the thickness of oxide layers as the wear intensity changes, and the oxide graphs indicate the possible existence of at least two different oxides. The aluminum is relatively consistent from sample to sample; no noticeable change can be accounted for. Silicon displays an important trend, as we go through the different stages of wear intensity, the silicon content begins to get depleted. This is very important because silicon is added to the aluminum to increase the hardness of the alloy. A depletion of silicon could lead to a reduction of hardness, thus eventual failure. An example of this is the difference between Al-390PM-T6 (hardness 46HRB, 7% Silicon), and Al-390PM-T6 (hardness 56HRB, 17% Silicon). The data in this section also support progressive wear of the surface as described, the surface is almost at steady state between the 0.25xT and 0.5xT Scuff, it then begins to change toward scuffing at 0.75xT Scuff.

4.4 XPS Analysis:

Once the Auger experiments were performed, it was decided to use the XPS, to identify the compounds that are formed by the elements with the nanometer scale in mind. The following procedure is used to identify the different compounds in different layers; the samples are initially cut using a low speed diamond saw to a size compatible with an XPS specimen holder (7mm x 7mm). These samples are then ultrasonically cleaned in a pool of acetone, and rinsed with alcohol. The samples are then stored in clean containers ready for the XPS analysis. In the XPS, the samples are loaded into the analysis chamber and the experiment is carried out. The analysis area is $1mm^2$, while the raster size used is 2mm x 2mm, and a sputtering rate of approximately 3nm (based on Si sputtering rate) a minute is used to sputter the sample. A larger area of analysis (was used compared to the AES) so as to investigate the variability of data between a specific point analysis (AES) and an average area analysis (XPS). Initially a scan is

ran on the surface to identify the concentration of Al, Si, C and O. Then sputtering is carried out to a depth of 6nm, where another scan is carried out. Thereafter, an additional 9nm is sputtered to obtain a scan at a depth of 15nm. A final scan is taken at 60nm, which is achieved by sputtering an additional 45nm. This procedure is duplicated for all the samples. Below is a summary of the data collected and its analysis.

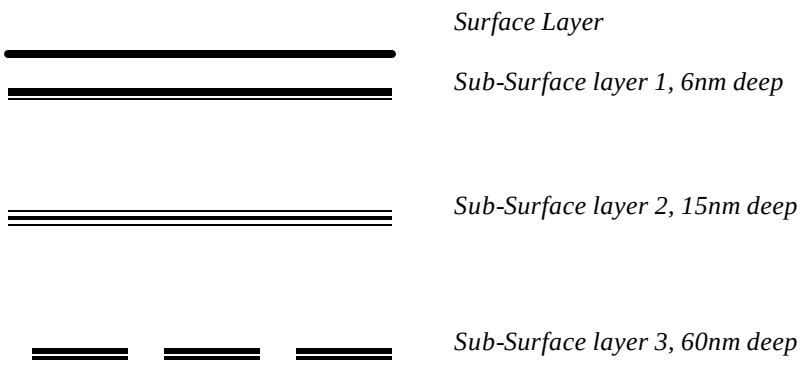

Figure 4.22, Profile studied by XPS

4.4.1 Experimental Data

The XPS gives output of data in two formats; first, a representation of the concentration of the elements detected, and second representation of the binding energy peaks of the elements. The first can be used to detect changes in concentration of elements from layer to layer (this would work similar to the AES depth profiles). The second set of data, representing the binding energy peaks, is used to determine the chemical composition of the layer under question. In this study we do collect the data for the chemical composition, however we only present an analysis of only one layer of the virgin sample. Further analysis of this data will be performed as a separate study. Below is an example of an XPS profile consisting of both data sets described earlier.

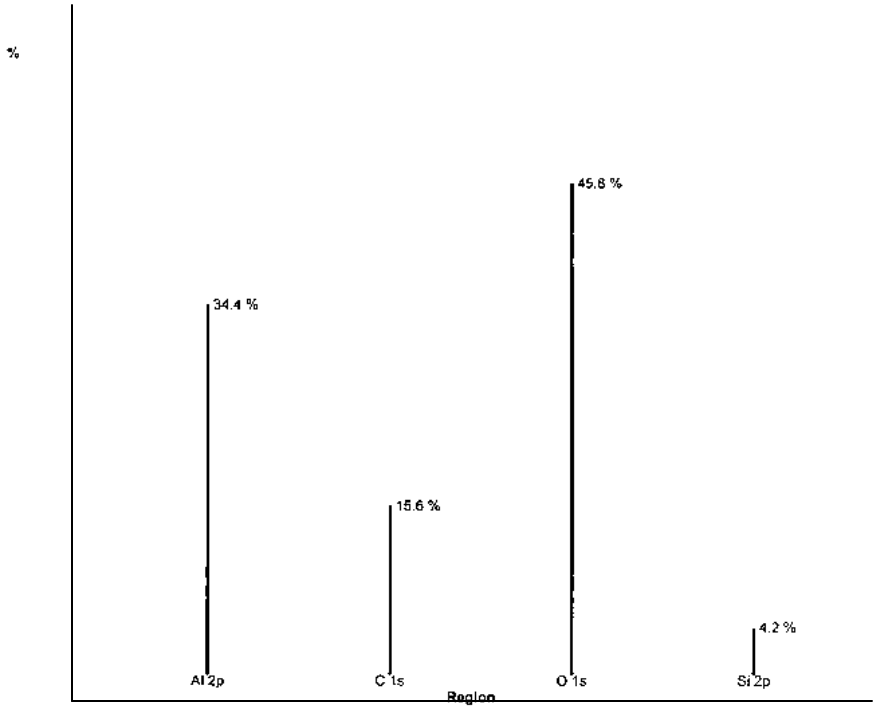

Figure 4.23, Percentage concentration of elements from XPS, Virgin sample, 6nm sub-layer.

The figure above depicts the percentage concentration four elements present in the virgin surface at a depth of 6nm from the surface. The four elements above were the only ones chosen because the chemical composition of the alloy contains Al, Si, while air oxidation and carbonation contribute the other two elements. The relative percentages are calculated by estimating the area under the binding energy curve of each of the elements. This method can also be used to estimate the ratio of one element to the other, and eventually help to deduce its chemical composition or valence state.

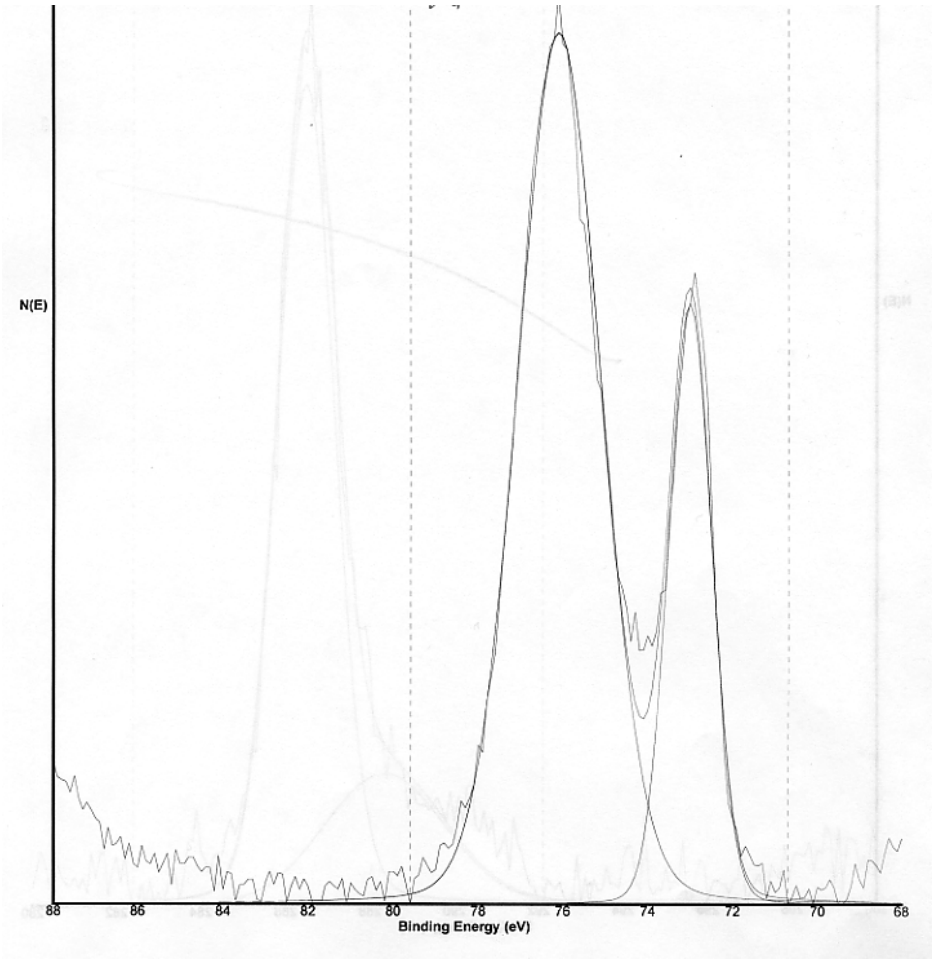

Figure 4.24, Binding energy of Al from XPS, virgin sample, 6nm sub-layer.

The figure above shows a binding energy graph of Al taken from a layer 6nm deep on the virgin surface. The graph shows the presence of two peaks, both in the aluminum binding energy range. One of the peaks represents pure aluminum, while the other represents an oxide of aluminum. The graph also shows that there is 74% pure aluminum and 26% aluminum oxide (the percentage is a function of area under the binding energy curve). Since there are several elements that are present in the sample, one has to study all the graphs of the main elements and then use all the data to deduce the composition of the layer. We now look at a graph of carbon from the same layer.

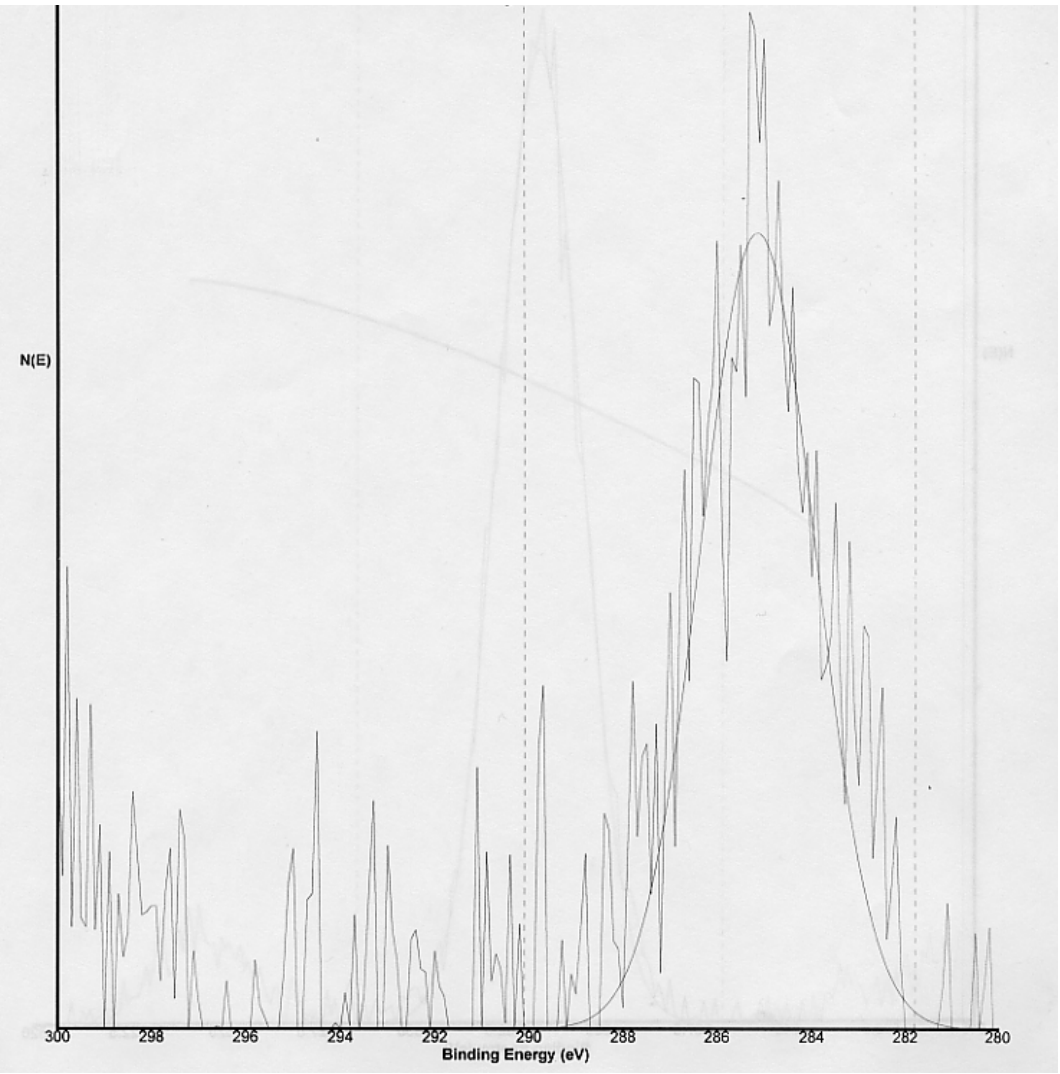

Figure 4.25, Binding energy of C from XPS, virgin sample, 6nm sub-layer.

Figure 4.25 has greater noise than the Al graph (Figure 4.24), the reason for this being that, the less the concentration of an element the smaller the peaks, and the harder it is to differentiate it from the noise. The carbon concentration is low, thus a well defined peak is not obtained, however, the graph above still reveals the state of carbon in the sample. From the binding energy, Carbon exists in some form of hydrocarbon state, and in order to identify the compound one needs to study the oxy gen curve.

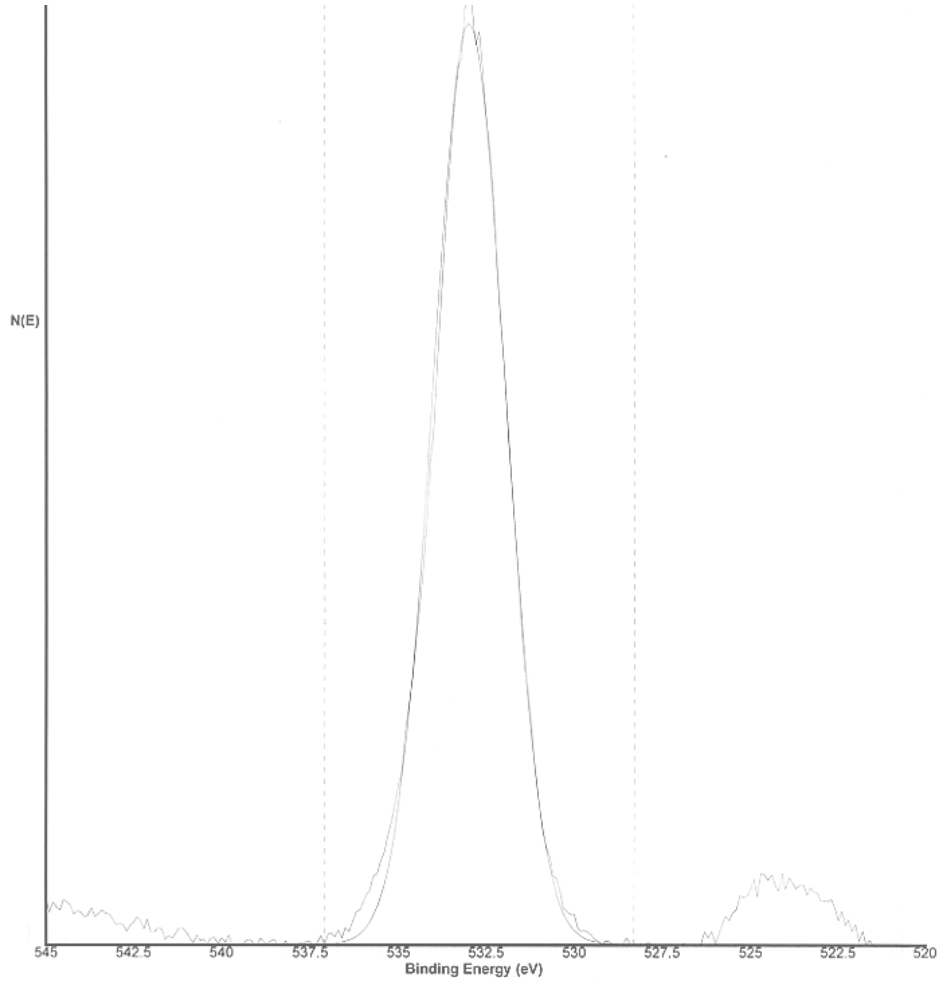

Figure 4.26, Binding energy of Oxygen from XPS.

Oxygen has two main peaks from the graph one at a binding energy of approximately 533eV, and the other at 524eV. From these energies, oxygen is present as silicon oxide and as a hydrocarbon. As described earlier, a standard universal chart is used as a reference to investigate the meaning of different binding energy peaks. Next we look at Silicon binding energy curve in Figure 4.27.

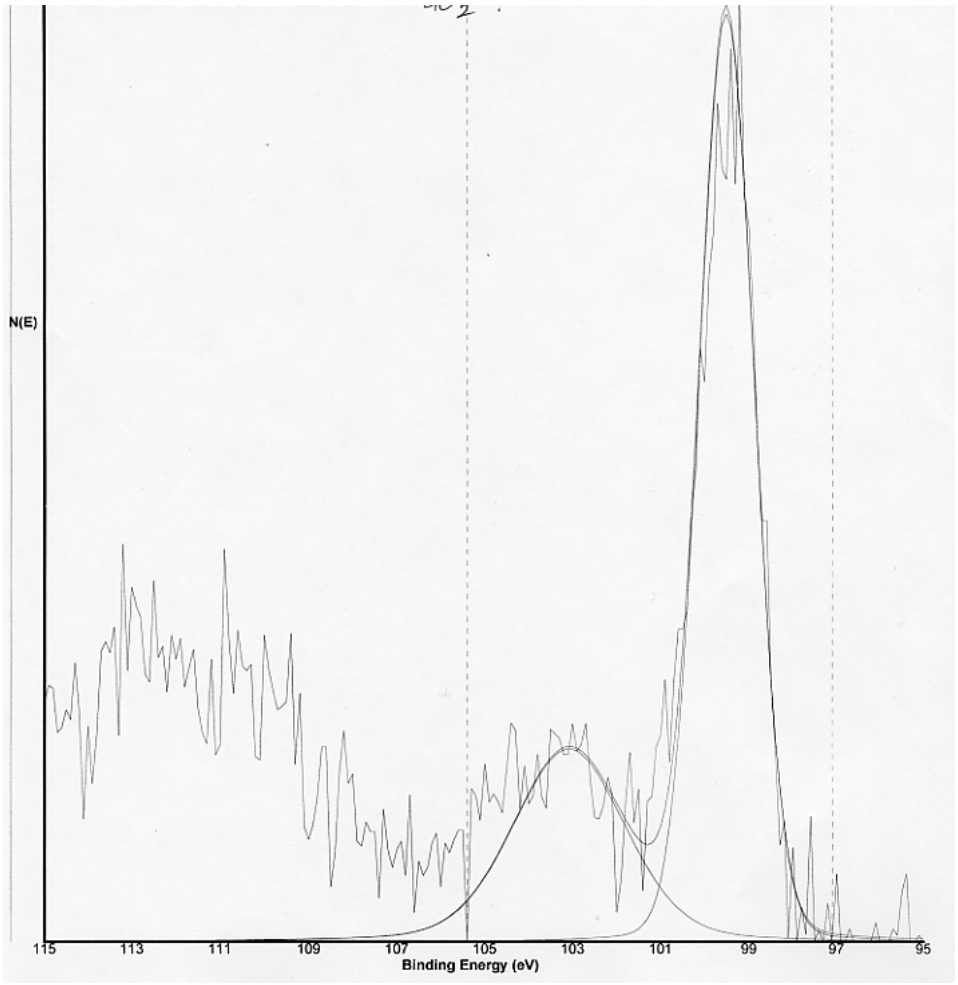

Figure 4.27, Binging energy of Si from XPS.

Silicon exists in two different forms at this layer. From the binding energies it is deduced that one of them is as pure silicon (69%) while the other is as silicon oxide (31%). Now that we have looked at both the concentration and compositions of each of the elements in the layer we can deduce the composition of this layer. From the XPS handbook (Joshi, 1986), it was deduced that there exists a hydrocarbon 6nm below the surface of the sample, there also exists an Aluminum-Silicon-Oxide which is proportional to about 17% aluminum and 30% silicon (this is not the exact concentration). Other than that, 70% of the silicon exists in its pure state, and approximately 50% of the Aluminum exists in its pure state. The carbon exists as a hydrocarbon and is mainly a contaminant. This same procedure can be repeated for all the samples and their layers.

4.4.2 Elemental Concentration Analysis:

In this section we summarize data dealing with the elemental concentration on each layer, and investigate whether this data supports the AES conclusions or not. To better understand the evolution of the surface, we plot the concentration of a specific element from disc to disc and plot it against depth. Since aluminum is most abundant in the alloy we initiate the analysis with that.

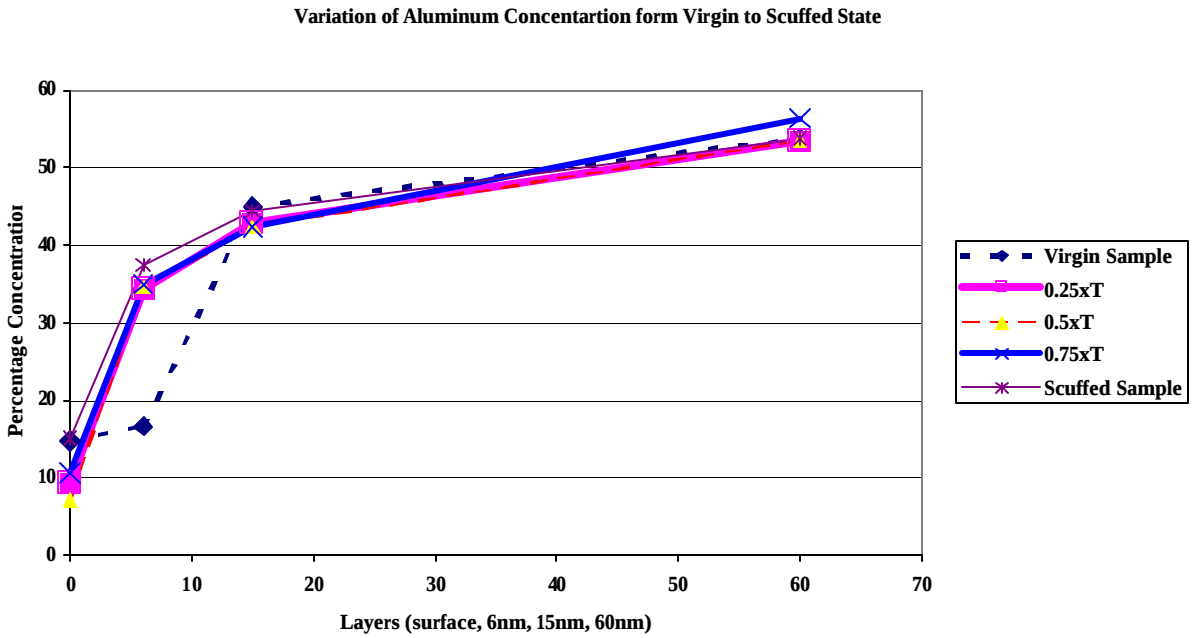

Figure 4.28, Variation of Al concentration from virgin to scuffed sample.

Aluminum exist in three states in the sub-surface layers of the Al-Si alloy, those are; as a compound Al-Si-O, as Aluminum oxide and as pure aluminum. From the figure above, the virgin sample shows some kind of coating up to a depth of 6nm that prevents full exposure of the Al, after this layer the Al concentration increases to an expected level. All the worn samples show no signs of the coating seen in the virgin sample, however, they do show similar results at a depth of 15nm and below. The trends here are similar to those seen in the Auger data earlier. Next we investigate results of Oxygen from XPS data.

The initial oxygen concentration is relatively high, this may be contributed to the oxidation of the surface from exposure to air. As one moves below the surface, differences are observed between the virgin and worn samples at a depth of 6nm. For the rest of the layers, the oxygen concentration does not vary much from sample to sample. The data suggests a decrease in the amount of Oxygen, as we sputter into a sample surface, which is expected because the surface is exposed to the atmosphere. The graph also suggests the existence of a large amount of oxygen at depths of over 30nm, which goes against AES results that showed substantially lower Oxygen at this depth. To get a better understanding of the layers we progress to study the Carbon data form XPS.

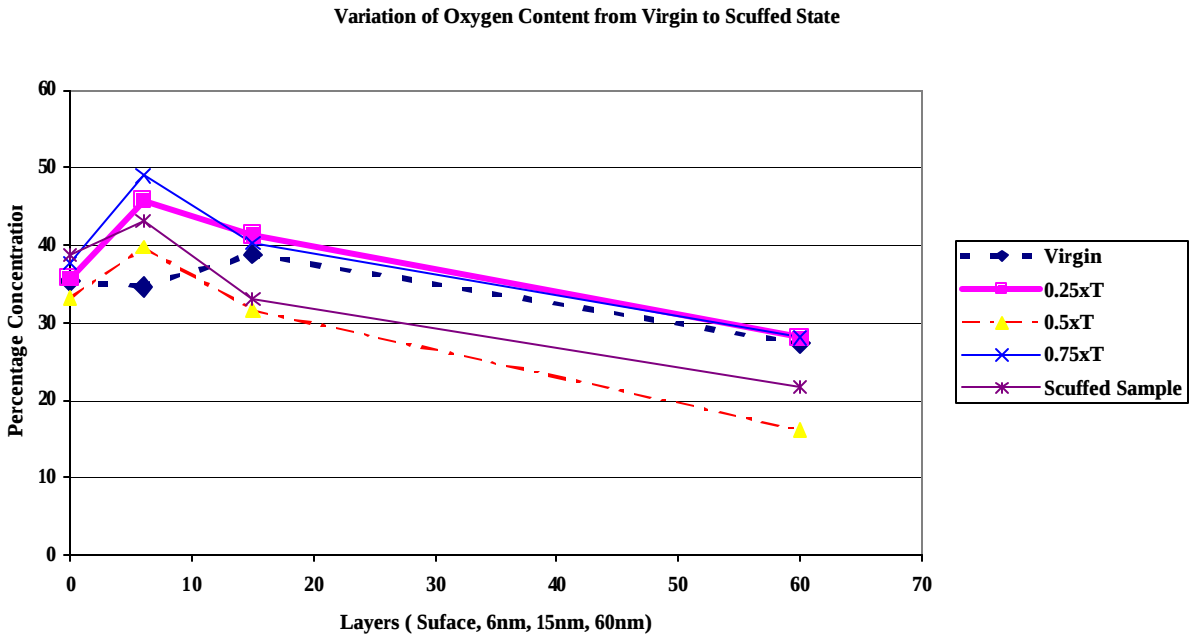

Figure 4.29, Variation of O concentration from virgin to scuffed sample.

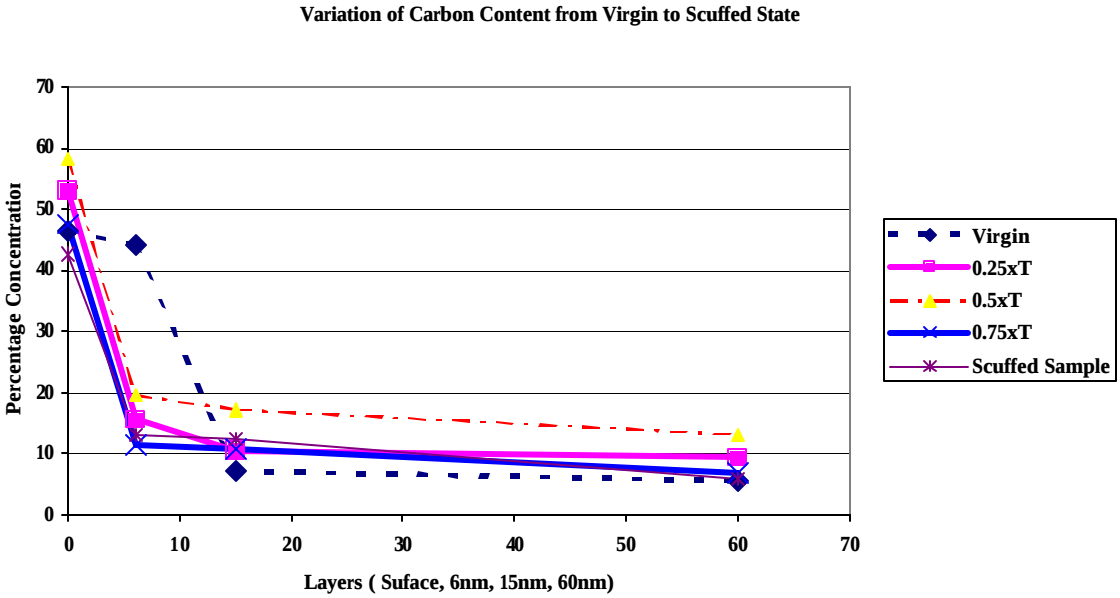

Figure 4.30, Variation of Carbon concentration from virgin to scuffed sample.

Carbon is primarily a contaminant from the atmosphere, which forms hydrocarbons on the surface and sub-surfaces of the sample. Carbon traces may also be found from wear areas that were exposed to both the lubricant and refrigerant. The surface of all the samples show high carbon concentrations, which is mainly attributed to the atmosphere. The virgin sample displays existence of approximately 40% carbon at 6nm depth, which is again

formed due to hydro-carbonation from the atmosphere. The presence of a high percentage of Carbon at 6nm depth, explains the low percentages of Al and O at this depth. The worn samples fail to detect the hydrocarbon layer probably because this layer was destroyed during wear. It should also be noted that the percentage of carbon in all XPS results is much higher than that seen from the Auger results. The final part of the puzzle is the Si data, which displayed the most important trends in AES experimentation.

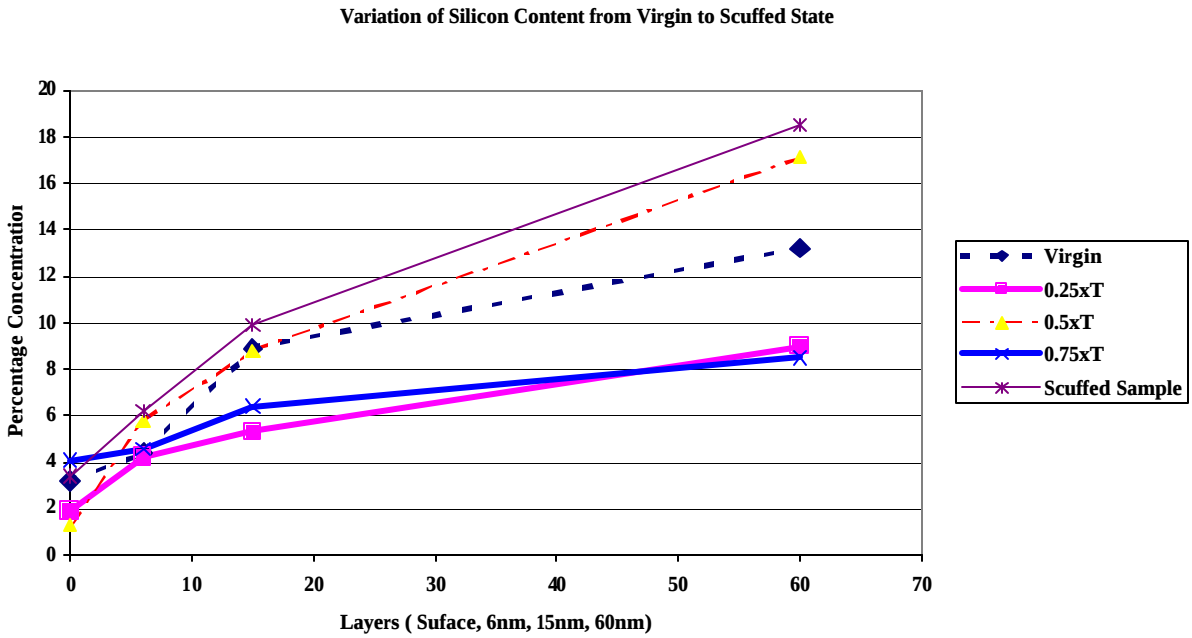

Figure 4.31, Variation of Silicon concentration from virgin to scuffed sample.

Figure 4.31 displays the percentage concentration of Silicon in various samples at various depths. Initially, the silicon is covered with the hydro-carbon layer, which when eliminated facilitates increase in the concentration of this element. The virgin graph lies at the center of the worn graphs, fenced by the 0.25xT and 0.75xT samp les at the bottom, and 0.5xT and Scuffed sample at the top. The data partly supports Silicon depletion and partly refutes it. This raises an important question, is the AES data false and the XPS data true of vice versa? This is explained in the following section.

4.5 AES Vs XPS Data:

Both the XPS and the AES data have been explained in detail in this chapter, it can be observed that the data do not agree with each other, does this mean that either is false? Both methods of chemical analysis are used extensively to analyze thin layers on different smooth samples, and have proven to be reliable, thus there must exist a special reason behind the variation in results. The reason for this is that the Al-390 surfaces are 'rough' compared to other surfaced which are commonly analyzed using the mentioned methods. In the AES, the sputter area is 700um x 700um, while the analysis area is $0.5um^2$, while in the XPS the sputter area is 2000um x 2000um and the analysis area is $1000000um^2$. This is where the discrepancy aris es, due to the small (point) analysis of the AES, the surface analyzed is almost flat (radius of asperities ~ 10 um), while the XPS analyzer overlooks a surface full of peaks and

valleys which have varying slopes. There have been many attempts to develop a general guide that dictated the variation of sputtering on curved surfaces (Makh, 1980), however none has been incorporated in the instrument to allow even sputtering. As a rough surfaces is sputtered, the summits are sputtered at a slower rate then the sloping areas (Barber, 1973), thus when the analyzer of the XPS takes data over a large area, it receives data which is not from an evenly sputtered area, and is more of an average. The reason mentioned above explains the high concentration of Oxygen and Carbon at a depth of 60nm, which is due to uneven sputtering. It can therefore be concluded that the AES data is more reliable than the XPS data for 'rough' surfaces at the nano-scale of analysis.

4.5.1 Conclusion:

An important finding from this study is that for surfaces as rough as the Aluminum disc, Auger analysis is more reliable than XPS at the nano-scale of analysis for reasons previously mentioned. This is essential because any analysis previously done using the XPS for such rough surfaces show an average result and not specific to an asperity. It can also be concluded there exists a trend in the change of the thickness oxide layers as the wear intensity changes, and the oxide graphs indicate the existence of at least two different oxides. The aluminum data is relatively consistent from sample to sample and from XPS to AES thus hinting that the surface Al is initially covered with aluminum oxides and hydrocarbons, but as these layers are sputtered into the expected concentration of Al is detected. Silicon displays an imperative trend, as an AL-390-T6 sample is worn out, the silicon concentration is depleted. Suggestions by Sheiretov and Yoon that that Silicon being harder is broken down into smaller fragments due to plastic deformation is supported here. A possible suggestion for the depletion is that the silicon after being broken down is plucked out of the alloy, which softens the surface. However this is a speculation, which needs further research to be validated. This concludes our study, the next chapter summarizes the main achievements of the study and suggests areas of further study in this field.

Chapter 5: Conclusions and Recommendations

5.1 Introductions

The evolution of a surface during a wear cycle is a complex and dynamic process, which includes mechanical, chemical and thermal interactions. With present day knowledge of this phenomenon, it is virtually impossible to come up with a set of equations or a fixed form solution that would model this process. However, we can come up with guidelines that govern this process and help us design better parts to resist wear better. In such complex processes, rarely does one end up with data that are perfectly distributed and that follow one certain pattern. That is not to say that a single conclusion cannot be reached, but, engineering judgment is required to come up with hypotheses that are derived from trends observed in experimental data. In this chapter of the thesis we summarize the present study, deduce conclusions from the study, and suggest future research areas.

5.1.1 Research Summary

There are two major goals of this study, first, to study the change in surface statistical parameters as the surface is worn and the relation to scuffing, second, to study the change in chemical composition of the surface and sub-surface layers of the sample and investigate its relation to scuffing.

The shoe-on-disc geometry, which is used to carry out the experiments of the steel shoe on aluminum disc is an approximate simulation of a swash-plate/shoe contact in an automotive swash-plate compressor. The High Pressure Tribometer (HPT) is used to simulate the wear conditions and the refrigerant used in this case is R410A with a POE lubricant. For experimentation five Al390-T6 samples are selected, making sure they have little surface damage in the form of scratchesfrom handling. The five samples are immersed in pools of Acetone, and ultrasonically cleaned for 10 minutes. They are then rinsed in alcohol and dried using a hot-air source. The samples are then placed in sealed containers to prevent contamination. Profilometer scans are run on the virgin samples after which ultrasonic cleaning is repeated. The five samples are then to be tested as follows; Sample 1, Virgin sample, no wear test, Sample 2 was worn in for a time corresponding to 0.25x T (T= time to scuff), Sample 3 was worn in for a time corresponding to 0.5x T, Sample 4 was worn in for a time corresponding to 0.75x T, and Sample 5 was run till it scuffed, the time taken to scuff (T) noted. The conditions for the sample in the HPT are as follows; Rotation Speed 1030RPM (2.4m/s), Load Step 20lbs, Disc Temperature 121°C, and Load Interval of 15 seconds. The samples are then ultrasonically cleaned as previously described and profilometer scans of the worn samples are taken. The data from profilometer scans are analyzed using MatLab and used to deduce the geometrical and statistical parameters. The samples are then cut into smaller sizes, ready for chemical analysis (prior to analysis they were ultrasonically cleaned again). The Dektak experiments consisted of radial short, radial long and circumferential profilometer scans on all 4 quadrants of each sample. These data were analyzed and plotted to deduce and support the suggested conclusions. As for the chemical analysis, the Auger Electron Spectrometer and X-Ray Spectrometer were used to analyze the samples at a nanometer scale. In the AES, depth profiles were carried out on the samples to a depth of approximately 120nm tracing Oxygen, Carbon, Aluminum and Silicon. In the XPS, four layers were studied at depths of 0nm, 6nm, 15nm and 60nm. The data were used to study the change in composition of the four elements previously mentioned. In general the study investigates trends during wear of the samples starting out at a larger

scale of analysis (millimeter) focusing down into a smaller scale (nanometer) of analysis. Below is a summary of the results form the study.

5.1.2 Conclusions from the Study

1. The study observes vital evidence that surface damage occurs soon after the sample test is initiated in the HPT by the presence of the primary wear scar on the quarter time to scuff sample. Sample 2 (quarter time to scuffing) shows development of a primary wear scar that occurs towards the inside of the overall wear track. This seems to indicated from the highest part of the crowned shoe and appears to be in the form of abrasive wear. In Sample 3 this wear track is still present, however the overall wear track becomes more defined at this stage. Sample 4 depicts a premonition that the sample would scuff and this will occur at the primary wear scar. Sample 5 shows that scuffing does occur at the primary wear scar, which is formed in the early stages of wear. The study thus concludes that a primary wear scar is formed during wear prior to 0.25xT scuffing which is the area where scuffing occurs. These observations were with macro and meso techniques, e.g. low magnification camera and microscope.

2. Based on the surface roughness measurements the following conclusions were deduced. The study data suggest that progressive wear occurs as virgin surface undergoes wear, the asperity peaks are smoothened till scuffing occurs. The profilometer scans and the statistical parameter graphs fully support this observation.

3. The skewness parameter suggests that the shape of the asperities prior to scuffing are similar to that of its virgin state. In that, as the surface undergoes the progressive wear described earlier, the asperities initially go from a positive skewness to a negative skewness due to the asperities being polished. As the as perities are further polished, the skewness decreases to a low point after which it increases towards a zero value.

4. The general trend exhibited by the radius of curvature of asperities is that, as the surface is worn out the radius of asperities increases. An explanation for this is that, as the asperities are polished, the flatter and wider parts of the asperities remain, thus providing a large radius of the asperities.

5. As for the areal density of asperities, the virgin samples have very consistent results as far as the initial density of asperities is concerned; as the surfaces are worn out the density increases in most cases. This is contrary to intuition, because as the radius of asperities increases it is expected that the density decreases. However, as the surfaces are smoothened out, the minor asperities that were not recorded get counted as asperities now thus suggesting an increase in density due to wear.

6. Results from profilometer scans in the radial direction conclude that profilometer scans taken in parallel to the machining marks are inconsistent and unreliable in nature. The topographical

data in line scans is usually most reliable if taken perpendicular to the machining marks, if the machining marks are prominent.

7. Next, the conclusions from the chemical analysis using AES and XPS as described. An important finding from this study is that for engineering surfaces as rough as ours, AES analysis is more reliable than XPS to study surface layers at the nanometer scale. The study also shows repeatability of AES results for areas as small as $0.5\mu m^2$, suggesting that studies can be carried out for rough surfaces at the nanometer scales.

8. The AES study suggests the existence of at least two different oxide layers from the surface into the bulk of the disc suggesting different material properties at these layers. It also suggests a nascent oxygen layer of a depth of approximately 40nm.

9. From the AES study we can also conclude that as a virgin sample is worn out, the silicon close to the surface (120nm) is depleted, this has been shown consistently by most of the AES results. This is very important because silicon is added to the aluminum to increase the hardness of the alloy. A depletion of silicon could lead to a reduction of hardness, thus eventual failure. An example of this is the difference between Al-390PM-T6 (hardness 46HRB, 7% Silicon), and Al-390PM-T6 (hardness 56HRB, 17% Silicon).

10. Aluminum composition changes mainly from pure to oxide state, while the concentration is barely affected.

11. A pure Al390-T6 sample does not have any carbon added to it, however, due to exposure to air; the surface of the sample gets contaminated with a carbon compound. For the virgin sample this goes to a depth of about 20nm, but for the worn samples this is deeper. The increase is depth is partly contributed by carbon from the oil during HPT experimentation.

5.2 Study Hypothesis

It is hypothesized that initially (0.25xT) the load is minimal, thus a primary scar is formed at the point of contact. Under abrasive wear as a mode of wear, as the load is increased this point of contact is elastically deformed allowing even contact pressure thus a wider wear scar (Samples 3 & 4). The wear mode now changes from abrasive to mild adhesive (polishing) wear. Eventually as more load is applied the surface eventually fails at the region of the primary wear. This hypothesis is supported by the optical images and the long wear scans. The nanometer layers that exist below a generally rough surface are different as the samples undergo tribological testing. This is the first study to investigate nano-scale layers on sub-surfaces of rough engineering samples.

5.2.1 Recommendations:

The study conducted has yielded some important conclusions, however these conclusions are just the foundations on which further investigation of the scuffing process is to be based on. From the tests in this study, data are now available to help construct an analytical model that can be used to predict and display the changes that occur on the surface of the sample as it is worn out. The analytical analysis is important to investigate that stage of wear

where maximum damage occurs and the possible causes of the primary wear scar. It is also suggested that the study on the radial long scans be continued to investigate the material transfer that occurs as a surface is worn out. If this is well understood, dimples or other features can be incorporated on the surface of the Al-390 alloy so as to increase its useful life.

From the chemical analysis, it is suggested that a study be carried out analyzing the XPS data to come up with the chemical compositions of the different layers within the sample. After this is done it is suggested that material properties of these layers are looked into, such as hardness, Young's modulus, thermal conductivity and others. Once this study has been carried out, one can predict the behavior of the layers during the wear process and can help compare this nano-scale study results to those carried out at the micron scale. This study can also shed light on previous theories such as that suggested by Yoon, 1999 that claim failure of the oxide layer is the main contributor to scuffing.

Based on this study there are discrepancies when chemical analysis is performed using small, say $0.5\mu m^2$ area for analysis, versus larger, say $0.5mm^2$ area due to the roughness of the sample. Further study of this effect is needed.

Finally further studies are needed to find out whether the nanometer range surface layers that exist below the rough surfaces are significant, since previous studies focused on micrometer range layers.

BIBLIOGRAPHY

AMTI (1991), *Model B; High Pressure Tribometer*, Advanced Mechanical Technology.

Archard, J.F. (1953), *Contact of Rubbing Surfaces and Flat Surfaces*, J. Appl. Phys., 24, pp.981-988.

Archard, J. F. (1980), *Wear Control Handbook*, ASME New York.

Arnell, R. D. et al. (1991), *Tribology, Principles and Design Applications*, Springer-Vergal, New York.

Auger, P. (1925), On the Secondary P-Radiation Produced in a Gas by X-rays, *Comptes Rendus*, 180, pp.65-68.

Barber, D. J, Frank F. C (1973), Graphical Method of Predicting How Two Dimensional Surfaces Deform, *Material Science*, 8, pp1030-1038.

Beesley, C., Eyre, T.S. (1976) Friction and Wear of Aluminum Alloys Containing Copper and Zinc, *Tribology International*, 9, pp 63-69.

Begelinger, A, deGee, A.W.J (1981) Failure of Thin Lubrication- The Effect of Running-In on Load Carrying Capacity of thin Film Lubricated Concentrated Contacts, *Journal of Lubrication Technology*, 103, pp.203-210.

Blok, H. (1940), Fundamental Mechanical Aspects of Boundary Lubrication, S.A.E.J., Vol. 46(2), pp. 54-68.

Bowden F.P; Tabor, D. (1950) *Friction and Lubrication of Solids, Part I*, Oxford University Press.

Burwell J.T (1957), Survey of Possible Wear Mechanisms, *Wear*, 1, pp.119-141.

Chang, C.C. (1975), General Formalism for Quantitative Auger Analysis, Surf ScL, 48, pp.9-21.

Chang, Y. W. (1992), Surface Diagnostic Techniques Commonly Used In Tribological Studies, American Chemical Society, Chapter 1.

Cameron, A. (1985), On a Generalized Theory of Scuffing, *Proc. 12th Leeds-Lyon Symposium on Tribology*, The Instisut National Des Science Aplliquees, Lyon, France, 3-6 September 1985, pp.3-9.

Cavatorta, M.P. (1998), Running-In and Scuffing in Aluminum/Steel Sliding Contacts, *Phd. Thesis*, Politecnico di Torino.

Childs, T.H.C (1998), The Mapping of Metallic Sliding Wear, *Proc. I. Mech. E., PartC.*, 202 (C6), p.379-395.

Childs, K.D. et al. (1995), *Handbook of Auger Electron Spectroscopy*, ed. by C.L. Hedberg, Physical Electronics Inc.

Cocks, M. (1952), Surface Oxide Films in Intermetallic Contacts, *Nature*, 170, p.213.

Czichos, H. (1974), Failure Criteria in Thin Film Lubrication, *The concept of Failure Surface, Tribology*, pp-14-20.

Davis, L.E. et al. (1976), Handbook of Auger Electron Spectroscopy, *Perkin-Elmer Corporation*, Physical Electronics Division, Eden Prairie.

Davis, B., Sheiretov, T.K., Cusano, C (1992) Tribological Evaluation of Contents Lubricated by Oil-Refrigerant Mixtures, *1992 International Compressor Engineering Conference at Purdue*, Purdue University, W. Lafayette, IN pp.477-487.

Dyson, A. (1975a), Scuffing- a Review, Part 1, *Tribology International*, 8 pp.117-125.

Greenwood, J.A., Williamson, B.P. (1966), Contact of Nominally Flat Surfaces, *Proc. R. Soc. London, Ser A*, 295, pp.300-319.

Harris, L.A. (1968a), Analysis of Materials by Electron-Excited Auger Electrons, *J Appl. Phys.*, 39, pp. 1419-1427.

Harris, L.A. (1968b), Some Observations of Surface Segregation by Auger Electron Emission, *J Appl. Phys.*, 39, pp. 1428-1431.

Hirst, W., Lanchaster, J.K (1956) surface Film Formation and metallic Wear, *Proc. Roy. Soc. London*, A259, pp.324-338.

Jahanmir, S, On the Wear Mechanism and Wear /equations, in Fundamentals of Tribology, N.P. Suh & N. Saka (eds), *The MIT Press, London*, pp.455-467.

Johnson, C. A., (1996), Mettalographic Sample Preparation, *Leco Corporation.*

Joshi, A. (1986), Auger Electron Spectroscopy, in Metals Handbook, 10, *American Society for Metals*, pp.550-567.

Kapoor, A., Williams J.A., Johnson, K.L. (1994), The Steady State Sliding of Rough Surfaces, *Wear*, 175, pp.81-92.

Kombalov, V.S. (1974), Effects of the Roughness of solids in Friction, *Nauka Press. Moscow.*

Lander, J.J. (1953), Auger Peaks in the Energy Spectra of Secondary Electrons from Various Materials, *Phys. Rev.*, 91, p.1382-1387.

Lee, S.C., Cheng, H.S (1991), Scuffing Theory Modeling and Experimental Correlations, *ASME Journal of Tribology*, 114, pp.237-334.

Makh, S. S, Smith R, Walls J. M. (1980), The Development of Surface Shape During Sputter Depth Profiling in Auger Electron Spectroscopy, *International Conference on Qualitative Surface Analysis*, pp.115-119.

McCool, J.I., Popgoshev, D. (1985), effect of Asperity Interaction on Scuffing, Proc. 12th Leeds-Lyon Symposium on Tribology, *The Institut National des Sciences Appliquees, Lyon, France*, 3-6 September 1985,pp.135-145.

Meyer, F., Vrakking, J.J. (1972), Quantitative Aspects of Auger Electron Spectroscopy, *Surf Sci.*, 33, p.271-294.

Moulder, J.F. et al. (1995), Handbook of X-ray Photoelectron Spectroscopy, *Physical Electronics*, Inc.

Ostvik, R., Christensen, H. (1968) changes in Surface Topography with Running-In, *Proc. Inst. Mech. Eng.*, London, 183, Part 3P, pp.57-66.

Palmberg, P.W. (1967), Secondary Emission Studies on Ge and Na-Covered Ge, *J Appl. Phys.*, 38, p.2137-2147.

Palmberg, P. W. et al. (1969), High Sensitivity Auger Electron Spectrometer, *Appl. Phys. Lett.*, 15, p.254-255.

Quinn, T.F.J. (199 1), Physical Analysis for Tribology, *Cambridge University Press*.

Quinn, T.F.J (1971), *Oxidation Wear* 18, pp.413-419

Rabinowicz, E., (1965), Friction and Wear of Materials, *John Wiley & Sons, Inc.*

Rabinowicz, E., (1995), Friction and Wear of Materials, II ed., *John Wiley & Sons, Inc.*

Spikes, H.A., Cameron, A (1974) A. (1974) Scuffing as a Desorption Process, *ASME Transactions*, 17. pp92-96.

Rabinowicz, E., Tabor, D. (1951), Metallic Transfer between Sliding Metals: an Autoradiographic Study, *Proc. Roy. Soc., 298, Series A*, pp.455-475.

Raveh, A., (1996), Surface Characterization of Thin Layers of Aluminum Oxide, *Surface and Coating Technologies*, 88, 103-111.

Razavizadeh, K., Eyre, T.S. (1982), Oxidative Wear of Aluminum Alloys: Part 11, *Wear*, 87, pp. 261-271.

Razavizadeh, K., Eyre, T.S. (1982), Oxidative Wear of Aluminum Alloys, *Wear*, 79, pp. 325-333.

Rice, S.L. & Solecki, R. (1979), Wear of Homogeneous and Composite Materials under Conditions of Repeated Normal and Sliding Impact, *AFOSR-TR*-79-1241.

Rice, S.L. (1979), The Role of Microstructure in the Impact Wear of Two Aluminum Alloys, *Wear*, 54, pp. 291-301.

Rice, S.L., Nowotny, H., Wayne, S.F. (1981), Characteristics of Metallic Subsurface Zones in Sliding and Impact Wear, *ASME Wear of Materials*, pp. 47-52.

Rigney, D.A., Chen, L.H., Naylor, M.G.S., Rosenfield, A.R. (1984), Wear Processes in Sliding Systems , *Wear*, 100, p. 195.

Rigney, D.A., Hirth, J.P. (1979), Plastic Deformation and Sliding Friction of Metals, *Wear*, 53, p. 354.

Saka, N. et al. (1977), Wear of Two-Phase Metals, *Wear*, 44, pp.77-86.

Sakmann, B.W. (1947), Geometrical and Metallurgical Changes in Steel Surfaces under Conditions of Boundary Lubrication, *J Appl. Mechs.*, pp. 43-52.

Sasada et al. (1979), in Proc. Int. Conf Wear Materials, Dearborn, MI, ASME, p.72.

Seah, N., Briggs, D. (eds) (1983), Practical Surface Analysis by XPS and Auger, *J. Wiley and Sons.*

Serpik, N.M., Kantor, M.M. (1965), Investigation on the Wear of Steel during Rubbing against Loose Powder Abrasive, *Friction and Wear in Machinery*, 19, p. 337.

Shchedrov, V.S. (1950), Analysis of Experimental Laws of Running-in on the Basis of General Equations of Wear Theory, in Friction and Wear of Machines, *Acad. Sci. USSR, Moscow- Leningrad*, pp.3-12.

Sheiretov, T.K. (1997), *Scuffing of Aluminum-Steel Contacts under Dry Sliding Conditions, P.h.D. Thesis*, University of Illinois at Urbana-Champaign.

Sheiretov, T.K., Yoon, H.K, Cusano, C. (1998a), Scuffing under Dry Sliding Conditions. Part 1: Experimental Studies, *STLE Tribology Transactions*, Vol. 41 (4), pp. 435-446.

Sheiretov, T.K, Yoon, H.K, Cusano, C. (1998b), Scuffing under Dry Sliding Conditions. Part 11: Theoretical Studies, *STLE Tribology Transactions*, Vol 41 (4), pp. 447-458.

Soda, N. (1977), Wear of some F.C.C. Metals during Un-lubricated Sliding. Part IV: Effects of Atmospheric Pressure on Wear, *Wear*, 43, pp. 165-174.

Somi Reddy, A., Pramila Bai, B.N., Murthy, K.S.S., and Biswas, S.K. (1995), Mechanism of Seizure of Aluminum-Silicon Alloys Dry Sliding Against Steel, *Wear*, 183, pp. 658-667.

Somi Reddy, A., Pramila Bai, B.N., Murthy, K.S.S., Biswas, S.K. (1994),Wear and Seizure of Binary Al-Si Alloys, *Wear*, 171, pp. 115-127.

Somi Reddy, A., Pramila Bai, B.N., Murthy, K.S.S., Biswas, S.K. (1995), Mechanism of Seizure of Aluminum-Silicon Alloys Dry Sliding against Steel, *Wear*, 183, pp. 658-667.

Spikes, H.A., Cameron, A. (1974), Scuffing as a Desorption Process - an Explanation of the Borsoff Effect, *ASLE Transactions*, 17, pp. 92-96.

Sreenath, A.V., Raman, N. (1976), Running-In Wear of a Compression Ignition engine. Factors Influencing Conformance between Cylinder Liner and Piston Rings, *Wear*, 38, pp. 271-289.

Subramanian, C. (1992), Some Considerations towards the Design of a wear Resistant Aluminum Alloy, *Wear*, 155, pp. 193-205.

Suh, N.P. (1977a), Microstructural Effects in Wear of Metals, in Fundamental Aspects of Structural Alloy Design, *R.I. Jaffe & B.A. Wilcox (eds.), Plenum Press, New York*, pp.565-595.

Suh, N.P. (1977b), Scientific and Technological Problems in Erosive Wear, *Institute on Scientific Problems relevant to Coal Utilization*, West Virginia University.

Suh, N.P. (1977c), An Overview of the Delamination Theory of Wear, *Wear*, 44, pp. 1- 16.

Sullivan J.L. (1987), The Role of Oxides in the Protection of Tribological. Surfaces, Proc. 1. Mech. E., *Tribology Friction Lubrication and Wear Fifty year on I Mech. E*, p.293.

Swanson, P.A., Ives, L.K., Whintenton, E.P., Peterson, M.B. (1987), Proc. ASME Wear of Materials Conference, *ASME, New York*, p. 49.

Tallian, T.E. (1967), On Competing Failure Modes in Rolling Contact, *ASLE Transactions*, 10, pp. 418-439.

Tharp, L.N., Scheibner, E.J. (1967), Energy Spectra of Inelastically Scattered Electrons and Leed Studies of Tungsten, *J Appl. Phys.*, 38, pp.3320-3330.

Yoon, H.K. (1999), Scuffing Under Starved Lubrication Conditions, *PhD. Thesis*, University of Illinois at Urbana-Champaign.

APPENDIX 1

A-1 Material Research: Summary of Cavatorta (1998)

A-1.1 Introduction

Presented here is a summary of tests carried out under similar conditions and test protocol, which led to the selection of materials, lubricants, refrigerant and experimental conditions for experimentation in this study. Various aluminum alloys were tested under the same environmental and operating conditions in order to compare their wear resistance or scuffing. The result show that the lowest wear rate was obtained with the 390die cast alloy (largest amount of Si content and highest hardness). It was also observed that adding Cu and Bi in certain proportions provides better wear results. Silicon is important because the composite SiC-Al provides high resistance to wear however increased percentages of Si led to more wear due to rougher and harder surfaces.

A-1.2 Effect of Silicon:

High wear rates at lower Si content are attributed to lower hardness of these alloys, while increased wear rates at high Si content are due to reduction in their ductility and fracture toughness. The optimum content of Si if approximately 17%. From the tests, two wear regimes were observed. The first, mild wear, most dominant one, characterized by small wear particles (<5µm). The second, is severe wear, this kind of wear is characterized by wear particles of the size >15µm. Other materials added to the alloys are; Zinc, Magnesium, Copper, Bismuth and Iron. There are two general requirements to effective boundary lubrication:

- The lubricant should be able to form protective films on a bare aluminum surface.
- The lubricant should be able to form a protective film on aluminum oxide surfaces.

Tables 1 &2 show composition and testing results of various aluminum alloys under different conditions. Table 3 shows the different tests conditions that were used. SEM and X-ray photoelectric spectroscopy were used to study and identify the chemical compounds formed on and beneath the surfaces of the alloys. Tables 4 &5 show results of tests of these materials.

A-1.3 Results:

From wear results it was observed that Ester/R134a mixture consistently provided better protection of the aluminum disc specimen compared to the PAG/R 134a mixture. HV3 and 356 have the same Si content, however HV3 provided better wear results, this is mainly due to the higher Cu and Bi content. During the experiment it was also observed that material transfer took place in the form of particle agglomeration at the inlet of the sliding contact (steel pin), from the aluminum alloy. This indicated that the geometry of the contact has a significant effect on the wear process.

Both 39OPM-T61 and 39ODC-T6 were tested with different initial surface roughness; the results are given in table 6. It can be concluded from these results that surfaces with lower roughness provided lower wear.

Table 1, Materials designation and tests conducted

Material Designation and Tests Conducted

Material Designation	Treatment	Fabrication	Hardness HRB	Test Conditions Designated in Table 3																
				A	B	C	D	E	F	G	H	I	J	K	L	M	N	O	P	Q	R
HV3-T6	T6	Extrusion	46	2		2															
HV3-T4	T4	Extrusion	44	2		2															
HV4-T61	T61	Squeeze Cast	51	2		2															
C278-T4	T4	Extrusion	47	2		2															
6061-T61	T61	Extrusion	48	2		2															
2024-T351	T351	Extrusion	58	2		2															
390DC-T6	T6	Die Cast	74	2		2															
390PM-T61	T61	Permanent Mold	56	3	2	2	2	2	2	2	2	3	2		2	2	2	2	2	2	4
356DC-NT	Not Treated	Die Cast	46	2		2															
356PM-T61	T61	Permanent Mold	46	2		2															
356CM-T61	T61	Coupon Mold	49	3	2	3	2	2	2	2	2	3	2	2	2	2	2	2	2	2	3
356CM-NT	Not Treated	Coupon Mold	38	2		3															
356CM-AN	Anodizing	Coupon Mold	49	2		2															
356CM-HC	‡Hardcoat®	Coupon Mold	600 HV											2							
356CM-NF	‡Nituff®	Coupon Mold	600 HV											2							
SiC-Al		Die Cast	41											2							
‡ Hardcoat® and Nituff® are proprietary hard anodizing processes																					

Table 2, Chemical composition of Al alloys tested

Chemical Composition of the Aluminum Alloys Tested

Alloy	Alloying Elements, % by Weight										
	Si	Fe	Cu	Mn	Mg	Cr	Ni	Zn	Bi	Pb	Ti
356	6.5-7.5	0.6	0.25	0.35	0.25-0.45	-	-	0.35	-	-	0.25
390	16-18.5	1.0	3.0-4.0	0.5	0.4-1.0	-	-	1.0	-	-	0.25
HV3	6.5-12	0.20	2.0-5.0	0.15	-	-	-	0.15	1.0-5.0	-	0.20
HV4	11-13.5	1.0	2.0-5.0	0.50	-	-	1.5-2.5	0.15	3.0-6.0	-	0.20
C278	11-13.5	1.0	0.5-1.3	-	0.8-1.3	0.10	0.5-1.3	0.25	0.50	0.50	-
2024	0.50	0.50	3.8-4.9	0.3-0.9	1.2-1.8	0.10	-	0.25	-	-	0.15
6061	0.4-0.83	0.70	0.15-0.4	0.15	0.8-1.2	0.04-0.35	-	0.25	-	-	0.15

Table 3, Tests Conditions

Test Conditions

Condition	Environment	Lubricant	L/R Viscosity cS	Env. Pressure MPa (psig)	Env. Temp. °C (°F)	Contact Load N (lbf)	Cont. Pressure MPa (ksi)
A	R134a	Ester 1	4.83	0.86 (125)	38 (100)	111 (25)	322 (46.7)
B	R134a	Ester 2	2.40	0.86 (125)	38 (100)	111 (25)	322 (46.7)
C	R134a	PAG 1	8.04	0.86 (125)	38 (100)	111 (25)	322 (46.7)
D	R134a	PAG 2	7.03	0.86 (125)	38 (100)	111 (25)	322 (46.7)
E	R22	Alkylbenzene	4.98	0.86 (125)	38 (100)	111 (25)	322 (46.7)
F	R22	Mineral Oil	4.98	0.86 (125)	38 (100)	111 (25)	322 (46.7)
G	R407C	Ester 1	10.67	0.86 (125)	38 (100)	111 (25)	322 (46.7)
H	R410A	Ester 1	13.35	0.86 (125)	38 (100)	111 (25)	322 (46.7)
I	R134a	Ester 1	3.32	0.17 (25)	121 (250)	111 (25)	322 (46.7)
J	R134a	PAG 1	6.62	0.17 (25)	121 (250)	111 (25)	322 (46.7)
K	R134a	Ester 1	5.73	0.86 (125)	38 (100)	667 (150)	1929 (280)
L	R407C	Ester 1	11.40	0.86 (125)	38 (100)	667 (150)	1929 (280)
M	R410A	Ester 1	16.10	0.86 (125)	38 (100)	667 (150)	1929 (280)
N	R407C	Alkylbenzene	14.05	0.86 (125)	38 (100)	111 (25)	322 (46.7)
O	R407C	Mineral Oil	7.97	0.86 (125)	38 (100)	111 (25)	322 (46.7)
P	R410A	Alkylbenzene	15.3	0.86 (125)	38 (100)	111 (25)	322 (46.7)
Q	R410A	Mineral Oil	9.36	0.86 (125)	38 (100)	111 (25)	322 (46.7)
R	Air	Ester 1	23.15	0.0 (0.0)	38 (100)	111 (25)	322 (46.7)

Table 4, Results of Al 356 under various test conditions

- Results for 390-T61 Permanent Mold Aluminum Alloy Tested under Various Conditions

Condition	Average Friction	Disc Wear Depth μm	Pin Wear Scar mm	Contact Resistance Ω	Wear Scar Roughness μm Ra	Roughness Before Test μm Ra	L/R Viscosity cS	Amount of Material Transfer†
A	0.128	0.86	0.23	0.37	0.225	0.160	4.83	None
B	0.139	1.58	0.26	8.70	0.262	0.165	2.40	None
C	0.140	1.82	.018	2.00	0.160	0.170	8.04	None
D	0.166	1.80	0.19	11.3	0.141	0.165	7.03	None
E	0.116	0.97	0.20	8.94	0.117	0.113	4.98	None
F	0.136	1.03	0.23	8.96	0.136	0.200	4.98	None
G	0.116	0.88	0.20	0.16	0.165	0.116	10.67	None
H	0.120	0.74	0.21	$3.9x\ 10^{-3}$	0.159	0.178	13.35	None
I	0.096	1.25	0.34	5.00	0.180	0.146	3.32	None
J	0.134	1.42	0.36	6.22	0.213	0.190	6.62	None
N	0.122	1.09	0.20	7.20	0.089	0.191	14.05	None
O	0.147	0.78	0.22	2.96	0.092	0.215	7.97	None
P	0.102	0.96	0.21	4.94	0.124	0.127	15.3	None
Q	0.100	1.25	0.20	3.41	0.118	0.199	9.36	None
R	0.092	1.20	0.28	10.7	0.165	0.216	23.15	None

Table 5, Results of Al-390 under various test conditions

-Results for 390-T61 Permanent Mold Aluminum Alloy Tested under Various Conditions

Condition	Average Friction	Disc Wear Depth μm	Pin Wear Scar mm	Contact Resistance Ω	Wear Scar Roughness μm Ra	Roughness Before Test μm Ra	L/R Viscosity cS	Amount of Material Transfer†
A	0.128	0.86	0.23	0.37	0.225	0.160	4.83	None
B	0.139	1.58	0.26	8.70	0.262	0.165	2.40	None
C	0.140	1.82	.018	2.00	0.160	0.170	8.04	None
D	0.166	1.80	0.19	11.3	0.141	0.165	7.03	None
E	0.116	0.97	0.20	8.94	0.117	0.113	4.98	None
F	0.136	1.03	0.23	8.96	0.136	0.200	4.98	None
G	0.116	0.88	0.20	0.16	0.165	0.116	10.67	None
H	0.120	0.74	0.21	$3.9x\ 10^{-3}$	0.159	0.178	13.35	None
I	0.096	1.25	0.34	5.00	0.180	0.146	3.32	None
J	0.134	1.42	0.36	6.22	0.213	0.190	6.62	None
N	0.122	1.09	0.20	7.20	0.089	0.191	14.05	None
O	0.147	0.78	0.22	2.96	0.092	0.215	7.97	None
P	0.102	0.96	0.21	4.94	0.124	0.127	15.3	None
Q	0.100	1.25	0.20	3.41	0.118	0.199	9.36	None
R	0.092	1.20	0.28	10.7	0.165	0.216	23.15	None

Table 6, Effect of test conditions on roughness of Al-390

Effect of the Initial Disc Surface Roughness on 390 Alloy

Alloy	Condition	Initial Roughness μm	Wear Scar Roughness μm Ra	Average Friction	Disc Wear Depth μm	Pin Wear Scar mm	Contact Resistance Ω	Amount of Material Transfer†
390DC-T6	A	0.258±0.009	0.129	0.130	0.681±0.074	0.25	11.7	None
390DC-T6	A	0.026±0.009	0.080	0.151	0.302±0.099	0.25	4.27	None
390DC-T6	C	0.259±0.015	0.010	0.132	1.11±0.12	0.16	3.17	None
390DC-T6	C	0.019±0.001	0.075	0.133	1.20±0.46	0.24	5.60	Medium
390PM-T61	A	0.191±0.028	0.225	0.128	0.859±0.017	0.23	0.37	None
390PM-T61	A	0.039±0.011	0.209	0.137	0.696±0.198	0.29	5.60	None

A-1.4 Conclusion:

Friction and wear tests of various aluminum alloys, aluminum composites and some surface treated aluminum alloys lubricated with different LJR mixtures were conducted using the HPT. These materials were slid against 1018 carburized steel pins. The 1JR mixtures tested included mineral and alkyl-benzene lubricants with R22, R407C and R410A, an ester lubricant with both R407C and R410A, and PAGs and esters with R134a. Most of the friction and wear data obtained were for 356-T61 and 390-T6 aluminum alloys. The effects of the viscosity of the L/R mixture and the initial surface roughness of the aluminum specimens were also evaluated. Finally, the effect of the environmental pressure of R134a refrigerant on the surface fatigue of 356-T61 alloys was analyzed. The results can be summarized as follows:

- The 2024-T351 and 6061-T61 alloys have approximately two orders of magnitude higher wear than the other materials tested. The friction coefficient of these alloys is also significantly higher and the contact resistance is lower than that of other alloys.
- In general, the amount of wear decreases as the amount of silicon content increases. This trend, however, is complicated by the presence of other alloying elements and the different heat treatment processes.
- The addition of bismuth and higher amount of copper reduces wear for alloys of otherwise similar composition and heat treatment.
- The lowest wear is obtained with the 39ODC-T6 alloy. The HV4-T61 alloy also gives very good wear resistance.
- Conventional anodizing (356CM-AM) does not improve the wear resistance of the 356-aluminum alloy under concentrated contacts. The hard layer cracks under the high contact stress causing an increase in wear.
- The Ester/R134a mixtures consistently provided better protection of the aluminum disc specimens compared to the PAG/R I 34a mixtures, even though the viscosity of the Ester/ R 1 34a mixture is lower than that of the PAG/R134a mixture.
- Hard anodizing and SiC particle reinforcement provide good wear resistance. However, they cause increased wear on the counter-face due to the rough hard surfaces generated by hard anodizing processes and the hard SiC particles on the surface of a SiC-Al composite.

The capped PAG (PAG 2) seems to be a better lubricant for 356CM-T61 alloy than the uncapped lubricant (PAG 1). However, for the 390PM-T61 alloy, the lubricity of the PAG's is about the same. When Ester 1 lubricant is used, the wear on the discs of both alloys is about the same in R134a, R407C, R410A and air environments. The R407C and R410A used with alkyl-benzene lubricant provide similar (with 39OPM-T61) or slightly better (with 356CM-T6 1) wear resistance when compared to R22. The lower wear obtained with the 356CM-T61 alloy is probably due to the higher viscosity of alkylbenzene/R407C or R410A mixtures compared to the alkylbenzene/R22 mixture. However, the relative wear differences between these mixtures are small, therefore, more tests need to be conducted to examine their lubricity difference, if any exists. The mineral/ R22 mixture produces less wear (with 356CM-T61) than the other mixtures, even though the viscosity of the mineral/R22 mixture is smaller than that of

the other mixtures. However, with the 390PM-T61, it is the mineral/R407C mixture, which provides, slightly better wear resistance compared to the other mixtures. The R I 34a refrigerant does not always behave as an inert environment. Under the conditions of this study, a chemical reaction between the freshly exposed aluminum and R134a occurred. The reaction product was identified as AlF3. However a -solid conclusion cannot be made about this reaction without further experimentation.

APPENDIX 2

A-2 Investigation of Profilometer Stylus Damage on Sample Surface

A-2.1 Introduction

After running initial tests on the aluminum sample using the Dektak profilometer to obtain surface roughness, it was decided that more specific objectives should be set before running further test. This Appendix primarily deals with the effect of stylus load on sample surface. The objective of this study was to investigate the surface damage caused by the stylus on the sample surface (NB: Unlike the discs in the thesis, these disks were machined circumferentially, therefore making the radial data the most important data).

A-2.1.1 Experimentation

The procedure was as follows:

1. Chose an appropriate sample as a specimen, making sure it has the least amount of scratches (other then machining scratches).
2. Clean the surface, first by dipping it acetone, and then placing the sample in the ultrasonic cleaner, for 15 minutes.
3. The sample is then placed in a container (to prevent contamination). This ends the cleaning process.
4. The area on the sample where the tests are to be run is then selected and marked.
5. The sample is then viewed under a microscope which has a camera attached to it and pictures of the virgin area are taken.
6. The sample is cleaned again.
7. A set of specific profilometer tests are ran on individual sections, the results of the tests are analyzed.
8. The surface is viewed under the microscope again to observe any scratches caused by the contact profilometer.
9. The surface parameters are analyzed using MatLab.

A-2.1.2 Experimental data

This report presents the experimental data (MatLab analysis) and a conclusion of each experimental set. The report is composed of four different experimental sets, described below.

1. AREA 7 & 8; radial direction scans, constant length, constant number of data points, varied position and varied stylus force.
2. AREA 9; radial direction scans, constant length, constant number of data points, varied position and constant stylus force.
3. AREA 1B; radial direction scans, constant length, constant number of data points, constant position and constant stylus force.

A detailed analysis of the mentioned experiments is discussed below.

AREA 7&8:

The area consisted of profilometer scans in the radial direction.. The tests were run for a scan length of 500µm, 4000 data points and varied stylus force (from a minimum of 1 mg to a maximum of 40 mg). The results of these tests are summarized in Table A-7&8. If we study the Ra values more closely a trend can be noticed. The Ra is initially about 0.23 microns (1 mg to 18 mg), as the stylus force is increased, the Ra increases to 0.29 (20 mg to 28 mg), with further increase in stylus force (30mg to 40mg) the Ra drops down to an average of 0.22 microns. This trend is also displayed by the Rq values. It should also be noticed that both the Dektak and MatLab results follow this trend. Could it be possible that the variation in load caused deformation and resulted in this trend? With further investigation, it was concluded that the trend was caused by uneven surface topography over the region (test positions 72 to 85 were much rougher than the surrounding regions). Due to the above discovery, no substantial conclusion on the effect of stylus force on statistical surface parameters could be established.

AREA 9:

After working on the above section it was decided that some tests should be run to see the variation of the statistical parameters with changes in position on the surface of the sample. Therefore this section was run with a constant stylus force of 40mg, scan length of 3000 microns, and 4800 data points were collected in the radial direction. The results are tabulated in table A-9. As can be observed from Table A-9, the Ra values varied from scan to scan by a maximum margin of 0.02 microns, this is due to the waviness of the surface and filtering of data. The results obtained in this section were fairly satisfying. Since the maximum stylus force was used, the sample was viewed under a high power microscope to check for any surface damage. No visible damage was observed. In the pursuit of identifying surface damage due to stylus force, another experiment was designed, this on in area 1b.

AREA 1-B:

This set of experiments was to be run with constant position, constant stylus force of 40mg, constant scan length of 3000 microns and constant number of data points collected (4800 points). In other words, it was one scan repeated six times. The results from this were very encouraging, with little variation in Ra and Rq values over the range of the experiments. However, no surface damage could be observed with the high power microscope. If any surface damage was caused, the asperities would be smoothened, thus their Ra and Rq values would have decreased as the number of tests ran on the same section increased. However this trend was also missing from the obtained data. It was now decided to have a theoretical approach into investigating the surface damage by the stylus.

A-2.2 Theoretical Calculations of Stylus Damage

The plasticity index is calculated to investigate whether the surface experiences plastic, elastic or both deformations. Below are the equations used to calculate the plasticity index.

$$\Psi = E^*/H[(\sigma/Rs)^{0.5}] \qquad \text{(Equation A-3.1)}$$

$$E^* = [(1-\nu_1^{\,2})/E_1 + (1-\nu_2^{\,2})/E_2]^{-1} \qquad \text{(Equation A-3.2)}$$

$$\Delta = a^2/Rs = [(9\,W^{\wedge 2})/(16Rs*E^{*\wedge 2})]^{(1/3)} \qquad \text{(Equation A-3.3)}$$

Ψ = Plasticity Index

E*= Youngs Modulus

H= Hardness

ν= Poissons Ratio

W= Load

Rs= Radius of Contact

Example:

Aluminum Sample, (1)

Steel Pin Tip (2)

Rs = 2.5μm

σ = 0.26μm

ν_1 = 0.33

ν_2 = 0.29

H = 6 x $10^{\wedge 9}$ Pa

E^*_1 = 6.89 x 10^{10}

E^*_2 = 2.068 x 10^{11}

W = 40mg

Using above equations, the following results were obtained

Ψ = 3.1, therefore plastic deformation.

Δ = 1.394μm

A-2.3 Conclusion:

According to the calculations, plastic deformation should take place of a magnitude of 1.4 microns, however this is smaller then the diameter of the stylus tip, therefore difficult to notice in experiment Area 1-B. It can also be concluded that, due to the low approach (depth) caused by the plastic deformation, it is relatively difficult to spot the change using a contact profilometer.

Table A-1B, (8000 data points, Radial Direction)

TABLE A-1B						**Asperity**			
NUMBER	**LENGTH**	**FORCE**	**Ra**	**Rq**	**Radius**	**Density**	**Roughness Parameter**	**SKEWNESS**	**KURTOSIS**
	um	**mg**	**Um**	**um**	**um**	**um^2**	**beta**		
AREA 1									
A11B	2000	40	0.6171	0.73799	20.873	0.01062	0.16359	0.19973	2.6177
A12B	2000	40	0.37664	0.47214	20.384	0.010971	0.10559	0.22783	2.2698
A13B	2000	40	0.34029	0.42315	21.153	0.01059	0.094789	0.12478	2.847
A14B	2000	40	0.33046	0.41473	20.437	0.011059	0.09373	0.17762	2.6424
A15B	5000	40	2.2453	2.6113	33.052	0.0057799	0.49887	0.011942	1.7605
Total			**1.63328**	**62.41**	**82.847**	**0.04324**	**0.457699**		
Mean			**0.326656**	**12.482**	**16.5694**	**0.008648**	**0.0915398**		

Table 9 (4800 data points Radial Direction)

Number	**FORCE**	**LENGTH**	**Ra**	**Rq**	**Radius**	**Density**	**Roughness Parameter**	**SKEWNESS**	**KURTOSIS**
	(mg)	**um**	**um**	**um**	**um**	**um^2**	**beta**		
91	40	3000	0.34604	0.43461	35.537	0.0054725	0.084521	-0.15012	2.7936
92	40	3000	0.3605	0.45164	35.429	0.0054718	0.087554	-0.17585	2.8544
93	40	3000	0.36626	0.45804	35.409	0.0054597	0.088549	-0.14097	2.7988
94	40	3000	0.35338	0.44281	35.31	0.0054641	0.085436	-0.14153	2.7653
95	40	3000	0.35251	0.44193	35.298	0.0054599	0.08517	-0.1479	2.7988
96	40	3000	0.3532	0.44253	35.366	0.0054303	0.084988	-0.14702	2.804
TOTAL			1.77869	2.22903	176.983	0.027328	0.43123		
MEAN			0.29644833	0.371505	29.49716667	0.004554667	0.071871667		

Table A-7&8 (4000 data points, Radial direction)

Number	**LENGTH**	**FORCE**	**Ra**	**Rq**	**Radius**	**Density**	**Roughness Parameter**	**SKEWNESS**	**KURTOSIS**
	Um	**mg**	**um**	**um**	**um**	**um^2**	**beta**		
71	500	1	0.24512	0.30612	6.9029	0.052447	0.11083	-0.054563	2.746
72	500	5	0.21209	0.26495	7.0719	0.049278	0.092331	-0.32716	2.7951
73	500	10	0.2342	0.28671	7.001	0.04915	0.098658	-0.18844	3.9455
76	500	15	0.23843	0.3175	7.543	0.041174	0.098607	-0.018636	2.5142
77	500	18	0.23008	0.28314	7.8366	0.045096	0.10006	-0.49792	2.9913
78	500	20	0.34505	0.43603	7.5033	0.044717	0.1463	0.20048	2.5962
81	500	25	0.29528	0.36584	7.4779	0.044621	0.12207	-0.083047	2.3118
82	500	28	0.33506	0.40054	7.924	0.043763	0.1389	-0.3465	2.7346
85	500	30	0.23674	0.29311	7.5	0.045989	0.1011	-0.29229	3.4208
86	500	32	0.24252	0.30862	7.1951	0.043353	0.096269	0.50157	2.5312
87	500	35	0.23453	0.29025	8.0459	0.04015	0.093765	0.76526	2.6926
88	500	38	0.46045	0.56271	7.9434	0.04488	0.20061	0.096939	2.477
89	500	40	0.21999	0.27296	7.6303	0.043603	0.090816	-0.028976	2.7627
TOTAL			1.490316	-0.273283	97.5753	0.588221	1.490316		
MEAN			0.11464	-0.02102	7.505792	0.04525	0.11464		

APPENDIX 3

A-3 Surface Characterization Methods

A-3.1.1 SEM Introduction

The SEM is a surface analysis technique, which uses a focused beam of electrons rastered across a sample surface, the raster scan being synchronous with that of a cathode ray tube (CRT). The brightness of the CRT is modulated by the detected secondary electron current from the sample, such that the viewing CRT displays an image of the variation of secondary electron intensity with position on the sample. This variation is largely dependent on the angle of incidence of the focused beam onto the sample, thus yielding a topographical image. Different detectors can be used to provide alternative information, e.g., a backscattered electron detector will provide average atomic number information. An auxiliary energy dispersive X-ray (EDS) detector provides elemental identification analyses from boron to uranium. Some high performance instruments have enhanced abilities due to use of a special field-emission electron source (FE-SEM).

A-3.1.2 Specimen Requirements

- Insulating samples must be coated with a conductive film
- Vacuum compatible
- <125 mm diameter, <50 mm height

A-3.1.3 Unique Advantages

- High resolution with little sample preparation
- Large depth of field allows use with rough samples
- Rapid qualitative analysis of particles and small areas by (EDS)

A-3.2 Energy Dispersive X-ray Spectrometry (EDS)

A-3.2.1 Description

An EDS attachment to an SEM permits the detection and identification of the x-rays produced by the impact of the electron beam on the sample thereby allowing qualitative and quantitative elemental analysis. The electron beam of an SEM is used to excite the atoms in the surface of a solid. These excited atoms produce characteristic X-rays, which are readily detected. By utilizing the scanning feature of the SEM, a spatial distribution of elements can be obtained. For flat, polished homogeneous samples, quantitative analysis can provide relative accuracy of 1-3% when appropriate standards are available.

A-3.2.2 Specimen Requirements

- Insulating samples must be coated with a thin conductive film
- <125 mm diameter, <40 mm height
- Quantitative analysis requires standard materials of known concentration be available for comparison for best results
- Quantitative analysis requires flat, polished homogeneous samples

A-3.2.3 Unique Advantages

- Rapid identification of particles, films, and unknown bulk materials
- Very fast elemental images and line scans
- Excellent first look technique for new problems

Following dektak analysis and surface SEM imaging, we progressed into looking at cross-sections of the worn samples. A standard procedure had to be established in order to achieve a surface, which can be analyzed under the SEM. While getting a cross section, it is important not to damage the surface. The procedure to be followed is as follows:

1. Clean up the surface of the sample.
2. Use the low speed diamond saw to cut the samples into the required shapes. This instrument ensures that the minimum damage occurs on the sides of the sample due to the cutting process. Water is used as both a lubricant and a coolant for the cutting process. A diamond blade is used so as to cut the sample precisely.
3. After obtaining the desired shapes the samples are washed in water (to remove any residue from the cutting process).
4. The sample is not to be polished to remove the layers of damaged material.
5. First start with a 200 level sand water sand paper, and polish the surface until all the cutting marks have disappeared and a smooth surface is visible.
6. Now use 400-level sandpaper and polish the sample to get a smother finish.
7. Finally, use the 600 sandpaper to reach the undamaged surface.
8. Take the samples and clean them ultrasonically (using acetone and ethanol to rinse them).
9. Now you can view the samples under the SEM. Use the EDS to identify the elements formed on the surface of the sample.

A-3.2.4 Analysis

From the EDS results it was observed that Al, Si, C, F, Mg, Mn, Fe and oxides were present on the surface of the samples. It was suspected that the Mn, Mg, Fe, are obtained from deposits of the worn out steel shoes. The F and C are formed directly from the refrigerant or as a result of a chemical reaction involving the refrigerant. The results obtained form this set of experiments were not reliable, the main reason for this being that the sample was not

prepared as it was supposed to, (Due to this reason the results have not been illustrated in this section). We therefore deduced erroneous conclusions especially with regard to the oxide layer. It was assumed that the oxide layer was several microns thick, but in reality the damage as seen in the image is due to poor sample preparation and is not an oxide layer. After some literature search and consultation with experts, it was concluded that the experiments were indeed erroneous. In my investigation, I obtained a copy of the Leco catalogue titled *metallography and principles and procedures*. This book describes the correct procedure to carry out sample preparation for SEM experimentation. From the study carried out in this section, the conclusion deduced was to get reliable results from SEM correct sample preparation is vital.

A-3.3 Fourier Transform Infrared Spectrometry (FTIR)

A-3.3.1 Description

Fourier transform infrared (FTIR) spectroscopy is a powerful analytical tool for characterizing and identifying organic molecules. The IR spectrum of an organic compound serves as its fingerprint and provides specific information about chemical bonding and molecular structure.

Micro beam FTIR allows areas as small as 10-15 microns to be analyzed; this allows the source of organic particles to be determined. Using attenuated total reflectance (ATR), thin films can be analyzed directly on a surface. FTIR aids in precise determination of the chemical identity of organic contamination in a variety of samples 'including samples from the disk drive, biomedical, semiconductor, PCB, electronic, laser and optic industries.

A-3.3.2 Advantages:

- Small spot size (10-15 microns)
- Detailed chemical bonding information
- Organic analysis of polymers and plastics
- Analysis of liquids, solids, and gases
- In ATR mode can sample the outer - 1000 A
- Non-destructive analysis
- Can analyze non-conductive materials
- Molecular specific identification

A-3.3.3 Applications of FTIR:

- Spots and discolorations on magnetic disks and other metal surfaces
- Films of contamination
- Contamination extracted from surfaces
- Molecular composition of plastics and polymers
- Fibers - composite and polymeric
- Particles
- Composite materials
- Contaminants on PCB's, electronic components

A-3.4 Transmission Electron Microscopy (TEM)

A-3.4.1 Description.

In transmission electron microscopy (TEM), a beam of highly focused electrons is directed toward a thinned sample (<200 nm). These highly energetic incident electrons interact with the atoms in the sample producing characteristic radiation and particles providing information for materials characterization. Information is obtained from both deflected and non-deflected transmitted electrons, backscattered and secondary electrons, and emitted photons.

A-3.4.2 Applications:

Because the electron beam goes through the sample, transmission electron microscopy reveals the interior of the specimen. It gives structure: the size, shape, and the distribution of the phases that make up the material. It gives composition: the distribution of the elements, including segregation if present. It shows the crystallography: the crystal structure of the phases and the character of the crystal defects.

A-3.5 Raman Spectroscopy

Raman spectroscopy is a universal analytical technique for identification of molecules gases, liquids and solids by scattering of laser light. The Raman spectrum is a vibrational signature of a molecule or complex system. Its origin lays in the inelastic collisions between the molecules composing say the liquid and photons, which are the particles of light composing a light beam. The collision between the molecules and the photons leads to an exchange of energy with consequent change in energy and hence wavelength of the photon. Recent developments in the dispersive Renishaw Raman spectrometer include the user of low power NIR diode lasers with high stability and optical efficiency, reduction of fluorescence, wide scan range and high spectral resolution and interactive software designed for use in analytical laboratories. Analysis of dense and/or dark samples and aqueous phase samples and very small sampling volumes of especially precious biological samples can be carried out with relative ease.

A-3.6 Conclusion

Several methods exist for chemical analysis of layers that exist on and below the surface of a sample. However, as described from the SEM section, there are two important things to choose before analysis; correct chemical analysis method and correct sample preparation method. Some of the methods described earlier may not be feasible for our sample due to grossness of the sample.